FIRST-PRINCIPLES STUDY OF ELECTRONIC PROPERTIES OF ONE DIMENSIONAL NANOSTRUCTURES

By

JUNWEN LI

Bachelor of Science in Applied Physics
Qingdao University
Qingdao, Shandong, China
1999

Master of Science in Physics
Institute of Physics, Chinese Academy of Sciences
Beijing, China
2002

Submitted to the Faculty of the
Graduate College of
Oklahoma State University
in partial fulfillment of
the requirements for
the Degree of
DOCTOR OF PHILOSOPHY
May, 2010

FIRST-PRINCIPLES STUDY OF ELECTRONIC PROPERTIES OF ONE DIMENSIONAL NANOSTRUCTURES

Dissertation Approved:

Dr. John W. Mintmire

Dissertation Advisor

Dr. Timothy M. Wilson

Dr. Yin Guo

Dr. Nicholas F. Materer

Dr. A. Gordon Emslie

Dean of the Graduate College

ACKNOWLEDGMENTS

I am pleased to acknowledge my appreciation for those who have helped this dissertation take shape.

First and foremost, my sincere thanks go to my advisor, Dr. John Mintmire, for spending enormous time and efforts in guiding my research. Every week I obtain valuable feedback from our discussion at individual and group meetings. I will always remember the scenes when he derived formulas and elucidated my puzzles on paper or the board. This dissertation originates from these gradual accumulations. He provides strong support for my research projects with his insight and understanding of the research field and grand knowledge. His rigorous scholarship is what I myself hope to achieve in my future research career. Dr. Mintmire also sets up an example for me to follow as an individual.

I would like to thank my committee members: Dr. Timothy Wilson, Dr. Yin Guo, and Dr. Nicholas Materer for their time and patience in serving my committee and reviewing my research proposal and dissertation. I appreciate their valuable comments and advice on my work.

I would like to thank Dr. Jacques Perk, Dr. Xincheng Xie, and Dr. Robert Hauenstein for their help and encouragement. I would also like to thank Dr. Carter White and Dr. Daniel Gunlycke at Naval Research Laboratory and Dr. Vincent Munier at Oak Ridge National Laboratory for our collaboration.

My thanks must go to all the former and current members in the research group and fellow graduate students for their friendship and indispensable support, but I have to single out Dr. Shelly Elizondo, Dr. Thushari Jayasekera, Vasantha Jogireddy,

and Pillalamarri Pavan for their help, friendship, and making a pleasant work environment.

Finally, I would like to thank my parents, my grandfather, my elder brother and his family for always being there for me, even though whole continents and oceans stand between us. Thanks to my wife, Jing Zhu, for her love, patience, and encouragement. She has always been an invaluable source of strength and support for me during the years we have been together.

TABLE OF CONTENTS

Chapter Page

1 INTRODUCTION 1

1.1 Overview 1

1.2 Organization of the Dissertation 4

2 THEORETICAL BACKGROUND AND APPROACHES 5

2.1 Overview 5

2.2 Hartree-Fock Approximation 7

2.3 DFT Methods 12

2.3.1 Overview 12

2.3.2 Thomas-Fermi Model 12

2.3.3 Hohenberg-Kohn Theorems 15

2.3.4 Kohn-Sham Formulation 17

2.4 Exchange Correlation Approximations 21

2.4.1 Overview 21

2.4.2 Local Density Approximation 21

2.4.3 PBE Generalized Gradient Approximation 23

2.5 Gaussian Basis Sets 26

2.6 Helical Band Structure Methods 28

2.7 Landauer Approach for Quantum Conductance Calculation 29

3 GRAPHENE NANORIBBONS 34

3.1 Introduction 34

3.2 Planar Zigzag Graphene Nanoribbons 36
3.2.1 Overview 36
3.2.2 Energetic Results 38
3.2.3 Non-spin-polarized LDF Band Structures 40
3.2.4 Ferromagnetic LDF Band Structures 45
3.2.5 Antiferromagnetic LDF Band Structures 49
3.2.6 Summary 54
3.3 Planar Armchair Graphene Nanoribbons 55
3.3.1 Overview 55
3.3.2 Model Structure 56
3.3.3 Local Density Functional Results 58
3.3.4 Consideration of Longer Range Interactions 61
3.3.5 Summary 65
3.4 Twist Effect in Electronic Properties of Armchair Graphene Nanoribbons 66
3.4.1 Overview 66
3.4.2 Computational Approach 68
3.4.3 Band Structures and Near-gap Wavefunctions 70
3.4.4 Structure Parameters 73
3.4.5 Tight-binding Model 75
3.4.6 Band Gap Change Under Twist 77
3.5 Summary and Conclusions 81

4 SURFACE PASSIVATION EFFECTS IN SILICON NANOWIRES 82

4.1 Overview 82
4.2 Computational Approaches 85
4.3 Structure Parameters 89
4.4 Mulliken Population Analysis 91
4.5 Band Gap Change 93

4.6 Electronic Structures 96
4.7 Near-gap States 99
4.8 Effective Mass of Charge Carriers 107
4.9 Surface Defects Effect on Transport 109
4.9.1 Computational Approach 109
4.9.2 Transport Conductance 111
4.10 Summary and Conclusions 113

5 CONCLUSIONS **114**

LIST OF TABLES

Table Page

3.1 Total energies divided by $2N$ and energy differences between different spin configurations of zigzag GNRs with various ribbon widths 39

3.2 Energy gaps of zigzag GNRs with various ribbon widths 53

3.3 Band gaps E_{gap} of armchair GNRs with ribbon width N 60

3.4 Binding states of edge C p_z orbitals HOMO and LUMO. $\uparrow$ ($\downarrow$) indicates the energy point shifts upward (downward) with increasing twist angle. $+$ ($-$) indicates the bonding (anti-bonding) states. 76

3.5 Band gaps (eV) as a function of twist angle (Deg) in armchair graphene nanoribbons with various widths N 80

4.1 Band gaps (eV) as a function of diameter for $\langle 100 \rangle$ silicon nanowires with various passivations. X represents H, OH, or CH_3. 95

4.2 Band gaps (eV) as a function of diameter for $\langle 110 \rangle$ silicon nanowires with various passivations. X represents H, OH, or CH_3. 95

4.3 Effective mass of silicon nanowires along $\langle 100 \rangle$ and $\langle 110 \rangle$ directions with various passivations 108

LIST OF FIGURES

Figure Page

3.1 Sample zigzag GNRs with ribbon width $N = 6$. The numbering of the unit cells is shown at the left side of the ribbon with only the unit cell labeled 0 shown in their entirety. Each unit cell is composed of $2N$ C atoms and 2 H atoms. The $2N$ C atoms in unit cell 0 are numbered as shown. The index of zigzag chains is indicated at bottom from left to right. 37

3.2 (a) Total energy differences divided by $2N$ between non-spin-polarized and ferromagnetic states in zigzag GNRs as a function of ribbon width N. (b) Total energy differences divided by $2N$ between ferromagnetic and antiferromagnetic states in zigzag GNRs as a function of ribbon width N. 39

3.3 Calculated non-spin-polarized band structure and density of states of zigzag GNRs of width $N = 6$. Γ (X) corresponds to the center (edge) of the first Brillouin zone. 41

3.4 Calculated non-spin-polarized band structure and density of states of zigzag GNRs of width $N = 8$. Γ (X) corresponds to the center (edge) of the first Brillouin zone. 42

3.5 Calculated non-spin-polarized band structure and density of states of zigzag GNRs of width $N = 10$. Γ (X) corresponds to the center (edge) of the first Brillouin zone. 43

3.6 Calculated HOMO band orbital densities of zigzag GNRs of width N = 6, calculated at wavevectors (a) π, (b) 0.875π, (c) 0.75π, and (d) 0.625π, respectively. Calculated orbital densities for the LUMO band are given for wavevectors (e) π, (f) 0.875π, (g) 0.75π, and (h) 0.625π, respectively. The isovalue is taken to be 0.008 for all plots. 44

3.7 Calculated ferromagnetic band structure and density of states of zigzag GNRs of width $N = 6$. Γ (X) corresponds to the center (edge) of the first Brillouin zone. 46

3.8 Calculated ferromagnetic band structure and density of states of zigzag GNRs of width $N = 8$. Γ (X) corresponds to the center (edge) of the first Brillouin zone. 47

3.9 Calculated ferromagnetic band structure and density of states of zigzag GNRs of width $N = 10$. Γ (X) corresponds to the center (edge) of the first Brillouin zone. 48

3.10 Calculated antiferromagnetic band structure and density of states of zigzag GNRs of width $N = 6$. Γ (X) corresponds to the center (edge) of the first Brillouin zone. 50

3.11 Calculated antiferromagnetic band structure and density of states of zigzag GNRs of width $N = 8$. Γ (X) corresponds to the center (edge) of the first Brillouin zone. 51

3.12 Calculated antiferromagnetic band structure and density of states of zigzag GNRs of width $N = 10$. Γ (X) corresponds to the center (edge) of the first Brillouin zone. 52

3.13 Magnitude of the HOMO-LUMO antiferromagnetic gap of the zigzag GNRs as a function of ribbon width N. 53

3.14 (a) Symmetric armchair GNRs with ribbon width $N = 7$. Each unit cell is composed of $2N$ C atoms and 4 H atoms. (b) Staggered armchair GNRs with ribbon width $N = 8$. Each unit cell is composed of N C atoms and 2 H atoms. For (a) and (b) the numbering of the unit cells is shown at the left edge of each figure with only the unit cells labeled 0 shown in their entirety. The C atoms in unit cell 0 are numbered as shown. The index of dimer lines is indicated at bottom from left to right. 57

3.15 Calculated band structures of armchair GNRs of various widths. (a), (b), and (c) correspond to ribbon with $N = 7$, 8, and 9, respectively. Γ (X) indicates the center (edge) of the first Brillouin zone. 59

3.16 LDF energy gaps of the armchair GNRs as a function of width N. . . 60

3.17 Magnitude of the HOMO-LUMO gap of the N armchair GNRs from the TBM calculations. 63

3.18 LDF results for E_{gap} compared to the corresponding tight-binding model (TBM) results obtained from Eq. (3.3) with $V_1 = -3.2$ eV and $V_3 = -0.3$ eV. 64

3.19 (a) Armchair GNR with width $N = 8$. Each helical unit cell is composed of one zigzag chain terminated by H atoms. The N C atoms in a helical cell are numbered as shown. The bonds are labeled as a1-a11. (b) Axial view of 10 °-twisted armchair GNR with width $N = 8$. . . . 69

3.20 Electronic band structure of armchair GNRs (width $N = 8$) twisted by (a) 0 °, (b) 8.5 °, (c) 9.0 °, and (d) 10.0 °. 71

3.21 The LUMO and HOMO wave function of armchair GNRs (width $N = 8$) twisted by (a) 0 °, (b) 8.5 °, (c) 9.0 °, and (d) 10.0 °. The ribbons are vertically oriented. 72

3.22 C-C bond lengths of the twisted armchair GNRs with width $N = 8$ as a function of twist angle θ. 74

3.23 Variation of energy gaps of armchair GNRs as a function of twist angle θ. (a), (b), and (c) represent the armchair GNRs of width $N = 3m$, $3m + 1$, and $3m + 2$, respectively. 79

4.1 Cross-section views of the studied H-SiNWs. $\langle 100 \rangle$ SiNWs of diameter (a) 0.43 nm, (b) 0.87 nm, (c) 1.3 nm, and (d) 1.73 nm, respectively. $\langle 110 \rangle$ SiNWs of diameter (e) 0.73 nm, (f) 1.09 nm, and (g) 1.46 nm, respectively. The golden-yellow and silver balls represent Si and H atoms, respectively. In OH-SiNWs and CH_3-SiNWs, all H atoms are replaced with OH and CH_3 groups, respectively. 87

4.2 Band gaps as a function of diameter with hydrogen passivation for silicon nanowires along $\langle 100 \rangle$. The square and blue line indicate the LDF results and the uptriangle and red line indicate the PBE results. 88

4.3 Si-Si bond length as a function of the distance from bond center to wire axis. (a), (b), (c) correspond to $\langle 100 \rangle$ SiNWs of diameter $d =$ 1.73 nm passivated by H, OH, and CH_3, respectively. (d), (e), and (f) correspond to $\langle 110 \rangle$ SiNWs of diameter $d = 1.46$ nm passivated by H, OH, and CH_3, respectively. 90

4.4 Net charge as a function of distance from the atom to the wire axis. (a), (b), (c) correspond to $\langle 100 \rangle$ SiNWs of diameter $d = 1.73$ nm passivated by H, OH, and CH_3, respectively. (d), (e), and (f) correspond to $\langle 110 \rangle$ SiNWs of diameter $d = 1.46$ nm passivated by H, OH, and CH_3, respectively. Si, H, O, and C are indicated by $+$, $\times$, $\triangleright$, and $\triangleleft$, respectively. 92

4.5 Band gaps as a function of diameter with various surface passivations for silicon nanowires along (a) $\langle 100 \rangle$, (b) $\langle 110 \rangle$. 94

4.6 Electronic band structures of ⟨100⟩ SiNWs (diameter d = 1.73 nm) passivated by (a) H, (b) OH, and (c) CH_3. The Fermi level in H-SiNW is shifted to zero eV and taken as the reference. 97

4.7 Electronic band structures of ⟨110⟩ SiNWs (diameter d = 1.46 nm) passivated by (a) H, (b) OH, and (c) CH_3. The Fermi level in H-SiNW is shifted to zero eV and taken as the reference. 98

4.8 The HOMO and LUMO orbital density of the ⟨100⟩ SiNWs. (a), (b), and (c) correspond to SiNWs passivated by H, OH, and CH_3, respectively. Here red and blue represent HOMO and LUMO density, respectively. The contour is at 10% of the maximum value. 100

4.9 The HOMO and LUMO orbital density of the ⟨110⟩ SiNWs. (a), (b), and (c) correspond to SiNWs passivated by H, OH, and CH_3, respectively. Here red and blue represent HOMO and LUMO density, respectively. The contour is at 10% of the maximum value. 101

4.10 The HOMO orbital isosurface of the ⟨110⟩ H-SiNWs (diameter d = 1.46 nm). Here red and blue represent positive and negative values, respectively. The contour is at 10% of the maximum value. 103

4.11 The LUMO orbital isosurface of the ⟨110⟩ H-SiNWs (diameter d = 1.46 nm). Here red and blue represent positive and negative values, respectively. The contour is at 10% of the maximum value. 104

4.12 The HOMO orbital isosurface of the ⟨110⟩ CH_3-SiNWs (diameter d = 1.46 nm). Here red and blue represent positive and negative values, respectively. The contour is at 10% of the maximum value. 105

4.13 The LUMO orbital isosurface of the ⟨110⟩ CH_3-SiNWs (diameter d = 1.46 nm). Here red and blue represent positive and negative values, respectively. The contour is at 10% of the maximum value. 106

4.14 Model system for the conductance calculation. The system is composed of three regions: left-hand lead region, central conductor region, and right-hand lead region. 110
4.15 The transport conductance through the OH-passivated region: The solid line is the conductance of the pure H-SiNWs. The dashed line shows the conductance of the H-SiNWs with OH defects on one helical cell. 112

CHAPTER 1

INTRODUCTION

1.1 Overview

Nanotechnology deals with structures between 1 nanometer and 100 nanometer in size. The materials at this scale can display properties very different from their bulk counterparts. These unique nanoscale properties originate from size effects such as the enhanced surface-to-volume ratio that causes surface atoms to experience potentials different from those in the bulk. In recent years the rapid development of fabricating and manipulating materials at nanometer scale has opened up a great deal of opportunities in a variety of scientific research efforts and practical applications.

We can consider different numbers of spatial dimensions at nanometer scale. Depending on how many dimensions are confined, the nanomaterials are termed as quantum well, quantum wire, and quantum dot for constraints on one, two, and three dimensions, respectively. Of these different systems, the quantum wire of one-dimensional extension represents the simplest transport path and is of especially great significance in electronic applications. Two types of one-dimensional nanostructures were investigated in this dissertation: graphene nanoribbons and silicon nanowires.

Our study on graphene nanoribbons was motivated by the discovery of new experimental methods for graphene, a single sheet of graphite. Novoselov, *et al.*,[1, 2] using a micro-mechanical cleavage method to extract a single sheet from three-dimensional graphite, obtained the two-dimensional form of carbon, i.e., graphene, which is stable under ambient conditions. The quality of the samples prepared were good enough so that the ballistic transport[1] and quantum Hall effect[3] were observed easily. The

ballistic transport makes this new material a promising candidate for future electronic applications such as ballistic field-effect transistors (FETs). Although experimental work on graphene systems is recent, the theoretical study of graphene started long ago, with Wallace's tight-binding study in 1947 as an early work. [4] After that many properties of graphite and nanotubes were derived using graphene as starting point. The experimental achievement of graphene in 2004 attracted great attention immediately. Two-dimensional graphene has a zero band gap with linear energy dispersion near the Fermi level and crossing at the Dirac point between valence and conduction bands. For practical electronic application in semiconductor industry a band gap could be induced by fabricating graphene nanoribbons. The ribbon structures have already been successfully obtained with various techniques such as lithographic patterning,[5] chemical vapor deposition,[6] Joule heating,[7] and unzipping the carbon nanotubes (CNTs).[8, 9]

The other one-dimensional structures investigated, silicon nanowires, have a wide variety of applications from use in batteries to use in energy conversion. Because of the geometry of silicon nanowire arrays, they are capable of inflating 4 times their normal size when absorbing lithium ions, which enables the new kind of battery to hold 10 times the charge of existing lithium-ion batteries.[10] The one-dimensional structure of silicon nanowires can allow p-i-n coaxial solar cells consisting of a p-type silicon nanowire core surrounded by i- and n-type silicon shells.[11] An advantage of this core/shell architecture is that carrier separation takes place in the radial rather than the axial direction, with a carrier collection distance smaller or comparable to the minority carrier diffusion length. Si nanowire arrays show promise as high-performance, scalable thermoelectric materials because of the high electron conductivity and low phonon conductivity in silicon nanowires with rough surface.[12, 13]

The promising applications of these nanostructures require a better theoretical understanding of their electronic properties. Our computational simulations of elec-

tronic properties of graphene nanoribbons and silicon nanowires are of great significance from both fundamental and practical points of view.

1.2 Organization of the Dissertation

Chapter 2 presents a brief introduction of the theoretical background and computational approaches utilized throughout this work. We briefly review the theoretical formalism of density functional theory, helical band structure methods, and the transport conductance approach with Landauer formula implemented by using non-equilibrium Green's function method.

Chapter 3 is dedicated to the simulation results from a study carried out on graphene nanoribbons. This theoretical study was primarily motivated by the experimental implementation of isolated graphene sheets which are a single layers of carbon atoms connected with hexagonal patterns. In this work, we investigated two kinds of graphene nanoribbons, namely zigzag and armchair graphene nanoribbons according to the edge shape. For zigzag nanoribbons, the calculations on energetic analysis and corresponding band structures were carried out. For armchair nanoribbons, we studied the electronic structure dependence on the ribbon width and on the torsional deformation. We have four papers related to the ribbon studies. [14–17]

Chapter 4 is devoted to the investigation carried out involving surface passivation effect in silicon nanowires. Because of the enhanced surface-to-volume ratio in silicon nanowires compared to bulk silicon, the electronic properties of the nanowires are strongly dependent on the surface substituents. We studied three kinds of passivating functional groups such as hydrogen, hydroxyl, and methyl. We also investigated the hydroxyl surface defects effect on transport property of pure hydrogen-passivated silicon nanowires. We have two papers based on the simulations presented in this chapter.[18, 19]

Chapter 5 summarizes this dissertation, focusing on the simulation findings and the possible further investigation based on the present calculations.

CHAPTER 2

THEORETICAL BACKGROUND AND APPROACHES

2.1 Overview

All band structure calculations reported in this work were carried out by using the Helical Nanostructures (HENS) `parallax` code developed by Dr. Mintmire at Oklahoma State University. Different from regular band structure codes that use translational symmetry, this approach takes advantage of the helical symmetry in one-dimensional nanostructures such as polymers, nanoribbons, nanotubes, and nanowires. Taking account of the helical symmetry can greatly reduce the unit cell size, and therefore can achieve major computational savings. Fujita and Imamura[20, 21] first proposed this idea of utilizing helical symmetry when studying the electronic structures of polymers with tight binding model. And this approach was developed for first-principles methods by Dr. Mintmire while at the Naval Research Laboratory. Mintmire, *et al.*,[22] using this helical band structure code, successfully predicted that the armchair single-walled carbon nanotubes would be metallic four years prior to the experimental verification. Now we apply this code in the study of graphene nanoribbons and silicon nanowires.

The zero-bias conductance was calculated within a Landauer approach.[23, 24] The transport code was developed by using the non-equilibrium Green's function (NEGF) formalism within a linear response regime. The approach is capable of taking any general Hamiltonian that can be described with a localized orbital basis, such as orthogonal, non-orthogonal tight-binding models, and first-principles results by making use of Gaussian orbitals as in the study of surface defects effect in silicon

nanowires. The effective Hamiltonian matrix elements and orbital overlap matrix elements used in the investigation of silicon nanowires were generated by the HENS `parallax` self-consistent field (SCF) calculations.

In this chapter, we will briefly describe the background on which the codes are based, including the density functional theory (DFT), the helical band structure method and the NEGF approach. Before that the Hartree-Fock method is reviewed in order to gain some idea on the exchange interaction and the advantage of DFT when dealing with many-electron system. The discussion in this chapter is mainly adapted from Refs. [25–27].

2.2 Hartree-Fock Approximation

For an isolated N-electron atomic or molecular system, in the Born-Oppenheimer approximation the time-independent non-relativistic Schrödinger equation is given by

$$\hat{H}\Psi = E\Psi, \tag{2.1}$$

where E is the electronic energy, $\Psi = \Psi(\mathbf{x}_1, \mathbf{x}_2, ..., \mathbf{x}_N)$ is the N-electron wavefunction, and $\hat{H}$ is the Hamiltonian operator composed of three terms,

$$\hat{H} = \hat{T} + \hat{V}_{ext} + \hat{V}_{ee}, \tag{2.2}$$

where

$$\hat{T} = \sum_{i=1}^{N} -\frac{1}{2}\nabla_i^2 \tag{2.3}$$

is the kinetic energy operator,

$$\hat{V}_{ext} = \sum_{i=1}^{N}\sum_{\alpha=1}^{M} -\frac{Z_i}{|\mathbf{r} - \mathbf{R}_\alpha|} \tag{2.4}$$

is the electron-nucleus attraction energy operator, and

$$\hat{V}_{ee} = \sum_{i\neq j}^{N} \frac{1}{|\mathbf{r}_i - \mathbf{r}_j|} \tag{2.5}$$

is the electron-electron repulsion energy operator. When additional fields are present, $\hat{T}$ and $\hat{V}_{ee}$ remain unchanged and extra terms appear in $\hat{V}_{ext}$.

The total energy E_{TOT} of the system is composed of the electronic energy E and the nucleus-nucleus repulsion energy

$$V_{nn} = \sum_{\alpha<\beta}^{M} \frac{Z_\alpha Z_\beta}{R_{\alpha\beta}}. \tag{2.6}$$

So we may have

$$E_{TOT} = E + V_{nn}. \tag{2.7}$$

The coordinate $\mathbf{x}_i$ of electron i comprises spatial coordinates $\mathbf{r}_i$ and spin freedom s_i. Atomic units are employed here and throughout this dissertation (unless otherwise specified): the length unit is the Bohr radius, $a_0 = 0.5292$ Å, the charge unit is the charge of the electron, e, and the mass unit is the mass of the electron, m_e.

The $\hat{T}$ and $\hat{V}_{ext}$ in Eq. (2.2) are single-particle operators and the $\hat{V}_{ee}$ is a two-particle operator from which the complications of many-body problem arises. We need to make approximation on the many-body wavefunction $\Psi(\mathbf{x}_1, \mathbf{x}_2, ..., \mathbf{x}_N)$. The simplest way to approximate the wavefunction is through the Hartree approximation, where the many-body wavefunction Ψ is replaced by a product of single-particle orbitals, $\psi_i(\mathbf{x}_i)$,

$$\Psi(\mathbf{x}_1, \mathbf{x}_2, ..., \mathbf{x}_N) = \frac{1}{\sqrt{N}} \psi_1(\mathbf{x}_1)\psi_2(\mathbf{x}_2) \cdots \psi_N(\mathbf{x}_N), \tag{2.8}$$

where $\psi_i(\mathbf{x_i})$ is a combination of spatial function $\phi_i(\mathbf{r}_i)$, and spin function $\sigma(s_i)$, such that

$$\psi_i(\mathbf{x}_i) = \phi_i(\mathbf{r}_i)\sigma(s_i), \tag{2.9}$$

where $\sigma = \alpha, \beta$ indicate spin-up and spin-down, respectively. However, the electrons are Fermions and should obey the Pauli exclusion principle which states that one quantum state only can be occupied by at most one electron. The wavefunction Ψ should be anti-symmetric with respect to the interchange of any two electron coordinates $\mathbf{x}_i$ and $\mathbf{x}_j$. Eq. (2.8), however, does not satisfy

$$\Psi(\mathbf{x}_1, ..., \mathbf{x}_i, ..., \mathbf{x}_j, ..., \mathbf{x}_N) = -\Psi(\mathbf{x}_1, ..., \mathbf{x}_j, ..., \mathbf{x}_i, ..., \mathbf{x}_N). \tag{2.10}$$

To account for Pauli principle the Hartree-Fock approximation was proposed by writing the wavefunction Ψ as an antisymmetrized product of orbitals explicitly. The Hartree-Fock wavefunction Ψ_{HF} amounts to a linear combination of the terms in Eq. (2.8) including all permutations of the electron coordinates with the corresponding

weights ± 1, which can be expressed as a Slater determinant,

$$\Psi_{HF} = \frac{1}{\sqrt{N!}} \begin{vmatrix} \psi_1(\mathbf{x}_1) & \psi_1(\mathbf{x}_2) & \cdots & \psi_1(\mathbf{x}_N) \\ \psi_2(\mathbf{x}_1) & \psi_2(\mathbf{x}_2) & \cdots & \psi_2(\mathbf{x}_N) \\ \vdots & \vdots & \vdots & \vdots \\ \psi_N(\mathbf{x}_1) & \psi_N(\mathbf{x}_2) & \cdots & \psi_N(\mathbf{x}_N) \end{vmatrix}. \tag{2.11}$$

The Hartree-Fock energy can be evaluated by taking the expectation value of the Hamiltonian with respect to the Slater determinant Eq. (2.11). This yields

$$\begin{aligned} E_{HF} &= \langle \Psi_{HF} | \hat{H} | \Psi_{HF} \rangle \\ &= \sum_{i=1}^{N} \int \psi_i^*(\mathbf{r}) \left(-\frac{1}{2}\nabla^2 + v_{ext}(\mathbf{r}) \right) \psi_i(\mathbf{r})\, d\mathbf{r} \\ &+ \frac{1}{2} \sum_{i=1}^{N} \sum_{j=1}^{N} \int \int \frac{|\psi_i(\mathbf{r}_1)|^2 |\psi_j(\mathbf{r}_2)|^2}{|\mathbf{r}_1 - \mathbf{r}_2|}\, d\mathbf{r}_1 d\mathbf{r}_2 \\ &- \frac{1}{2} \sum_{i=1}^{N} \sum_{j=1}^{N} \int \int \frac{\psi_i^*(\mathbf{r}_1)\psi_i(\mathbf{r}_2)\psi_j^*(\mathbf{r}_2)\psi_j(\mathbf{r}_1)}{|\mathbf{r}_1 - \mathbf{r}_2|} \delta_{s_i,s_j}\, d\mathbf{r}_1 d\mathbf{r}_2. \end{aligned} \tag{2.12}$$

The last term is of significant interest since it arises from the anti-symmetric nature of the Hartree-Fock wavefunction. It vanishes when $s_i \neq s_j$, which is a result of the Pauli exclusion principle. Therefore it is termed as exchange energy. In order to obtain the total energy of the system an extra term coming from repulsion energy between the nucleus must be added to Eq. (2.12).

In most cases, we are more concerned with the ground state of a system. Even from the ground state property of system, we could get a great deal of information on the property of excited states in room temperature since the system deviates not too much from the ground states.

To obtain the Hartree-Fock ground state energy E_0^{HF} we could minimize Eq. (2.12) with respect to the orbitals, subject to the constraint that the orbitals remain orthonormal ($\langle \psi_i | \psi_j \rangle = \delta_{ij}$). The minimization procedure carried out with the Euler-

Lagrange method yields the corresponding stationary condition given by

$$\delta\left(E_0^{HF} - \sum_{i=1}^{N}\sum_{j=1}^{N}\varepsilon_i\left(\langle\psi_i|\psi_j\rangle - 1\right)\right) = 0, \tag{2.13}$$

where ε_i is the Lagrange multiplier. The corresponding Euler equations are written as

$$\left(-\frac{1}{2}\nabla^2 + v_{ext}(\mathbf{r}) + \sum_{j=1}^{N}\int\frac{|\psi_j(\mathbf{r}')|^2}{|\mathbf{r}-\mathbf{r}'|}\,d\mathbf{r}'\right)\psi_i(\mathbf{r}) - \sum_{j=1}^{N}\int\frac{\psi_i(\mathbf{r}')\psi_j^*(\mathbf{r}')\psi_j(\mathbf{r})}{|\mathbf{r}-\mathbf{r}'|}\delta_{s_i,s_j}\,d\mathbf{r}' = \varepsilon_i\psi_i(\mathbf{r}), \tag{2.14}$$

which is called Hartree-Fock equations.

In general the Hartree-Fock equations can not be solved analytically. One exception is for the homogeneous electron gas, where the solutions are plane wave functions because of the constant external potential everywhere. Otherwise, the Hartree-Fock equations are solved using an iterative method. Because the desired orbitals are required to construct the one-electron effective potential, this process is known as the self-consistent field procedure. The self-consistent procedure starts with an initial guess for the orbitals, and successive iterations are performed with new orbitals generating the new potentials until the convergence is achieved. The converged orbitals are the ground state orbitals for that system within the Hartree-Fock approximation.

Hartree-Fock theory is not an exact theory because it only considers a single determinant for the electron wavefunction. The only case where a single determinant is the exact solution is for a non-interacting system of electrons.

In real systems the motions of electrons are more correlated than the mean-field description provided by Hartree-Fock approximation. The interaction energy missed in Hartree-Fock approximation is termed as the correlation energy E_C,

$$E_C = E_0 - E_{HF}, \tag{2.15}$$

where E_0 is the exact ground state energy. Since Hartree-Fock is a variational approach, $E^{HF} \geq E_0$ always holds and the correlation energy takes non-positive value.

A natural way to include correlation effects beyond the Hartree-Fock approximation is to represent the many-electron wavefunction as a linear combination of Slater determinants corresponding to ground state and excited states. These post Hartree-Fock methods, such as configuration interaction, coupled-cluster and Møller-Plesset theory have been extensively developed in quantum chemistry. Although the precision may be systematically improved by including more and more excited Slater determinants, the computational cost increases dramatically with the number of excitation levels. Consequently, these post Hartree-Fock approaches are limited to small systems such as atoms and small molecules.

2.3 DFT Methods

2.3.1 Overview

The main idea of density functional theory (DFT) is to describe a system composed of N interacting electrons via the electron density rather than the many-electron wavefunction like the Slater determinant used in Hartree-Fock approximation. This means that the basic variable of the system depends only on 3 spatial coordinates (x, y, and z) rather than $3N$ degrees of freedom as in Hartree-Fock approximation. Additionally, the computational costs are relatively low compared to those methods based on the complicated many-electron wavefunction such as Hartree-Fock theory and its descendants.

In 1927 Thomas and Fermi first proposed a model expressing the electronic energy as a functional of electron density.[28, 29] In the original idea they derived a differential equation for the electron density without resorting to one-electron orbitals. The DFT has its conceptual roots in the Thomas-Fermi model, but the firm theoretical foundation was set up by two Hohenberg-Kohn theorems 37 years after the proposal of Thomas-Fermi method.

2.3.2 Thomas-Fermi Model

Thomas and Fermi proposed that the electronic energy of a system can be expressed as the functional of electron density. In this idea the kinetic, exchange, and correlation contributions can be constructed from the model study on the homogeneous electron gas but should be dependent on the position. The electron density $\rho(\mathbf{r})$ is the central variable, given by

$$\rho(\mathbf{r}) = N \int \cdots \int d\mathbf{r}_2 \cdots d\mathbf{r}_N \Psi^*(\mathbf{r}, \mathbf{r}_2, ..., \mathbf{r}_N)\Psi(\mathbf{r}, \mathbf{r}_2, ..., \mathbf{r}_N). \tag{2.16}$$

The total energy of a system is expressed as a functional $E_{TF}[\rho(\mathbf{r})]$, which is given by

$$E_{TF}[\rho(\mathbf{r})] = C_F \int \rho(\mathbf{r})^{5/3}\, d\mathbf{r} + \int \rho(\mathbf{r}) v_{ext}(\mathbf{r})\, d\mathbf{r} + \frac{1}{2}\int\int \frac{\rho(\mathbf{r}_1)\rho(\mathbf{r}_2)}{|\mathbf{r}_1 - \mathbf{r}_2|}\, d\mathbf{r}_1 d\mathbf{r}_2. \quad (2.17)$$

The first term in Eq. (2.17) is the electronic kinetic energy associated with non-interacting homogeneous electron gas. This form could be obtained by integrating the kinetic energy density of a homogeneous electron gas $t_0[\rho(\mathbf{r})]$,

$$T^{TF}[\rho(\mathbf{r})] = \int t_0[\rho(\mathbf{r})]\, d\mathbf{r}, \quad (2.18)$$

where $t_0[\rho(\mathbf{r})]$ is obtained by summing all of the free electron energy states $\varepsilon_k = \frac{k^2}{2}$, up to the Fermi wave vector $k_F = [3\pi^2\rho(\mathbf{r})]^{1/3}$,

$$t_0[\rho(\mathbf{r})] = \frac{2}{8\pi^3}\int \frac{k^2}{2} n_k\, d\mathbf{k} = \frac{1}{2\pi}\int_0^{k_F} k^4\, dk \quad (2.19)$$

with n_k is the density of states in reciprocal space. This leads to the form given in Eq. (2.17) with coefficient $C_F = \frac{3}{10}(3\pi^2)^{2/3}$. The second term is the classical electrostatic energy of attraction between the nucleus and the electrons, where $v_{ext}(\mathbf{r})$ is the static Coulomb potential arising from the nucleus

$$v_{ext}(\mathbf{r}) = -\sum_{\alpha=1}^{M} \frac{Z_\alpha}{|\mathbf{r} - \mathbf{R}_\alpha|}. \quad (2.20)$$

Finally, the third term in Eq. (2.17) represents the electron-electron interactions of the system. In the Thomas-Fermi model this term contains only the classical Coulomb repulsion energy between electrons, known as the Hartree energy.

In order to obtain the ground state density and energy of a system, we may minimize the Thomas-Fermi energy functional of Eq. (2.17) with constraint of conserved total number of electrons N. Applying the Euler-Lagrange method to Eq. (2.17) leads to the stationary condition

$$\delta\left\{E_{TF}[\rho(\mathbf{r})] - \mu\left(\int \rho(\mathbf{r})\, d\mathbf{r} - N\right)\right\} = 0, \quad (2.21)$$

which yields the so-called Thomas-Fermi equations

$$\frac{5}{3}C_F\rho(\mathbf{r})^{2/3} + v_{ext}(\mathbf{r}) + \int \frac{\rho(\mathbf{r}')}{|\mathbf{r} - \mathbf{r}'|}\, d\mathbf{r}' - \mu = 0, \quad (2.22)$$

which can be solved directly to obtain the ground state density.

Thomas-Fermi theory suffers from many difficulties. One of them is that it does not predict bonding between atoms, so molecules and solids can not exist in this theory. The main source of error is a crude approximation for the kinetic energy. The kinetic energy represents a substantial portion of the total energy of a system and so even small errors prove disastrous. Another shortcoming is the oversimplified description of the electron-electron interactions, which are treated classically and so do not take into account quantum mechanical effects such as the exchange interaction.

Shortly after the introduction of Thomas-Fermi theory, Dirac[30] developed an approximation for the exchange interaction based on the homogeneous electron gas. The resulting formula is simple, and is also a local functional of the density,

$$E_X[\rho(\mathbf{r})] = -C_X \int \rho(\mathbf{r})^{4/3}\, d\mathbf{r} \tag{2.23}$$

with $C_X = \frac{3}{4}\left(\frac{3}{\pi}\right)^{1/3}$. When exchange interaction is treated like Eq. (2.23), the theory is called Thomas-Fermi-Dirac Model. Correlation can also be easily included by using any local approximation derived from homogeneous electron gas. One commonly used was proposed by Wigner[31],

$$E_C[\rho(\mathbf{r})] = -0.056 \int \frac{\rho(\mathbf{r})^{4/3}}{0.079 + \rho(\mathbf{r})^{1/3}}\, d\mathbf{r}. \tag{2.24}$$

The Thomas-Fermi model was actually too crude, mainly because the approximation used for the kinetic energy of the electrons was unable to sustain bound states. However, it set up the basis for the later development of density functional theory.

2.3.3 Hohenberg-Kohn Theorems

The Thomas-Fermi approach was developed in the hopes that the energy can be expressed exclusively in terms of the electron density. This idea, however, was intuitive at the time. Until 1964, Hohenberg and Kohn[32] proved two theorems that put the Thomas-Fermi model on solid mathematical grounds.

Theorem 1. *The external potential $v_{ext}(\mathbf{r})$ is determined, within a trivial additive constant, by the electron density $\rho(\mathbf{r})$.*

Let us suppose there are two different external potentials, $v_{ext,1}(\mathbf{r})$ and $v_{ext,2}(\mathbf{r})$ such that they correspond to same ground state electron density $\rho(\mathbf{r})$. Let Ψ_1 and $E_1 = \langle\Psi_1|\hat{H}_1|\Psi_1\rangle$ be the ground state wavefunction and ground state energy of the Hamiltonian $\hat{H}_1 = \hat{T} + \hat{V}_{ext,1} + \hat{V}_{ee}$. Let Ψ_2 and $E_2 = \langle\Psi_2|\hat{H}_2|\Psi_2\rangle$ be the ground state wave function and ground state energy of the Hamiltonian $\hat{H}_2 = \hat{T} + \hat{V}_{ext,2} + \hat{V}_{ee}$. We assumed that different Hamiltonians correspond to different ground state wave functions, i.e., $\Psi_1 \neq \Psi_2$. Applying the variational principle we may have:

$$E_1 < \langle\Psi_2|\hat{H}_1|\Psi_2\rangle = \langle\Psi_2|\hat{H}_2|\Psi_2\rangle + \langle\Psi_2|\hat{H}_1 - \hat{H}_2|\Psi_2\rangle \tag{2.25}$$

$$= E_2 + \int \rho(\mathbf{r})[v_{ext,1}(\mathbf{r}) - v_{ext,2}(\mathbf{r})]\, d\mathbf{r} \tag{2.26}$$

Similarly, we have

$$E_2 < \langle\Psi_1|\hat{H}_2|\Psi_1\rangle = \langle\Psi_1|\hat{H}_1|\Psi_1\rangle - \langle\Psi_1|\hat{H}_1 - \hat{H}_2|\Psi_1\rangle \tag{2.27}$$

$$= E_1 - \int \rho(\mathbf{r})[v_{ext,1}(\mathbf{r}) - v_{ext,2}(\mathbf{r})]\, d\mathbf{r} \tag{2.28}$$

Therefore adding the two inequalities leads to the result,

$$E_1 + E_2 < E_2 + E_1, \tag{2.29}$$

which is a contradiction, and as a result there can not be two different external potentials that correspond to the same electron density for the ground state, unless they differ by a trivial additive constant.

Theorem 2. *The ground state energy can be obtained variationally : the density that minimizes the total energy is the exact ground state density.*

As just shown, $\rho(\mathbf{r})$ determines $v_{ext}(\mathbf{r})$, N and $v_{ext}(\mathbf{r})$ determine $\hat{H}$ and therefore Ψ. This ultimately means Ψ is a functional of $\rho(\mathbf{r})$, and so the expectation value of any operator $\hat{O}$ is also a functional of $\rho(\mathbf{r})$, i.e.,

$$O[\rho(\mathbf{r})] = \langle \Psi[\rho(\mathbf{r})] | \hat{O} | \Psi[\rho(\mathbf{r})] \rangle. \tag{2.30}$$

Assume we have $\rho'(\mathbf{r})$, which determines its own $v'_{ext}(\mathbf{r})$ and wavefunction Ψ'. Then Ψ' could be taken as a trial function for the system of interest having external potential v_{ext} and corresponding $\rho(\mathbf{r})$. Thus,

$$\langle \Psi' | \hat{H} | \Psi' \rangle = \langle \Psi' | \hat{T} | \Psi' \rangle + \langle \Psi' | \hat{V}_{ee} | \Psi' \rangle + \langle \Psi' | \hat{V}_{ext} | \Psi' \rangle = E[\rho'(\mathbf{r})] \geq E[\rho(\mathbf{r})] \tag{2.31}$$

based on the variational argument.

2.3.4 Kohn-Sham Formulation

Although the Hohenberg-Kohn theorems are extremely powerful, they do not offer a way to calculate the ground state density of a system in practice. About one year after the seminal DFT paper by Hohenberg and Kohn, Kohn and Sham (KS)[33] devised a simple method for carrying out DFT calculations, that retains the exact nature of DFT. Since the electron density is the central variable rather than the wavefunction, we could construct our electron density from orbitals which are obtained from easily solved system such as the non-interacting system. The Kohn-Sham formulation centers on mapping the full interacting system with the real potential, onto a fictitious non-interacting system where the electrons are moving in an effective single-particle KS potential $v_{KS}(\mathbf{r})$. The Kohn-Sham method is still exact since it yields the same ground state electron density as the real system, but greatly facilitates the calculation.

First consider the variational problem presented in the second Hohenberg-Kohn theorem. The ground state energy of a many electron system can be obtained by minimizing the energy functional, subject to the constraint that the number of electrons N is conserved, which leads to

$$\delta\left[F[\rho(\mathbf{r})] + \int v_{ext}(\mathbf{r})\rho(\mathbf{r})\,d\mathbf{r} - \mu\left(\int \rho(\mathbf{r})\,d\mathbf{r} - N\right)\right] = 0, \tag{2.32}$$

where $F[\rho(\mathbf{r})] = T[\rho(\mathbf{r})] + V_{ee}[\rho(\mathbf{r})]$ is called universal functional since they do not depend on the external potentials. The Euler equation is given by

$$\mu = \frac{\delta F[\rho(\mathbf{r})]}{\delta\rho(\mathbf{r})} + v_{ext}(\mathbf{r}), \tag{2.33}$$

where μ is the Lagrange multiplier associated with the constraint of conserved N. The idea of Kohn and Sham was to set up a system where the kinetic energy could be determined exactly, since this was a major problem in Thomas-Fermi theory. This

was achieved by resorting to a non-interacting system of electrons. The corresponding ground state wavefunction Ψ_{KS} for this type of system is given exactly by a determinant of single-particle orbitals $\psi_i(\mathbf{r}_i)$,

$$\Psi_{KS} = \frac{1}{\sqrt{N!}}\det[\psi_1(\mathbf{r}_1)\psi_2(\mathbf{r}_2)...\psi_N(\mathbf{r}_N)]. \tag{2.34}$$

The universal functional $F[\rho(\mathbf{r})]$ was then partitioned into three terms, the first two of which are known exactly and constitute the majority of the energy, the third being a small unknown quantity,

$$F[\rho(\mathbf{r})] = T_S[\rho(\mathbf{r})] + E_H[\rho(\mathbf{r})] + E_{XC}[\rho(\mathbf{r})]. \tag{2.35}$$

$T_S[\rho(\mathbf{r})]$ is the kinetic energy of a non-interacting electron gas of density $\rho(\mathbf{r})$, $E_H[\rho(\mathbf{r})]$ is the Hartree energy of the electrons

$$E_H[\rho(\mathbf{r})] = \frac{1}{2}\int\int \frac{\rho(\mathbf{r}_1)\rho(\mathbf{r}_2)}{|\mathbf{r}_1 - \mathbf{r}_2|}\, d\mathbf{r}_1 d\mathbf{r}_2, \tag{2.36}$$

and $E_{XC}[\rho(\mathbf{r})]$ is the exchange correlation energy, which contains the difference between the exact and non-interacting kinetic energies and also the non-classical contribution to the electron-electron interactions, of which the exchange energy is a part. In the Kohn-Sham prescription the Euler equation now becomes

$$\mu = \frac{\delta T_S[\rho(\mathbf{r})]}{\delta\rho(\mathbf{r})} + v_{KS}(\mathbf{r}) \tag{2.37}$$

where the effective KS potential $v_{KS}(\mathbf{r})$ is given by

$$v_{KS}(\mathbf{r}) = v_{ext}(\mathbf{r}) + v_H(\mathbf{r}) + v_{XC}(\mathbf{r}) \tag{2.38}$$

with the Hartree potential $v_H(\mathbf{r})$,

$$v_H(\mathbf{r}) = \frac{\delta E_H[\rho(\mathbf{r})]}{\delta\rho(\mathbf{r})} = \int \frac{\rho(\mathbf{r}')}{|\mathbf{r} - \mathbf{r}'|}\, d\mathbf{r}', \tag{2.39}$$

and the exchange correlation potential $v_{XC}(\mathbf{r})$,

$$v_{XC}(\mathbf{r}) = \frac{\delta E_{XC}[\rho(\mathbf{r})]}{\delta\rho(\mathbf{r})}. \tag{2.40}$$

In Kohn-Sham theory the several potential terms were just rearranged to make up v_{KS}. So the density obtained when solving the fictitious non-interacting Kohn-Sham system is the same as the exact ground state density. The ground state density is obtained in turn by solving the N one-electron Schrödinger equations,

$$\left[-\frac{1}{2}\nabla^2 + v_{KS}(\mathbf{r})\right]\psi_i(\mathbf{r}) = \varepsilon_i\psi_i(\mathbf{r}), \tag{2.41}$$

where ε_i are Lagrange multiplier corresponding to the orthonormality of the N single-particle states $\psi_i(\mathbf{r})$, and the density is constructed from

$$\rho(\mathbf{r}) = \sum_{i=1}^{N} |\psi_i(\mathbf{r})|^2. \tag{2.42}$$

The non-interacting kinetic energy $T_S[\rho(\mathbf{r})]$ is therefore given by

$$T_S[\rho(\mathbf{r})] = -\frac{1}{2}\sum_{i=1}^{N}\int \psi_i^*(\mathbf{r})\nabla^2\psi_i(\mathbf{r})\, d\mathbf{r}. \tag{2.43}$$

Since $v_{KS}(\mathbf{r})$ depends on the density through the exchange correlation and Hartree potentials, the Kohn-Sham equations must be solved self-consistently as in the Hartree-Fock method. In order to handle the kinetic energy in an exact manner, N equations have to be solved in Kohn-Sham theory to obtain the set of Lagrange multiplier ε_i, as opposed to one equation that determines μ when solving for the density directly, as in the Thomas-Fermi approach. However an advantage of the Kohn-Sham method is that as the complexity of a system increases, with N increasing, the problem becomes no more difficult, only the number of single-particle equations to be solved increases.

Although exact in principle, Kohn-Sham theory is approximate in practice because of the unknown exchange correlation functional $E_{XC}[\rho(\mathbf{r})]$. An implicit definition of $E_{XC}[\rho(\mathbf{r})]$ can be given by,

$$E_{XC}[\rho(\mathbf{r})] = T[\rho(\mathbf{r})] - T_S[\rho(\mathbf{r})] + E_{ee}[\rho(\mathbf{r})] - E_H[\rho(\mathbf{r})] \tag{2.44}$$

where $T[\rho(\mathbf{r})]$ and $E_{ee}[\rho(\mathbf{r})]$ are the exact kinetic and electron-electron interaction energies respectively. The intention of Kohn and Sham was to make the unknown

contribution to the total energy of the non-interacting system as small as possible, and this is indeed the case with the exchange correlation energy, however it is still an important contribution since the binding energy of many systems is about the same size as $E_{XC}[\rho(\mathbf{r})]$, so an accurate description of exchange and correlation is crucial for the prediction of binding properties.

2.4 Exchange Correlation Approximations

2.4.1 Overview

While DFT is an exact theory of ground state properties, practical applications of DFT must be based on approximations for the unknown exchange correlation potential which describes the effects of Pauli exclusion principle and Coulomb potential beyond the pure electrostatic interaction between electrons in an average sense. If the exact exchange correlation potential is obtained, the many-body problem can be solved exactly.

All exchange correlation functionals can be written in a general form

$$E_{XC}[\rho(\mathbf{r})] = \int \rho(\mathbf{r})\varepsilon_{XC}(\mathbf{r})\, d\mathbf{r}, \tag{2.45}$$

where $\varepsilon_{XC}(\mathbf{r})$ is the exchange correlation energy density.

In DFT, the exchange correlation functionals can be approximated in different levels by the number and kind of their local ingredients.[34] The simplest one is the local density approximation in which only the local electron density is considered. In the high level approximation such as generalized gradient approximation (GGA), the gradient of electron density $\nabla\rho(\mathbf{r})$ is also included. We will discuss local density approximation (LDA) and GGA especially PBE with more details because these two kinds of functionals are extensively used in our simulations.

2.4.2 Local Density Approximation

In 1951, Slater[35] suggested a model in which the kinetic energy would be treated as in the Hartree-Fock model, but where the exchange term was replaced by a functional of electron density $v_X[\rho(\mathbf{r})]$. This work lead to what is known as the $X\alpha$-SCF method. In the derivation of Slater's one-electron exchange potential, we follow the

procedure of Kohn and Sham.[33]

We may begin by writing the Hartree-Fock exchange operator in the form of an equivalent potential acting on the kth wave function,

$$v_{xk}(\mathbf{x}) = -\sum_{k'=1}^{N} \int \frac{\psi_k^*(\mathbf{x})\psi_{k'}^*(\mathbf{x}')\psi_{k'}(\mathbf{x})\psi_k(\mathbf{x}')}{|\mathbf{r}-\mathbf{r}'|}\, d\mathbf{x}'\psi_k^*(\mathbf{x})\psi_k(\mathbf{x}). \tag{2.46}$$

Next we make an approximation and simplification assuming the wave functions can be approximated by plane waves as in free electron gas. This leads to

$$v_{xk}(\mathbf{r}) = -\frac{k_F(\mathbf{r})}{\pi}\left[1 + \frac{k_F^2(\mathbf{r}) - k^2}{2kk_F(\mathbf{r})}\right] \ln\left|\frac{k + k_F(\mathbf{r})}{k - k_F(\mathbf{r})}\right| \tag{2.47}$$

with $k_F(\mathbf{r}) = \left(3\pi^2\rho(\mathbf{r})\right)^{1/3}$. Then, we average v_{xk} over the occupied state k, which results in

$$v_X[\rho(\mathbf{r})] = -\frac{3}{2\pi}(3\pi^2)^{1/3}\rho(\mathbf{r})^{1/3}, \tag{2.48}$$

which is the original Slater's exchange potential.

Since electron density adjustments are mainly affected by redistribution of the electrons near the Fermi level, it is reasonable to take $k = k_F(\mathbf{r})$ in Eq. (2.47), which is equivalent to taking the effective exchange potential for a state at the top of the Fermi distributions. This leads to

$$v_X[\rho(\mathbf{r})] = -\frac{1}{\pi}(3\pi^2)^{1/3}\rho(\mathbf{r})^{1/3}, \tag{2.49}$$

which is the expression for exchange potential that Kohn and Sham derived in 1965. Eq. (2.49) is different from Slater's by a factor of $\frac{2}{3}$. The paper published by Kohn and Sham in 1965 is not the first addressing this difference of two-thirds. Actually in 1954, Gáspár already obtained the same kind of dependence of the exchange energy on the electron density as that of Kohn and Sham.

The model, in which $v_X[\rho(\mathbf{r})]$ is proportional to $\rho(\mathbf{r})^{1/3}$, became known as the $X\alpha$ method, where the exchange term is written in the form,

$$-\frac{3}{2\pi}\alpha(3\pi^2)^{1/3}\rho(\mathbf{r})^{1/3} \tag{2.50}$$

with $\alpha = 1$ for Slater's model and $\alpha = 2/3$ for that of Gáspár, Kohn, and Sham.

In Eq. (2.50), we only include the exchange effect. Together with this exchange potential, a commonly used correlation formula is that of Perdew and Zunger[36] which makes use of accurate quantum Monte Carlo data for the homogeneous electron gas generated by Ceperley and Alder[37] to fix the coefficients in the interpolation formula.

Our local density functional (LDF) approach employs the Gáspár-Kohn-Sham exchange potential and neglects the correlation effect. This approach is also commonly referred to as the local density approximation (LDA).

2.4.3 PBE Generalized Gradient Approximation

For exchange correlation energy the LDA makes use of the result obtained from homogeneous electron gas at each point irrespective of the non-homogeneity of the real electron density and is the simplest approximation for exchange and correlation functionals. For real system of non-homogeneous electron density the exchange correlation energy can be significantly different from that of homogeneous electron gas. The gradient and higher spatial derivatives of the electron density are needed to account for this deviation.

Perdew and colleges made great contributions on the development of GGA functionals. [34, 36, 38–42] They introduced an analytic function known as the enhancement factor, $F_{XC}[\rho(\mathbf{r}), \nabla\rho(\mathbf{r})]$, that accounts for the non-homogeneity of electron density and modifies the LDA energy density through

$$E_{XC}^{GGA}[\rho(\mathbf{r})] = \int \rho(\mathbf{r})\varepsilon_{XC}^{hom}[\rho(\mathbf{r})]F_{XC}[\rho(\mathbf{r}), \nabla\rho(\mathbf{r})]\, d\mathbf{r}. \tag{2.51}$$

Usually the GGA enhancement factor is written in terms of the Seitz radius, r_s, which is related to the electron density $\rho(\mathbf{r})$ by

$$r_s = \left(\frac{3}{4\pi\rho(\mathbf{r})}\right)^{1/3}, \tag{2.52}$$

and the dimensionless reduced density gradient $s(\mathbf{r})$,

$$s(\mathbf{r}) = \frac{|\nabla\rho(\mathbf{r})|}{2k_F(\mathbf{r})\rho(\mathbf{r})} \tag{2.53}$$

with k_F being the Fermi wave vector,

$$k_F(\mathbf{r}) = \left(3\pi^2\rho(\mathbf{r})\right)^{1/3}. \tag{2.54}$$

At present the most popular GGA functional in physics community is PBE.[38] The PBE functional E_{XC}^{PBE} is composed of two parts : PBE exchange E_X^{PBE} and PBE correlation E_C^{PBE} functionals. The exchange PBE functional is written in the following form,

$$E_X^{PBE}[\rho(\mathbf{r})] = \int d^3\mathbf{r}\rho(\mathbf{r})\varepsilon_X^{hom}(\rho)F_X(s) \tag{2.55}$$

with

$$F_X(s) = 1 + k - \frac{k}{1 + \mu s^2/k} \tag{2.56}$$

where $k = 0.804, \mu = 0.21951$. This exchange energy obeys the spin-scaling relationship,[43]

$$E_X^{PBE}[\rho_\alpha, \rho_\beta] = \frac{1}{2}E_X^{PBE}[2\rho_\alpha] + \frac{1}{2}E_X^{PBE}[2\rho_\beta]. \tag{2.57}$$

And the PBE correlation energy functional is given by

$$E_C^{PBE}[\rho_\alpha, \rho_\beta] = \int d^3\mathbf{r}\rho(\mathbf{r})[\varepsilon_C^{hom}(r_s, \zeta) + H(r_s, \zeta, t)], \tag{2.58}$$

where the non-local part $H(r_s, \zeta, t)$ depends on the parameter t including the density gradient via

$$H = \gamma\phi^3 \ln\left\{1 + \frac{\beta}{\gamma}t^2\left[\frac{1 + At^2}{1 + At^2 + A^2t^4}\right]\right\} \tag{2.59}$$

where $\beta = 0.066725, \gamma = 0.03191$, and

$$\begin{aligned}
\zeta &= (\rho_\alpha - \rho_\beta)/\rho(\mathbf{r}) \\
t &= (\pi/4)^{1/2}(9\pi/4)^{1/6}\frac{2}{\phi(\zeta)r_s^{1/4}} \\
\phi(\zeta) &= \frac{1}{2}\left[(1+\zeta)^{2/3} + (1-\zeta)^{2/3}\right] \\
A &= \frac{(\beta/\gamma)}{e^{-\varepsilon_C(r_s,\zeta)/\gamma\phi^3} - 1}.
\end{aligned}$$

The GGA takes account of the gradient of the electron density. For systems of slowly varying electron density, the GGA has proved to be an improvement over LDA. For example, GGAs lead to improvement on total energies,[44] atomization energies,[44, 45] energy barriers, and structural energy differences.[46, 47]

2.5 Gaussian Basis Sets

When molecular calculations are performed, basis functions are employed to construct the molecular orbitals, which are expanded as a linear combination of such functions with the coefficients to be determined in the self consistent procedure. A natural choice for basis functions would be Slater-type atomic orbitals decaying exponentially with distance from the nuclei. Boys[48] pointed out that these Slater-type orbitals could be approximated as linear combinations of Gaussian-type orbitals (GTOs) instead. Because it is easier to calculate overlap and other integrals involved in the construction of Hamiltonian matrix with Gaussian basis functions, this led to significant computational savings.

In Cartesian coordinate system, Gaussian primitive basis functions are defined as products of the integer powers of Cartesian coordinates and a Gaussian function:

$$\chi(\mathbf{r}, \alpha, \hat{n}) = x^{n_x} y^{n_y} z^{n_z} e^{-\alpha r^2} \tag{2.60}$$

and the corresponding normalization constant is given by

$$N(\alpha, \hat{n}) = \left(\frac{2\alpha}{\pi}\right)^{3/4} \frac{(4\alpha)^{n/2}}{\sqrt{(2n_x - 1)!!(2n_y - 1)!!(2n_z - 1)!!}} \tag{2.61}$$

with $n = n_x + n_y + n_z$.

At present, there are various basis sets composed of Gaussian-type orbitals. The smallest one are called minimal basis sets typically composed of a minimum number of basis functions required to represent all of the electrons on each atom. The most common minimal basis set is STO-nG, where n is an integer. The value of n represents the number of Gaussian primitive functions comprising a single basis function. In these basis sets, the same number of Gaussian primitives are used to construct core and valence orbitals. Minimal basis sets are usually used in testing calculations to get the rough idea.

Other more complicated basis sets are proposed to improve the quality of the minimal basis set. Based on the observation that the valence orbitals have greater effects on chemical properties, a split-valence basis set was proposed such that the number of functions used to describe the valence electrons is doubled but a single function is used for the inner shells. The notation for the split-valence basis sets is typically X-YZG. In this convention, X represents the number of primitive Gaussians comprising each core atomic orbital basis function. The Y and Z indicate that the valence orbitals are composed of two basis functions each, the first one composed of a linear combination of Y primitive Gaussian functions, the other composed of a linear combination of Z primitive Gaussian functions. For example, in the 3-21G basis set, three Gaussian functions describe the core orbitals and the valence electrons are also represented by three Gaussians of which two are used for the contracted part and one for the diffuse part.

Other improvement is the addition of polarization functions, indicated by an asterisk, $*$. Two asterisks, $**$, indicate that polarization functions are also added to light atoms (hydrogen and helium). These polarization functions have one more node. For example, the only basis function located on a hydrogen atom in a minimal basis set would be a function approximating the $1s$ atomic orbital. When polarization is added to this basis set, a p-function is also added to the basis set. This adds some extra flexibility within the basis set, effectively allowing molecular orbitals involving the hydrogen atoms to be more asymmetric about the hydrogen nucleus.

Throughout this work, we use 6-31G* split valence basis sets to model the twisted armchair graphene nanoribbons in Chapter 3. The 3-21G split valence set is used in the simulations of silicon nanowires discussed in Chapter 4. And we also use uncontracted basis sets[49] such as $7s3p$ for C atoms and $3s$ for H atoms in the study of planar graphene nanoribbons presented in Chapter 3.

2.6 Helical Band Structure Methods

For a one-dimensional system with helical symmetry such as carbon nanotubes, we can define a screw operation in terms of a translation l down the z axis in conjunction with a right-handed rotation ϕ about the z axis. That is,

$$\mathcal{S}\,\mathbf{r} = \mathcal{S}(a,\phi)\,\mathbf{r} = \begin{pmatrix} x\cos\phi - y\sin\phi \\ x\sin\phi + y\cos\phi \\ z + l \end{pmatrix}. \tag{2.62}$$

Because the symmetry group generated by the screw operation $\mathcal{S}$ is isomorphic with the one-dimensional translation group, we may have a generalized Bloch's theorem in which the one-electron wavefunctions will transform according to

$$\mathcal{S}^m \psi_i(\mathbf{r};\kappa) = e^{i\kappa m}\,\psi_i(\mathbf{r};\kappa). \tag{2.63}$$

The quantity κ is a dimensionless quantity which is conventionally restricted to $-\pi < \kappa \leq \pi$. For the case of pure translation, i.e., $\phi = 0$, κ corresponds to a normalized quasi-momentum in terms of $\kappa = kl$, where k is the traditional reciprocal wavevector.

The one-electron wavefunctions ψ_i are constructed from a linear combination of Bloch functions φ_j, which are in turn constructed from a linear combination of nuclear-centered Gaussian-type orbitals $\chi_j(\mathbf{r})$ in forms of

$$\psi_i(\mathbf{r};\kappa) = \sum_j c_{ji}(\kappa)\,\varphi_j(\mathbf{r};\kappa) \tag{2.64}$$

$$\varphi_j(\mathbf{r};\kappa) = \sum_m e^{-i\kappa m}\,\mathcal{S}^m\,\chi_j(\mathbf{r}). \tag{2.65}$$

The detailed description and formulism derivation of this helical method can be found in Ref. [50].

2.7 Landauer Approach for Quantum Conductance Calculation

The conductance calculations have been extensively discussed in literature. This section is mainly adapted from Refs. [51, 52] with more details carried out.

The transport calculations are based on phase-coherent transport of electrons through the device region from the left semi-infinite lead to the right semi-infinite lead of a linear system. In Landauer approach,[23, 24] the conductance is proportional to the transmission function as follows

$$G_{con} = \frac{2e^2}{h}T, \tag{2.66}$$

where both the conductance G_{con} and the transmission function T are functions of energy E. T represents the probability that an electron injected at one end of the conductor will emit at the other end. The transmission function T of the device can be expressed in terms of the Green's functions of the conductor and the coupling of the conductor to the leads,

$$T = \mathrm{Tr}[\Gamma_L G^R \Gamma_R G^A], \tag{2.67}$$

where the advanced Green's function G^A is the Hermitian conjugate of the retarded Green's function G^R of the conductor describing the dynamics of the electrons inside the conductor, and the $\Gamma_{\{L,R\}}$ accounts for the coupling of the conductor to the leads.

To compute the Green's function of the conductor we could start with the retarded Green's function of the whole system including the conductor and two semi-infinite leads,

$$(\varepsilon - H)G = I, \tag{2.68}$$

where $\varepsilon = E + i\eta$ (η is an arbitrarily small positive real number) is a complex energy, I is the identity matrix, and we neglect the superscript in G for simplicity. Since the whole system can be conceptually divided into three distinct regions : a conductor

region, a left-hand lead, and a right-hand lead, Eq. (2.68) can be expressed in terms of sub-matrices that correspond to different subsystems,

$$\begin{pmatrix} (\varepsilon - H_L) & h_{LC} & 0 \\ h_{LC}^{\dagger} & (\varepsilon - H_C) & h_{CR} \\ 0 & h_{CR}^{\dagger} & (\varepsilon - H_R) \end{pmatrix} \begin{pmatrix} G_L & G_{LC} & G_{LCR} \\ G_{CL} & G_C & G_{CR} \\ G_{LRC} & G_{RC} & G_R \end{pmatrix} = I. \tag{2.69}$$

Since we are more concerned with the Green's function of conductor, the equations involving the G_C can be written explicitly as follows :

$$(\varepsilon - H_L)G_{LC} + h_{LC}G_C + 0 = 0 \tag{2.70}$$

$$h_{LC}^{\dagger}G_{LC} + (\varepsilon - H_C)G_C + h_{CR}G_{RC} = I \tag{2.71}$$

$$0 + h_{CR}^{\dagger}G_C + (\varepsilon - H_R)G_{RC} = 0 \tag{2.72}$$

From Eq. (2.72) we have

$$G_{RC} = -(\varepsilon - H_R)^{-1}h_{CR}^{\dagger}G_C. \tag{2.73}$$

From Eq. (2.71) we get

$$G_{LC} = -(\varepsilon - H_L)^{-1}h_{LC}G_C. \tag{2.74}$$

Substituting the expressions for G_{RC} and G_{LC} into Eq. (2.72) leads to

$$-h_{LC}^{\dagger}(\varepsilon - H_L)^{-1}h_{LC}G_C + (\varepsilon - H_C)G_C - h_{CR}(\varepsilon - H_R)^{-1}h_{CR}^{\dagger}G_C = I, \tag{2.75}$$

which suggests

$$G_C = \left[(\varepsilon - H_C) - h_{LC}^{\dagger}(\varepsilon - H_L)^{-1}h_{LC} - h_{CR}(\varepsilon - H_R)^{-1}h_{CR}^{\dagger}\right]^{-1}. \tag{2.76}$$

Then we can write the expression of the retarded Green's function of a system as

$$G^R = [(\varepsilon - H_C) - \Sigma_L^R - \Sigma_R^R]^{-1} \tag{2.77}$$

where $\Sigma_{\{L,R\}}^R$ is the retarded self-energy terms describing the coupling between the conductor and semi-infinite leads, and is given by

$$\Sigma_L^R = h_{LC}^{\dagger}g_L^R h_{LC}, \Sigma_R^R = h_{CR}g_R^R h_{CR}^{\dagger} \tag{2.78}$$

with g_L^R and g_R^R are the Green's functions of the semi-infinite leads $(\varepsilon - H_L)^{-1}$ and $(\varepsilon - H_R)^{-1}$, respectively. The self-energy term can be viewed as an effective Hamiltonian term coming from the interaction of the conductor with leads. The coupling matrices $\Gamma_{\{L,R\}}$ can be easily obtained as

$$\Gamma_{\{L,R\}} = i[\Sigma^R_{\{L,R\}} - \Sigma^A_{\{L,R\}}], \tag{2.79}$$

where the advanced self-energy $\Sigma^A_{\{L,R\}}$ is the Hermitian conjugate of the retarded self-energy $\Sigma^R_{\{L,R\}}$.

The core of the problem lies in the calculation of the Green's functions of the semi-infinite leads. The lead Green's function in an orthogonal localized-orbital Hamiltonian can be computed with an efficient principal layer method and we take the right-hand side lead as an example.

With increasing the distance between two localized orbitals, the overlap and interaction matrix elements are smaller and smaller. Beyond some length, the elements could be considered as zero. So the semi-infinite lead can be viewed as an infinite stack of principal layers with only nonzero nearest-neighbor interactions. This corresponds to transforming the original system into a linear chain of principal layers. Within this approach, the Green's function equation for right-hand lead can be expressed as

$$\begin{pmatrix} \varepsilon - H_{00} & H_{01} & 0 & 0 & \cdots \\ H_{01}^\dagger & \varepsilon - H_{11} & H_{12} & 0 & \cdots \\ 0 & H_{12}^\dagger & \varepsilon - H_{22} & H_{23} & \cdots \\ 0 & 0 & H_{32}^\dagger & \varepsilon - H_{33} & \cdots \\ \vdots & \vdots & \vdots & \vdots & \cdots \end{pmatrix} \begin{pmatrix} G_{00} & G_{01} & G_{02} & G_{03} & \cdots \\ G_{10} & G_{11} & G_{12} & G_{13} & \cdots \\ G_{20} & G_{21} & G_{22} & G_{23} & \cdots \\ G_{30} & G_{31} & G_{32} & G_{33} & \cdots \\ \vdots & \vdots & \vdots & \vdots & \cdots \end{pmatrix}$$

$$= \begin{pmatrix} I & 0 & 0 & 0 & \cdots \\ 0 & I & 0 & 0 & \cdots \\ 0 & 0 & I & 0 & \cdots \\ 0 & 0 & 0 & I & \cdots \\ \vdots & \vdots & \vdots & \vdots & \vdots \end{pmatrix} \tag{2.80}$$

which can be expanded explicitly as follows

$$\begin{aligned} (\varepsilon - H_{00})G_{00} &= I + H_{01}G_{10} \\ (\varepsilon - H_{00})G_{10} &= H_{01}^{\dagger}G_{00} + H_{01}G_{20} \\ &\cdots \\ (\varepsilon - H_{00})G_{n0} &= H_{01}^{\dagger}G_{n-1,0} + H_{01}G_{n+1,0} \end{aligned} \tag{2.81}$$

where H_{nm} and G_{nm} are the matrix elements of the Hamiltonian and Green's function between the layer orbitals, and we assume that in a bulk system $H_{00} = H_{11} = \cdots$ and $H_{01} = H_{12} = \cdots$. In the iterative method proposed by Lopez-Sancho *et al.*,[53, 54] this chain can be transformed such than the Green's function of an individual layer can be expressed in terms of Green's function of the preceding (or following) one. This is achieved by introducing transfer matrices T and $\bar{T}$, defined such that $G_{10} = TG_{00}$ and $G_{00} = \bar{T}G_{10}$. The transfer matrix can be easily computed from the Hamiltonian matrix elements via an iterative procedure. T and $\bar{T}$ can be written as

$$T = t_0 + \tilde{t}_0 t_1 + \tilde{t}_0\tilde{t}_1 t_2 + \cdots + \tilde{t}_0\tilde{t}_1\tilde{t}_2\cdots t_n$$
$$\bar{T} = \tilde{t}_0 + t_0 + t_0 t_1 \tilde{t}_2 + \cdots + t_0 t_1 t_2 \cdots \tilde{t}_n$$

where t_i and $\tilde{t}_i$ are defined via the recursion formulas

$$t_i = (I - t_{i-1}\tilde{t}_{i-1} - \tilde{t}_{i-1}t_{i-1})^{-1} t_{i-1}^2$$
$$\tilde{t}_i = (I - t_{i-1}\tilde{t}_{i-1} - \tilde{t}_{i-1}t_{i-1})^{-1} \tilde{t}_{i-1}^2$$

with initial values

$$t_0 = (\varepsilon - H_{00})^{-1} H_{01}^{\dagger}$$

$$\tilde{t}_0 = (\varepsilon - H_{00})^{-1} H_{01}$$

The process is repeated until $t_n, \tilde{t}_n \leq \delta$ with δ arbitrarily small. In our calculations, we fixed δ at 10^{-6}.

We always order the basis function from left to right in the matrix. Since there is only non-negligible interaction between the conductor and the surface layer close to the conductor, only the top-left block G_{00} in Eq. (2.80) is needed. So the nonzero part of surface Green's function of right lead can be written as

$$g_{R,00} = G_{00} = \left[\varepsilon - H_{00} - H_{01} T\right]^{-1}. \tag{2.82}$$

and similarly the nonzero part of the surface Green's function of left lead can be written as

$$g_{L,00} = \left[\varepsilon - H_{00} - H_{01}^{\dagger} \bar{T}\right]^{-1} \tag{2.83}$$

In the case of general non-orthogonal orbitals, the above derivations still apply except the following substitutions

$$\varepsilon - H_{00} \longrightarrow \varepsilon S_{00} - H_{00}$$

$$H_{01} \longrightarrow -(\varepsilon S_{01} - H_{01})$$

where the matrix S represents the overlap between the localized orbitals.

CHAPTER 3

GRAPHENE NANORIBBONS

3.1 Introduction

Graphene has attracted a great deal of research interest since its isolation via mechanical exfoliation[1, 2] because graphene exhibits many unusual properties such as massless fermions, minimum quantum conductance, and anomalous integer quantum Hall effect occurring at half-integer filling factors.[55] In addition graphene sheets show promise for future nanoelectronic applications, such as ultrafast transistors[56] because of the high carrier mobility.[3] Graphene materials are expected to play an important role in future electronic applications and even replace silicon some day. Two-dimensional graphene, however, has a zero band gap with linear energy dispersion near the Fermi level. For practical application in the semiconductor industry a band gap could be induced by making graphene nanoribbons (GNRs) via a variety of methods such as lithographic patterning,[5] chemical vapor deposition,[6] Joule heating,[7] and unzipping the carbon nanotubes (CNTs).[8, 9]

Graphene has two major types of high symmetry structures, namely those with edges that have either armchair or zigzag configurations. Fujita, *et al.*, [57–59] carried out tight-binding studies of these systems using them as model structures to study edge defects in CNTs. It was predicted that in zigzag GNRs there were strongly localized edge states near the Fermi level, suggesting electronic structure and low-bias transport very sensitive to different edge passivations. The localized edge states were not expected in the armchair GNRs. The electronic energy gaps of armchair GNRs were calculated to have strong dependence on the ribbon widths. When we

started the project on GNRs in summer 2006, there were very few simulations done with density functional theory.[60, 61]

Most studies were focused on the planar GNRs so far. there were only several investigations addressing the torsional deformation in GNRs. Bets and Yakobson,[62] using Molecular Dynamics Simulations, found that the narrow bare GNRs prefer the twisted structure rather than the planar geometry. Hod and Scuseria[63] reported the density functional theory calculations on twisted nanoribbons of finite length and found the gap between the highest occupied molecular orbital (HOMO) and the lowest unoccupied molecular orbital (LUMO) is tunable by torsional deformation.

In this chapter, we studied the electronic structures of planar zigzag and armchair graphene nanoribbons. In addition, we investigated how the armchair graphene nanoribbons respond under applied twist about the ribbon axis.

3.2 Planar Zigzag Graphene Nanoribbons

3.2.1 Overview

Figure 3.1 depicts the model structure of a zigzag graphene nanoribbon with ribbon width $N = 6$. Here the width N refers to the number of zigzag chains along the transverse direction. In each unit cell there are $2N$ C atoms and 2 H atoms. The infinite ribbon could be obtained by repeating the unit cell framed by dashed line in Figure 3.1 periodically along two sides with translation length $l = 2.46$ Å. In our calculations we fixed the C-C bond length at 1.42 Å and C-H bond length at 1.08 Å. We define the ribbon extension direction as the z axis perpendicular to the transverse direction. The right-handed rotation ϕ of screw operation about the z axis is zero in this case. We investigated ribbons with even values of N from 6 - 20. We used a 7s3p Gaussian basis for C, a 3s basis for H,[49] and 32 κ points were evenly sampled over the central Brillouin zone.

For the zigzag graphene nanoribbons we carried out the non-spin-polarized (NSP), ferromagnetic (FM), and antiferromagnetic (AFM) calculations. The energetic trend on these states corresponding to different spin configurations was analyzed. We found the antiferromagnetic states are energetically favorable. The zigzag ribbons exhibited strongly localized edge states near the Fermi level. Our results with Gaussian basis sets are consistent with others' results obtained by using tight-binding model and density functional theory simulations with numerical atomic orbital methods. [60, 64, 65]

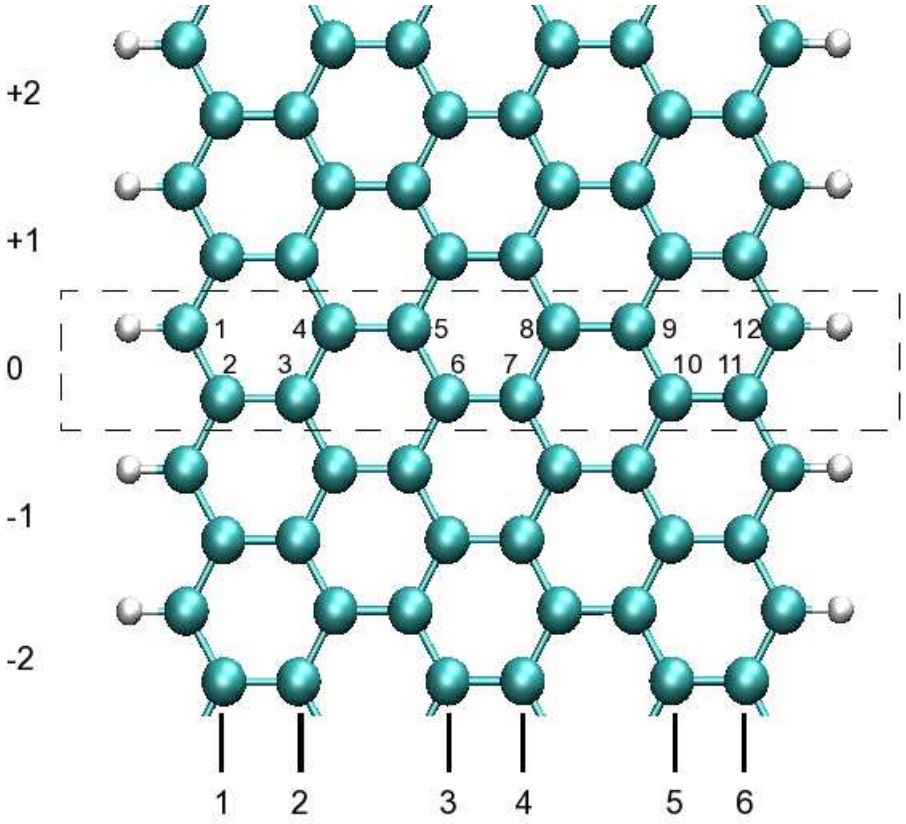

Figure 3.1: Sample zigzag GNRs with ribbon width $N = 6$. The numbering of the unit cells is shown at the left side of the ribbon with only the unit cell labeled 0 shown in their entirety. Each unit cell is composed of $2N$ C atoms and 2 H atoms. The $2N$ C atoms in unit cell 0 are numbered as shown. The index of zigzag chains is indicated at bottom from left to right.

3.2.2 Energetic Results

Figure 3.2 depicts the total energies divided by $2N$ and energy differences between different spin configurations as a function of ribbon width N. The corresponding numerical values are presented in Table 3.1. For the ribbon of same width, the antiferromagnetic state has the lowest energy and is energetically favorable. For example, for ribbon of $N = 6$, the energy of non-spin-polarized state is 0.20 meV higher than that of ferromagnetic state, which is further stabilized by about 0.032 meV in antiferromagnetic ribbon. As the ribbon width increases, the edges play a less important role and the total energies have more contributions from the bulk C atoms in the middle. So the energy difference is decreasing with increasing ribbon width. When ribbon width N approaches 20, the energy difference between FM and AFM states has already reduced to 0.00016 meV, suggesting for even bigger ribbons the preference to one of these two states is eliminated. In order to observe the AFM ground state, low temperature is needed since the thermal energy at room temperature is $K_BT = 26$ meV with $K_B = 8.617343 \times 10^{-5}$ eV/K and $T = 300$K, which will be able to excite the system and mix the various spin configurations.

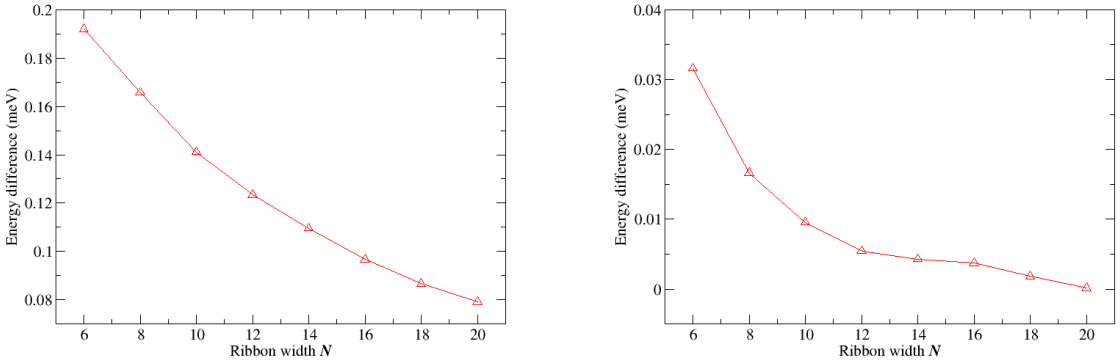

(a) (b)

Figure 3.2: (a) Total energy differences divided by $2N$ between non-spin-polarized and ferromagnetic states in zigzag GNRs as a function of ribbon width N. (b) Total energy differences divided by $2N$ between ferromagnetic and antiferromagnetic states in zigzag GNRs as a function of ribbon width N.

Table 3.1: Total energies divided by $2N$ and energy differences between different spin configurations of zigzag GNRs with various ribbon widths

width N	NSP (eV)	FM (eV)	AFM (eV)	NSP-FM (meV)	FM-AFM (meV)
6	-37.4358823900	-37.4360743104	-37.4361059109	0.191920458334	0.0316004916669
8	-37.4147775171	-37.4149432678	-37.4149598679	0.165750693746	0.0166001437520
10	-37.4021060503	-37.4022471735	-37.4022567277	0.141123230001	0.0095541400071
12	-37.3936847190	-37.3938081844	-37.3938136308	0.123465429169	0.0054464166652
14	-37.3876676725	-37.3877772624	-37.3877815346	0.109589875002	0.0042721500009
16	-37.3831570254	-37.3832537549	-37.3832574688	0.096729465625	0.0037139687521
18	-37.3796450210	-37.3797317062	-37.3797335467	0.086685177777	0.0018405499986
20	-37.3768360202	-37.3769151528	-37.3769153107	0.079132679993	0.0001578675040

3.2.3 Non-spin-polarized LDF Band Structures

In the non-spin-polarized calculations, we assumed the spin-up and spin-down states are degenerate. The typical calculated band structures are presented in Figures 3.3, 3.4, and 3.5, corresponding to the ribbon of widths $N = 6$, 8, and 10, respectively. They all exhibited nearly flat bands crossing the Fermi level. The flat region in Brillouin zone is ranging from about $\kappa = 2\pi/3$ to the zone edge, consistent with the tight-binding calculations.[57] Because the density of states is inversely proportional to the slope of the energy dispersion, the flatness in lower-lying bands generates high density of states around the Fermi level. We will show these states are localized on the ribbon edges by plotting the orbital density in real space.

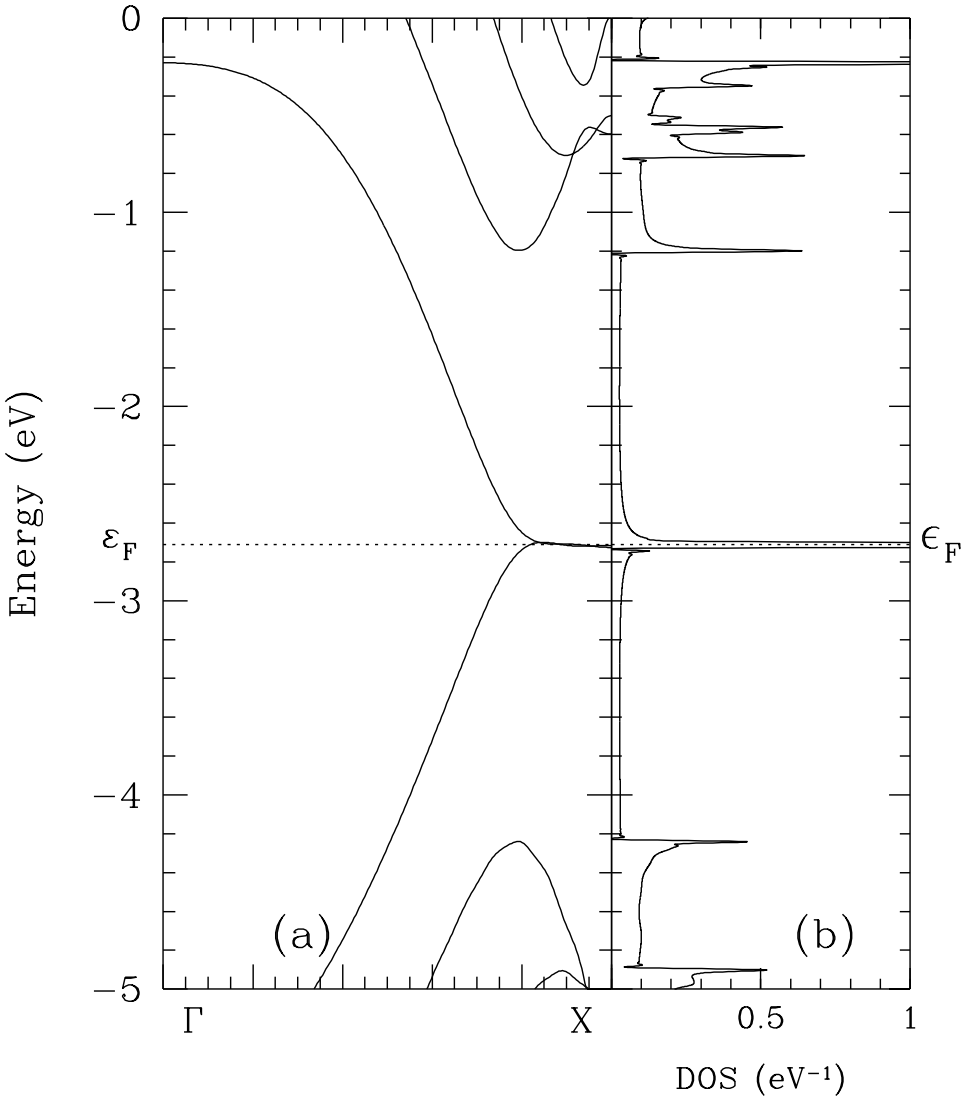

Figure 3.3: Calculated non-spin-polarized band structure and density of states of zigzag GNRs of width $N = 6$. Γ (X) corresponds to the center (edge) of the first Brillouin zone.

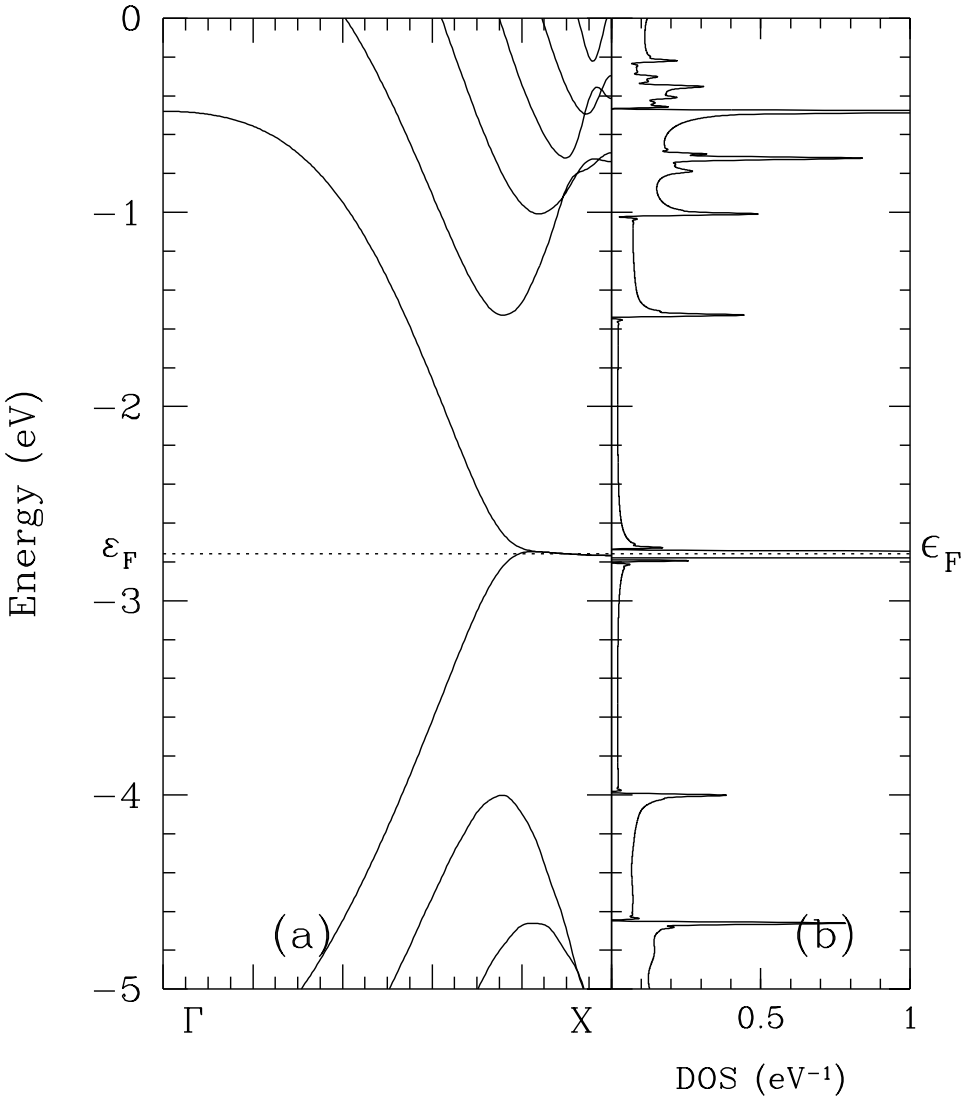

Figure 3.4: Calculated non-spin-polarized band structure and density of states of zigzag GNRs of width $N = 8$. Γ (X) corresponds to the center (edge) of the first Brillouin zone.

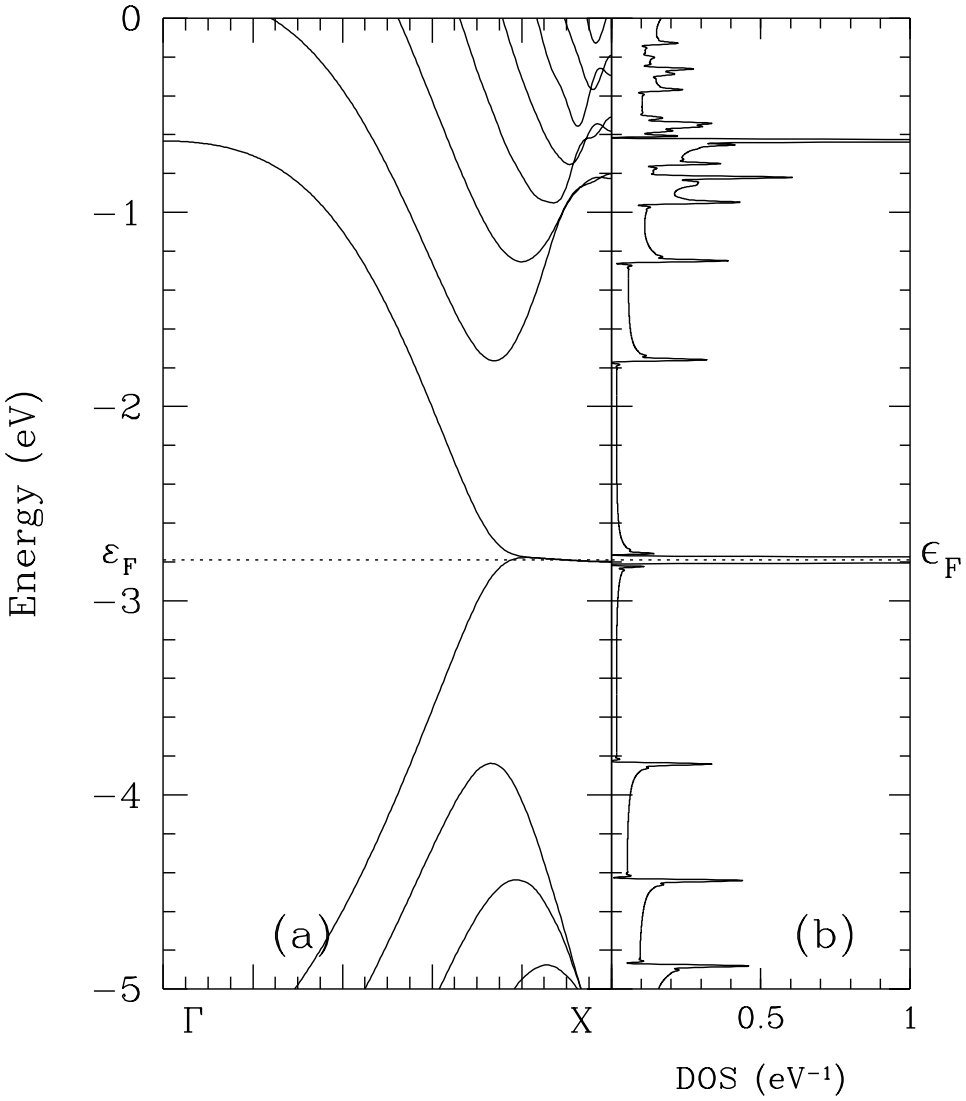

Figure 3.5: Calculated non-spin-polarized band structure and density of states of zigzag GNRs of width $N = 10$. Γ (X) corresponds to the center (edge) of the first Brillouin zone.

Figure 3.6 depicts the orbital density of zigzag GNRs of width $N = 6$. The wavevectors are sampled at 0.625π, 0.75π, 0.875π, and π in the Brillouin zone. For state at the zone edge with $\kappa = \pi$, the wavefunctions are completely localized at the edge C sites. When κ is moving away from the zone edge, the orbital density extends and decays towards the ribbon center. If $\kappa = 0.625\pi$, the states become extended across the transverse direction. Our simulation results are consistent with the previous tight-binding prediction in which the near-gap state is completely localized at the edge sites when $\kappa = \pi$, and starts to gradually penetrate into the inner sites as κ deviates from π, reaching the extended state at $\kappa = 2\pi/3$.[57]

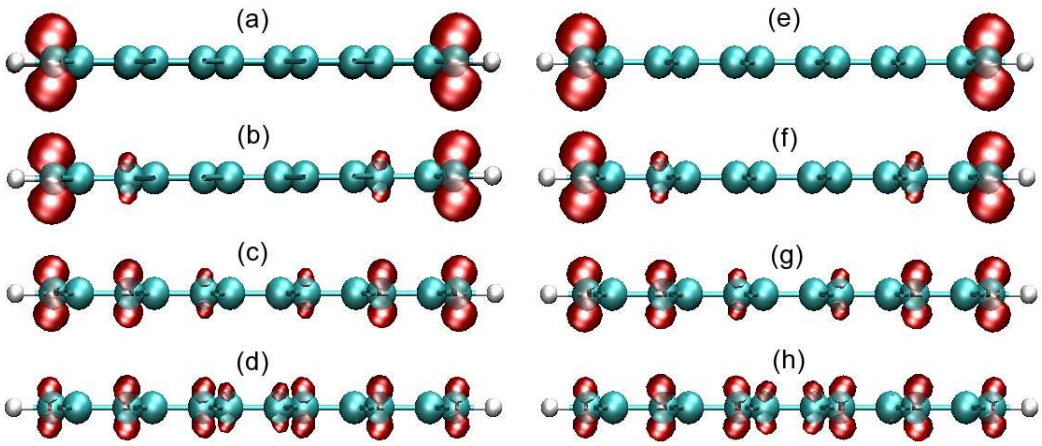

Figure 3.6: Calculated HOMO band orbital densities of zigzag GNRs of width $N = 6$, calculated at wavevectors (a) π, (b) 0.875π, (c) 0.75π, and (d) 0.625π, respectively. Calculated orbital densities for the LUMO band are given for wavevectors (e) π, (f) 0.875π, (g) 0.75π, and (h) 0.625π, respectively. The isovalue is taken to be 0.008 for all plots.

3.2.4 Ferromagnetic LDF Band Structures

If we do not apply constrains of spin degeneracy, spin-polarized calculations gave us ferromagnetic states. The typical band structures are shown in Figures 3.7, 3.8, and 3.9, corresponding to the ribbon of widths $N = 6$, 8, and 10, respectively. In this case the spin degeneracy was lifted. Compared to the non-spin-polarized results, the flat bands and the corresponding high density of states around Fermi level were not observed. Instead two peaks in density of states appeared with centers at energy points 0.3 eV above and below the Fermi level. For electron excitation, the spin-down states dominate the density of states. For hole excitation, the spin-up states contribute more.

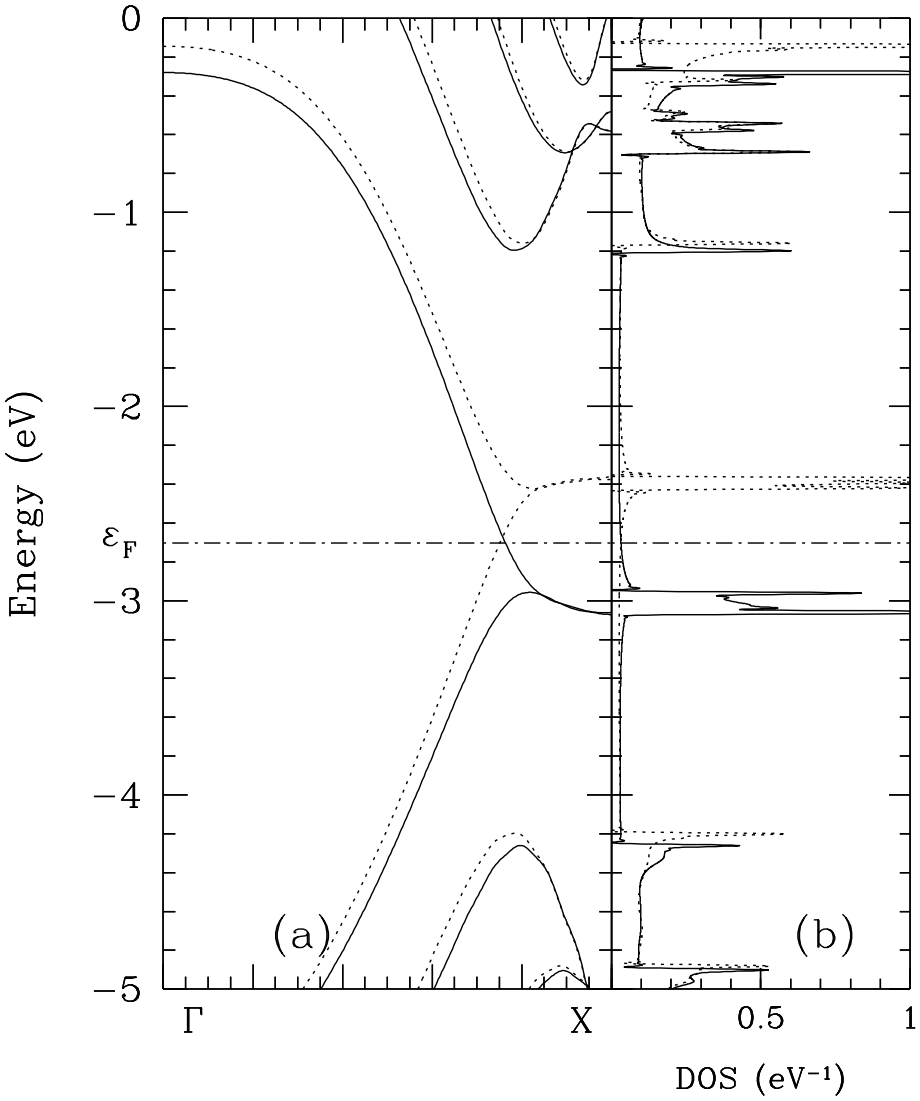

Figure 3.7: Calculated ferromagnetic band structure and density of states of zigzag GNRs of width $N = 6$. Γ (X) corresponds to the center (edge) of the first Brillouin zone.

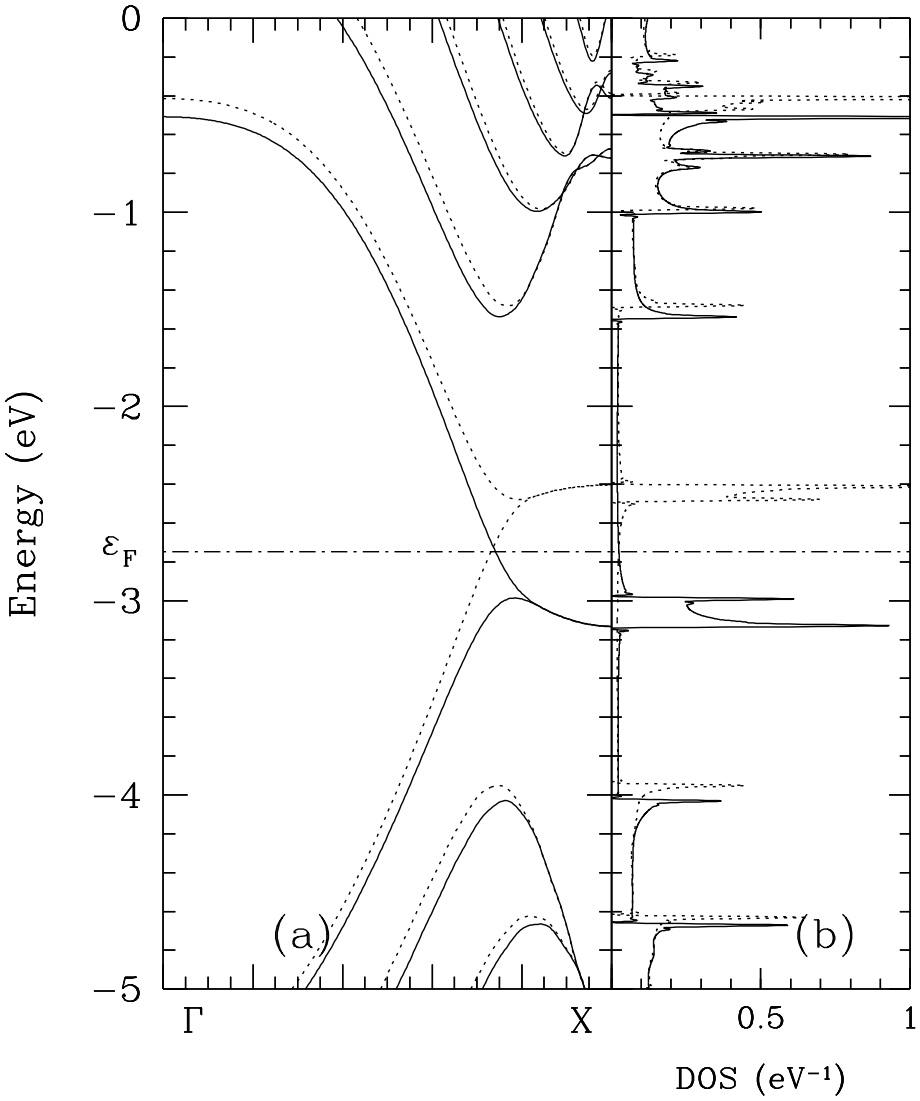

Figure 3.8: Calculated ferromagnetic band structure and density of states of zigzag GNRs of width $N = 8$. Γ (X) corresponds to the center (edge) of the first Brillouin zone.

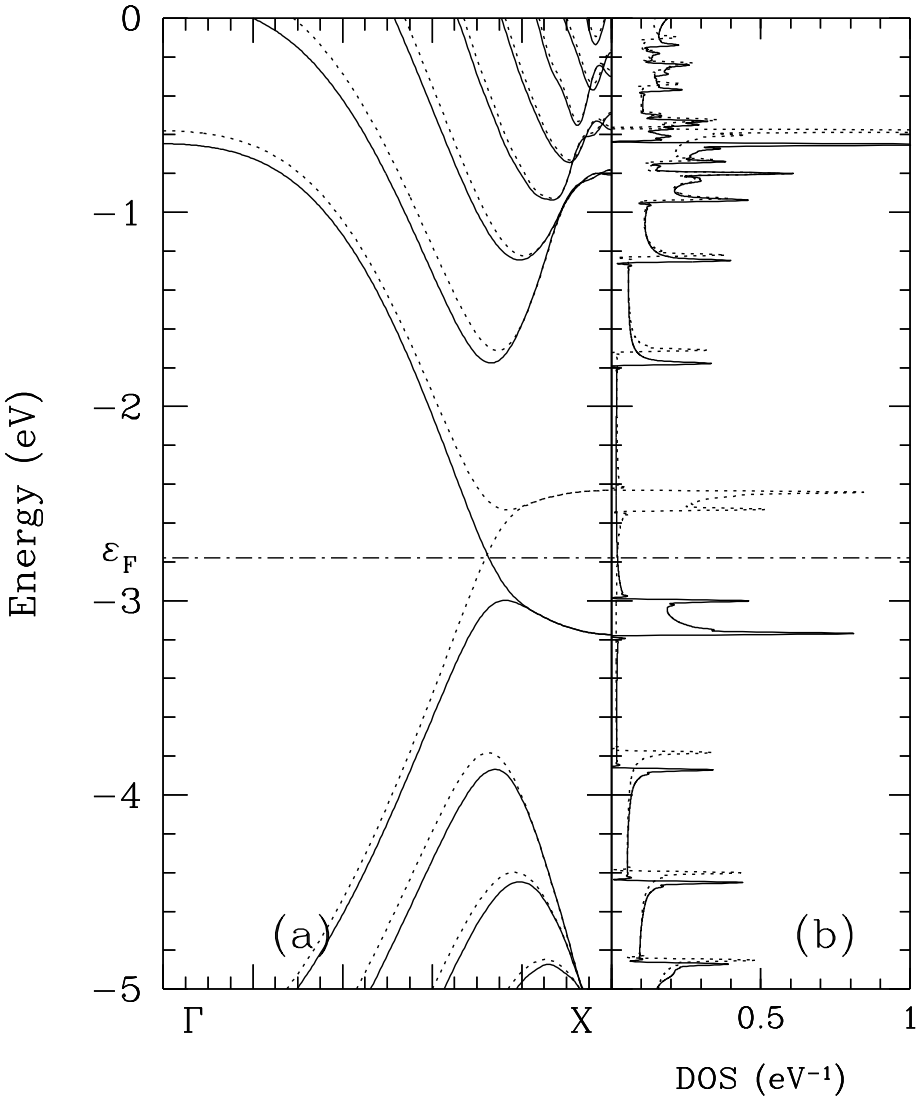

Figure 3.9: Calculated ferromagnetic band structure and density of states of zigzag GNRs of width $N = 10$. Γ (X) corresponds to the center (edge) of the first Brillouin zone.

3.2.5 Antiferromagnetic LDF Band Structures

We also carried out the calculations with constraint of applying inversion symmetry about the z axis in the exchange correlation potential. From this, we got the antiferromagnetic ground states. The typical band structures are depicted in Figures 3.10, 3.11, and 3.12, corresponding to the ribbon of widths $N = 6$, 8, and 10, respectively. In Figure 3.13 we depicts the energy gaps as a function of ribbon width N. The corresponding numerical values of gaps are listed in Table 3.2. The ribbons exhibited direct gap nature. However the gaps open up at 0.70π rather than the zone center or edge. When increasing ribbon width, the band gaps are decreasing monotonically. Our results are consistent with that of Son, *et al.*[64] In their studies, the effect of electric field was also addressed. When an electric field is applied along the transverse direction, spin-up and spin-down electrons respond in different way. The spin-up electrons are moving toward the Fermi level, leading to smaller gap even gap closure for big enough field. The spin-down electrons are moving away from the Fermi level and will not play a role in the electron transport within some voltages. The response of electrons under applied electric field renders the antiferromagnetic graphene nanoribbons a half metal.

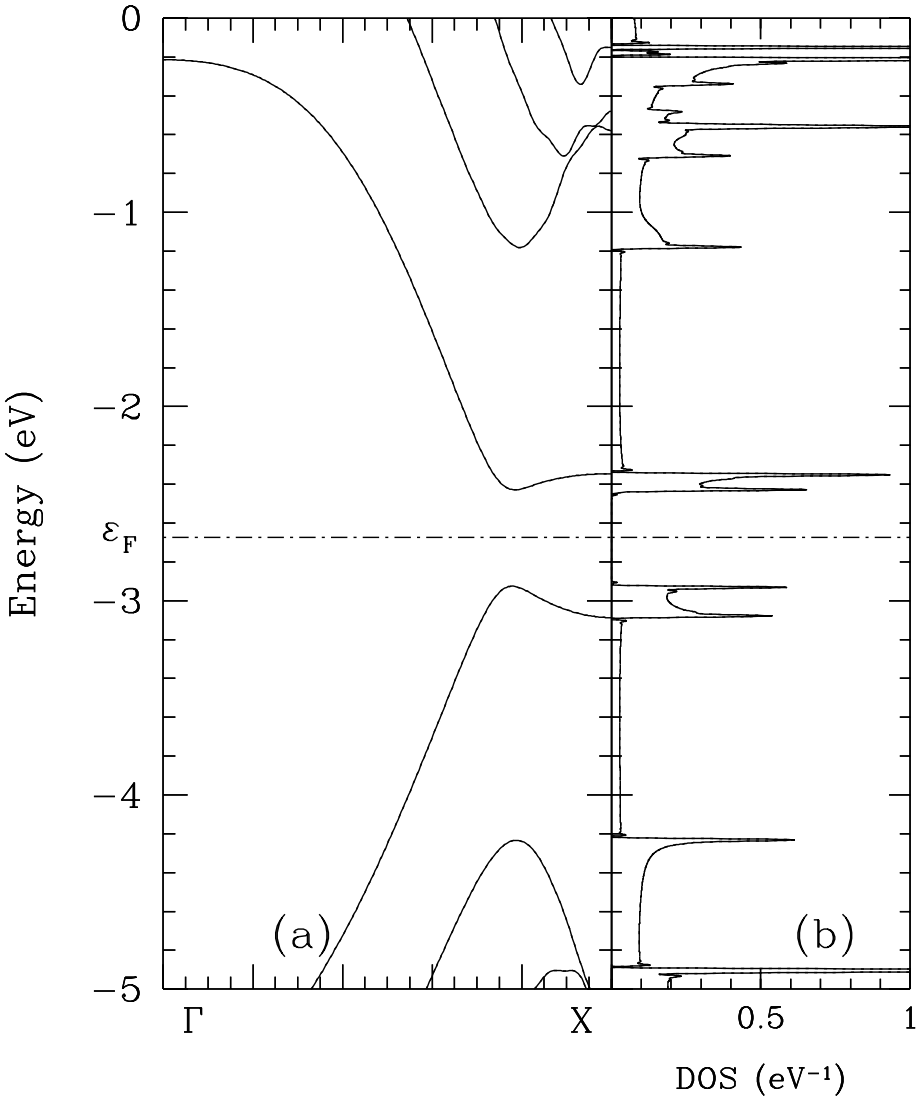

Figure 3.10: Calculated antiferromagnetic band structure and density of states of zigzag GNRs of width $N = 6$. Γ (X) corresponds to the center (edge) of the first Brillouin zone.

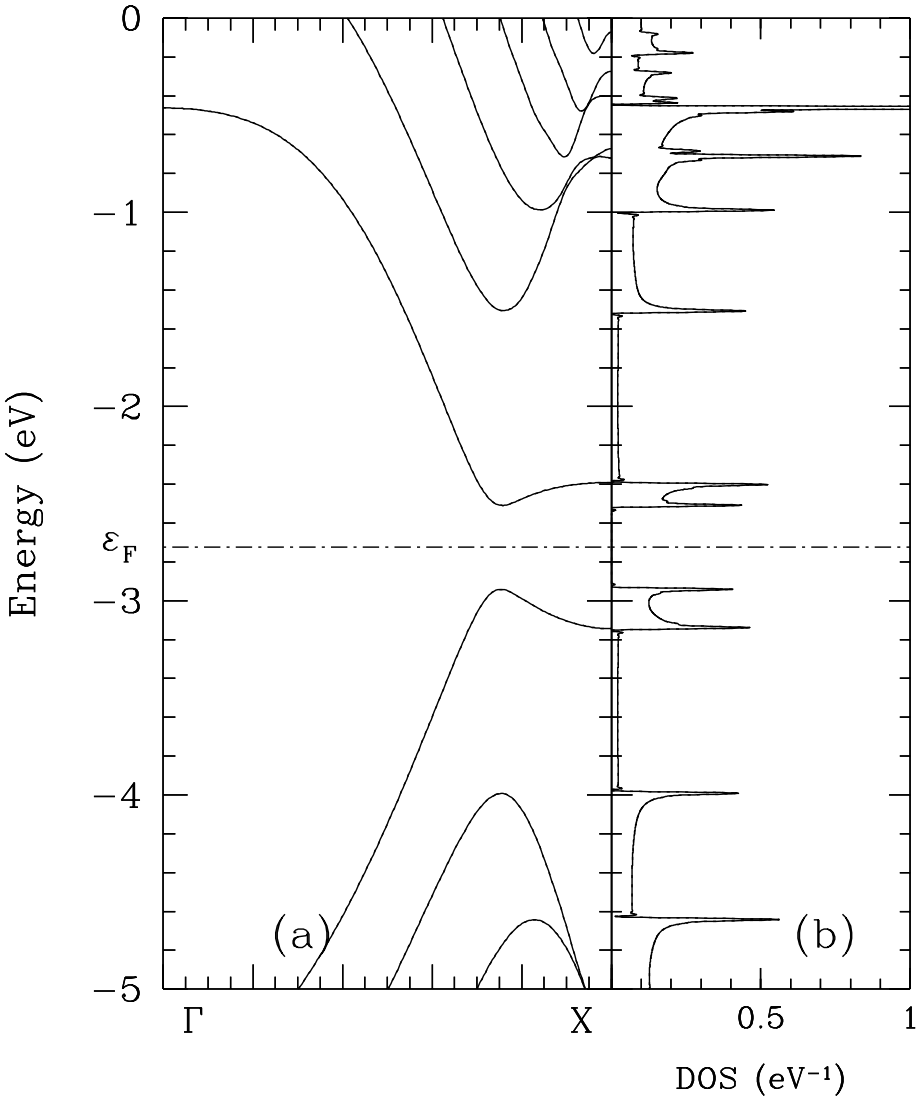

Figure 3.11: Calculated antiferromagnetic band structure and density of states of zigzag GNRs of width $N = 8$. Γ (X) corresponds to the center (edge) of the first Brillouin zone.

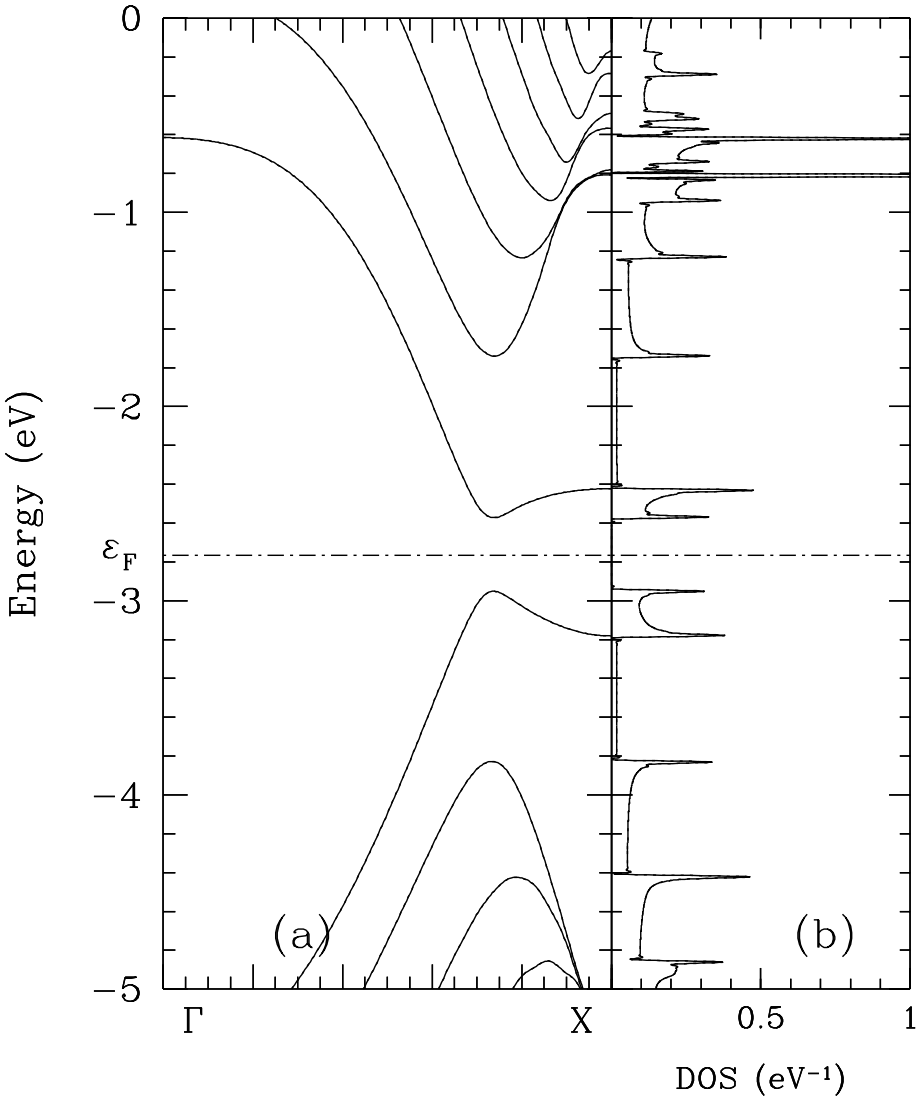

Figure 3.12: Calculated antiferromagnetic band structure and density of states of zigzag GNRs of width $N = 10$. Γ (X) corresponds to the center (edge) of the first Brillouin zone.

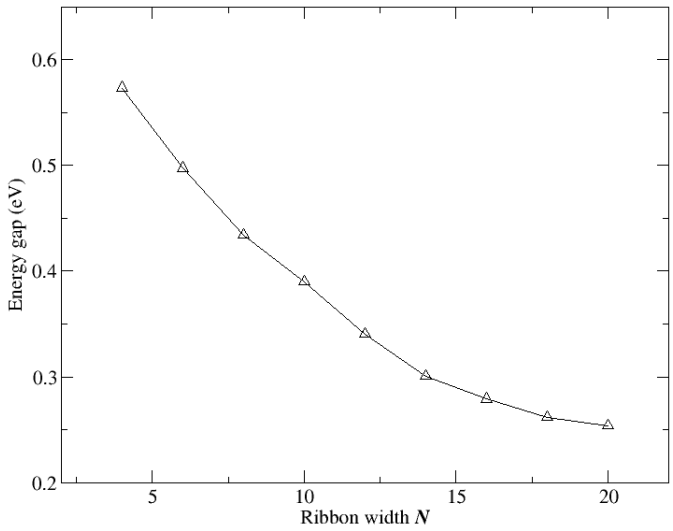

Figure 3.13: Magnitude of the HOMO-LUMO antiferromagnetic gap of the zigzag GNRs as a function of ribbon width N.

Table 3.2: Energy gaps of zigzag GNRs with various ribbon widths

Ribbon width N	Energy gap (eV)	Ribbon width N	Energy gap (eV)
4	0.5732	14	0.3008
6	0.4972	16	0.2790
8	0.4341	18	0.2618
10	0.3901	20	0.2539
12	0.3404		

3.2.6 Summary

We calculated the electronic structures of zigzag graphene nanoribbons for different spin configurations. It was found that there were localized edge states, which make the electronic properties of zigzag GNRs tunable by edge chemistry. [16, 66, 67] The zigzag GNRs exhibited ground states with two ferromagnetic edges antiferomagnetically coupled. With transverse electric field applied, the zigzag GNRs were found to be half metals,[64] which provides a suitable platform for the spintronics. This half-metallicity is further enhanced by edge-oxidization[68] and edge modifications with NO_2 and CH_3 terminations on opposite sides.[69]

3.3 Planar Armchair Graphene Nanoribbons

3.3.1 Overview

Nakada *et al.*,[58] with nearest-neighbor tight-binding model, predicted that the energy gaps of armchair GNRs are strongly dependent on the ribbon width N. If the ribbon width satisfies $N = 3m + 2$ with m being an integer, the ribbon is metallic of zero gap. Otherwise, the semiconducting energy gaps monotonically decrease with increasing ribbon widths. Our first principles results with local density functional (LDF) do not agree with the TBM prediction. Especially in our simulations, there is no metallic ribbon. In order to elucidate the discrepancy between TBM and LDF results, we introduced the third-nearest-neighbor interaction as perturbation correction to the nearest-neighbor TBM and show that the longer range interactions play an important role in describing the band gaps of armchair graphene nanoribbons.

3.3.2 Model Structure

Figure 3.14 depicts the model structure of armchair graphene nanoribbons with ribbon width $N = 7$ and 8. Here the width N is referred to as the number of dimer lines along the transverse direction. Depending on the way of constructing the whole infinite ribbon from the basic helical cell as framed by dashed line, the armchair graphene nanoribbons are classified into two categories : symmetric and staggered ribbons. For symmetric ribbons as shown in Figure 3.14 (a), the translation length l and rotation angle ϕ is 4.26 Å and 0 degree, respectively, and in each unit cell there are $2N$ C atoms and 4 H atoms. For staggered ribbons as shown in Figure 3.14 (b), the translation length l and rotation angle ϕ is 2.13 Å and 180 degrees, respectively, and each unit cell contains N C atoms and 2 H atoms. In our calculations the C-C bond length and C-H bond length are fixed at 1.42 Å and 1.08 Å, respectively.

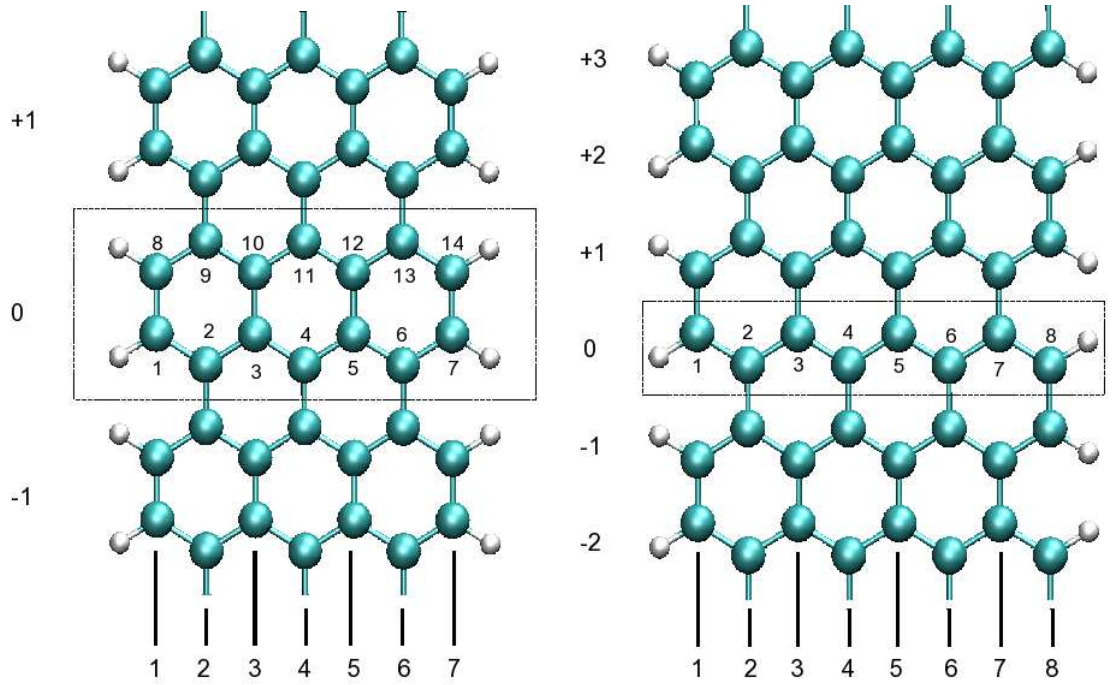

(a) (b)

Figure 3.14: (a) Symmetric armchair GNRs with ribbon width $N = 7$. Each unit cell is composed of $2N$ C atoms and 4 H atoms. (b) Staggered armchair GNRs with ribbon width $N = 8$. Each unit cell is composed of N C atoms and 2 H atoms. For (a) and (b) the numbering of the unit cells is shown at the left edge of each figure with only the unit cells labeled 0 shown in their entirety. The C atoms in unit cell 0 are numbered as shown. The index of dimer lines is indicated at bottom from left to right.

3.3.3 Local Density Functional Results

We carried out the local density functional calculations on armchair graphene nanoribbons with various widths ranging from 4 to 24. We used a 7s3p Gaussian basis for C, a 3s basis for H, and 32 κ points were evenly sampled over the central Brillouin zone.

Figure 3.15 depicts the band structures for armchair GNRs of widths $N = 7$, 8, and 9. and in Figure 3.16 we present the energy gap as a function of ribbon width N using the gap values listed in Table 3.3. In the calculations of staggered armchair GNRs, we were making use of the helical symmetry of π rotation. The presented band structures, however, have already been folded to be within the regular Brillouin zone corresponding to the translational operation. First, all ribbons are semiconductors and exhibit direct band gap with HOMO and LUMO occurring at Γ point, irrespective of the ribbon width in our study. On the other hand, the gap decreases with increasing ribbon widths. However, the variations in energy gaps have alternating pattern rather than monotonic decrease. We have relative relation of $E_{gap,\,3m+1} > E_{gap,\,3m} > E_{gap,\,3m+2}$ with m being integer.

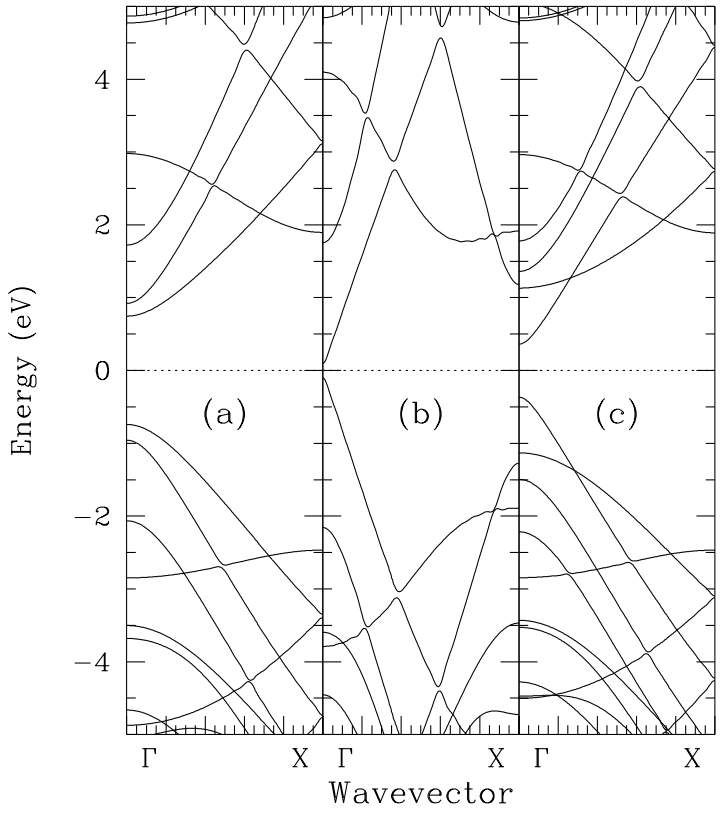

Figure 3.15: Calculated band structures of armchair GNRs of various widths. (a), (b), and (c) correspond to ribbon with $N = 7$, 8, and 9, respectively. Γ (X) indicates the center (edge) of the first Brillouin zone.

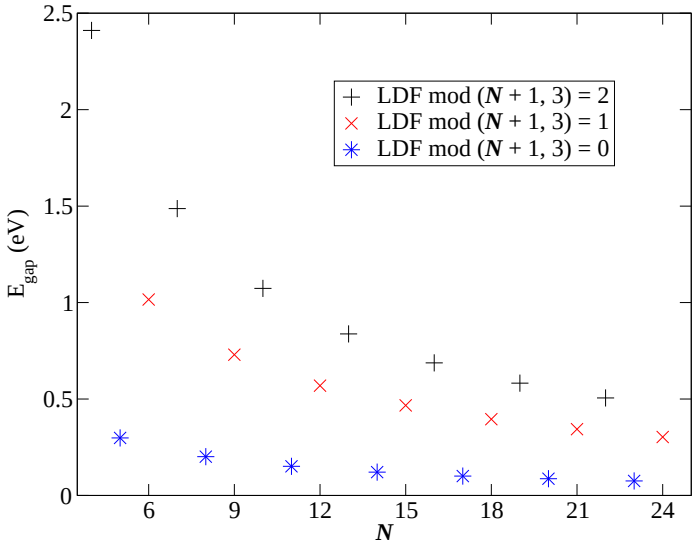

Figure 3.16: LDF energy gaps of the armchair GNRs as a function of width N.

Table 3.3: Band gaps E_{gap} of armchair GNRs with ribbon width N

N	E_{gap}(eV)	N	$E_{gap}(eV)$	N	E_{gap}(eV)	N	E_{gap}(eV)
4	2.4106	10	1.0734	16	0.6874	22	0.5055
5	0.2982	11	0.1512	17	0.1006	23	0.0752
6	1.0158	12	0.5692	18	0.3953	24	0.3030
7	1.4872	13	0.8375	19	0.5821		
8	0.2012	14	0.1210	20	0.0868		
9	0.7298	15	0.4669	21	0.3437		

3.3.4 Consideration of Longer Range Interactions

Tight-binding models were frequently used to analyze the electronic properties of semiconductors. With only nearest-neighbor interactions considered tight-binding models have been very successful in describing many properties of single-wall carbon nanotubes (SWCNTs).[22, 70–83] The geometries of SWCNTs and GNRs have great similarity because both of them can be obtained from graphene by rolling over a chiral vector or cutting along specific edges. This similarity, along with the success of TBM in SWCNTs, allow us to expect the applicability of TBM in studying GNRs. However, the LDF results are quite different from the previous predictions based on nearest-neighbor tight-binding model. In the tight-binding model, if the ribbon width N satisfies $N = 3m + 2$, then the ribbon is metallic with zero gap at Γ point where π and π^* bands crossing occurs. In addition, the band gaps of other ribbons are decreasing monotonically with increasing ribbon width.

The discrepancy motivated us to think over the validity of nearest-neighbor tight-binding model in describing the electronic property of armchair GNRs. In the previous calculations, only nearest-neighbor interactions are included. The gap openings in armchair GNRs of width $N = 3m + 2$ from our first-principles calculations, however, indicated that there were some interactions which are important but ignored in the tight-binding description.

Since the armchair GNRs can be obtained by cutting graphene along specific direction, we could apply proper boundary condition on the energy dispersion for 2D graphene, discretize the wavevector along the transverse direction, and find the energy dependence on the 1D wavevector in armchair GNRs. However, we are more concerned with the band gap instead of the energy values in whole Brillouin zone and will take a different method. The underlying procedure is described below.

The ribbons are direct band gap materials with HOMO and LUMO states occurring at $k = 0$ (see Figure 3.15). Therefore, to study the gap dependence on ribbon width we need only to consider the eigenstates of nearest-neighbor Hamiltonian $\hat{H}_0$ at $k = 0$. In the following discussion, we make use of the regular Bloch theorem to construct the wavefunctions based on the translational symmetry down the ribbon axis. So each unit cell contains two zigzag chains for symmetric and staggered armchair GNRs. We can apply the the boundary condition with vanishing nodes at the ends of zigzag chains. Then the eigenstates of $\hat{H}_0$ for the armchair GNRs with ribbon width N are given by

$$|\Psi_p^{\pm}>= \frac{1}{\sqrt{N_{cell}}}\frac{1}{\sqrt{N+1}}\sum_l\sum_{n=1}^{N}\sin(\frac{pn\pi}{N+1})(|n,l>+s|n+N,l>), \tag{3.1}$$

where $1 \leq p \leq N$, $|n,l>$ denotes the $|p_z>$ orbital associated with the nth C atom in the unit cell labeled by l in the notation of Figure 3.14, and the $s = 1$ (-1) indicates the bonding (anti-bonding) state between the wavefunctions belonging to neighboring zigzag chains. The calculated energy gap with nearest-neighbor interaction V_1 only is

$$E_{gap} = 2V_1[2\cos(\frac{p\pi}{N+1}) + s] \tag{3.2}$$

where we have : if mod(N+1,3) = 0, then $p = (N+1)/3$ and $s = -1$; if mod(N+1,3) = 1, then $p = (2N+3)/3$, and $s = 1$; and, if mod(N+1,3) = 2, then $p = (N+2)/3$, and $s = -1$. Then the band gap strongly depends on the ribbon width. The system is metallic if $N = 3q - 1$, and is semiconducting otherwise, see Figure 3.17 in which $V_1 = -2.6$ eV is assumed.

Except the nearest-neighbor interaction, longer range interactions between C atoms are neglected and may modify the band structure results of TBM. These longer range interactions can be incorporated into the TBM by adding $\hat{U}_{V_2}$ and $\hat{U}_{V_3}$ to $\hat{H}_0$, the Hamiltonian in TBM, where $\hat{U}_{V_2}$ ($\hat{U}_{V_3}$) includes all second-nearest-neighbor (third-nearest-neighbor) interactions V_2 (V_3) between C atoms in the armchair GNRs. Because V_2 and V_3 are small in magnitude compared to V_1, $\hat{U} = \hat{U}_{V_2} + \hat{U}_{V_3}$ can be

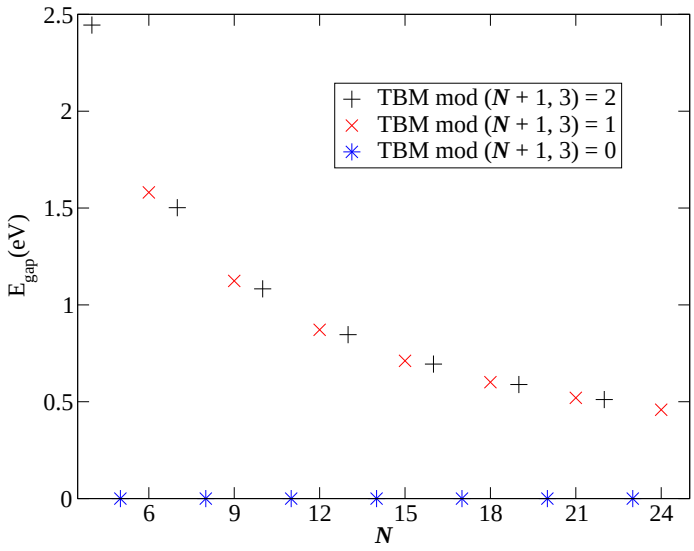

Figure 3.17: Magnitude of the HOMO-LUMO gap of the N armchair GNRs from the TBM calculations.

treated as perturbation to $\hat{H}_0$. Also, because $\hat{U}$ does not break the translational symmetry of the ribbon, it couples only states with the same k, which allows us to consider the states at $k = 0$ only.

We carried out the time-independent perturbation calculations to first order with the V_2 and V_3 as perturbation terms to V_1 and found the new expression for E_{gap} given by

$$E_{gap} = 2V_1[2\cos(\frac{p\pi}{N+1}) + s] + s\frac{2V_3}{N+1}[3 + N + 2N\cos(\frac{2p\pi}{N+1})] \qquad (3.3)$$

where we have : if mod(N+1,3) = 0, then $p = (N+1)/3$ and $s = -1$; if mod(N+1,3) = 1, then $p = (2N+3)/3$, and $s = 1$; and, if mod(N+1,3) = 2, then $p = (N+2)/3$, and $s = -1$.

The first term on the right-hand side of Eq. (3.3) is the gap arising from $\hat{H}_0$. The second term gives the lowest order correction because of $\hat{U}$. Although $\hat{U}_{V_2}$ contributes to $\hat{U}$, V_2 does not appear in Eq. (3.3) because to first order it shifts the HOMO and LUMO levels by the same amount $-3NV_2/(N+1)$.

If $N + 1 = 3m$, the first term on the right-hand side of Eq. (3.3) vanishes leaving

only the second term which reduces to

$$E_{gap} = -\frac{6V_3}{N+1}. \tag{3.4}$$

Eq. (3.4) can be used to least-squares fit to the LDF data for $N+1 = 3q$ to determine V_3 and then with V_3 fixed at this value V_1 can be determined by using Eq. (3.3) to least-squares fit to the LDF data for $N+1 \neq 3q$. Implementing this procedure yields the physically reasonable results: $V_1 = -3.2$ eV and $V_3 = -0.3$ eV, which provide an excellent fit to the LDF results for all N as shown in Figure 3.18.

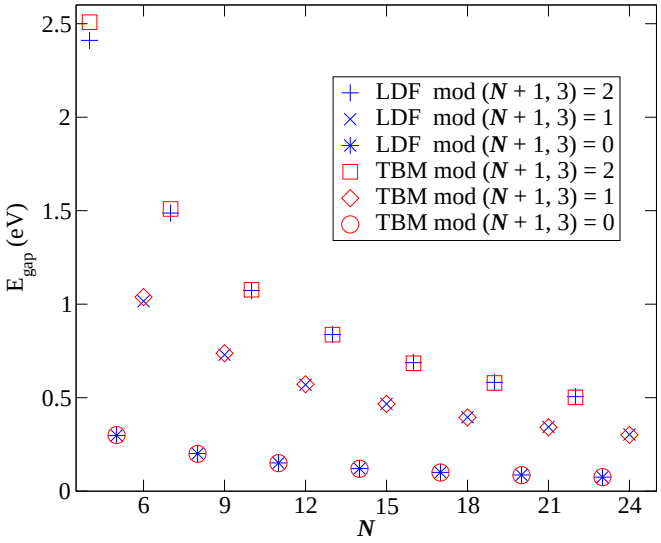

Figure 3.18: LDF results for E_{gap} compared to the corresponding tight-binding model (TBM) results obtained from Eq. (3.3) with $V_1 = -3.2$ eV and $V_3 = -0.3$ eV.

3.3.5 Summary

In our LDF simulations we fixed all C-C bond lengths at 1.42 Å and found that the armchair GNRs can be separated into three families according to the band gap dependence on ribbon width. Then we proposed an explanation by using TBM with perturbation correction from the second- and third-nearest-neighbor interactions. The non-zero semiconducting gaps in GNRs of width $N = 3q + 2$ and three families of armchair GNRs were also observed by Son, *et al.*[84] In their calculations, they carried out geometry optimization and found that the C-C distances on edges decrease leading to 12% increase of the hopping integrals between p_z orbitals of edge C atoms. After taking matrix elements change into account, they also got a TBM results which agree with their LDA calculations. Gunlycke, *et al.*[85] found that both edge contraction and third-nearest-neighbor interactions play an important role in producing good tight-binding band structures which fit the first-principles results of optimized GNRs. Experimentally, great progress has been made in preparing GNRs with widths less than 10 nm,[86, 87] which makes our theoretical calculation of more fundamental and practical significance.

3.4 Twist Effect in Electronic Properties of Armchair Graphene Nanoribbons

3.4.1 Overview

In the study of planar armchair GNRs, we show that the band gap could be engineered by controlling the ribbon width. The band gaps of nanostructures also could be tuned by other ways such as edge passivation, doping, and strain.

Strain is a powerful approach to modify the electronic structure of nanomaterial to improve device performance. The carrier mobility of silicon nanowires could be significantly enhanced by applied strain.[88] First-principles calculations have shown that for smaller diameters the band structures and gaps can be significantly modified.[89, 90]

The strain effect in graphene also attracted much attention. Ni, *et al.*[91] predicted a band-gap opening of 300 meV for graphene under 1% uniaxial tensile strain. Teague, *et al.*[92] found that the strain could modulate the local conductance of graphene. Lu and Guo,[93] using a tight-binding model, investigated armchair GNRs and found uniaxial weak strain changes the band gap in a linear fashion and large strain results in periodic oscillation of the band gap. Sun, *et al.*,[94] using GGA exchange correlation potentials, predicted that the similar oscillating behavior with linear change in each period.

For the out-of-plane strain, Hod and Scuseria[63] studied the torsional deformation effect in graphene nanoribbons of finite length. With traditional band structure codes using translational symmetry, it is hard even almost impossible to study the torsional deformation for infinite-long ribbon structure because of the huge unit cell and hence the Hamiltonian matrix of enormous size. Our HENS `parallax` code takes advantage of the helical symmetry and is well suited to the calculation of electronic structures

of the twisted quasi-one-dimensional structures.

In this section we investigated the band gaps of armchair GNRs as a function of twist angle. We found that the electronic properties of armchair GNRs are highly sensitive to the applied twist, indicating the potential application of armchair GNRs as building blocks in nanoelectromechanical devices.

3.4.2 Computational Approach

We investigated the armchair GNRs of widths $N = 8, 10, 12, ..., 18$ in this study. The representative structure of the armchair GNRs is shown in Figure 3.19. The whole ribbon can be constructed with a unit cell consisting of one zigzag chain as framed by dashed lines in Figure 3.19(a) and a screw operation acting on that unit cell, where the screw operation combines a translation l down the ribbon axis with a right-handed rotation ϕ about that same axis. In our calculations we fixed l at 2.13Å. For the planar structure, the ϕ is $180\,^\circ$. For the twisted armchair GNRs as shown in Figure 3.19(b), the torsional deformation of armchair GNRs can be represented by the relative rotation angle θ, defined as $\theta = \phi - 180\,^\circ$. The planar ribbons have symmetry operations corresponding to a reflection perpendicular to the ribbon axis and passing through the center of C-C bonds parallel to the ribbon axis. When applying the twist, the reflection symmetry of armchair GNRs is broken and only C_2 symmetry is left. All edge C atoms are passivated by H atoms to remove the dangling bands near the Fermi level. Following conventional notation, the ribbon width of armchair GNRs is defined as the number of dimer lines along the ribbon forming the width as in the preceeding section. For example, the ribbon width in Figure 3.19 is 8.

The LDF band structures were obtained by using 32 discrete points evenly sampled in the central Brillouin zone and a 6-31G* basis set. [95] Although the LDF is well-known to underestimate the band gap, we are primarily concerned with the relative change of the energy gaps under different twists.

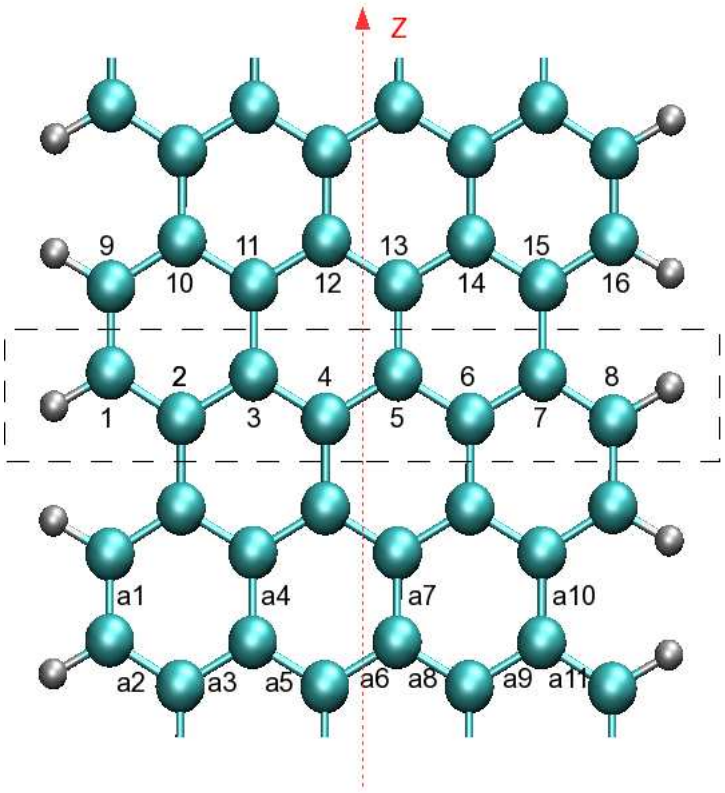

(a)

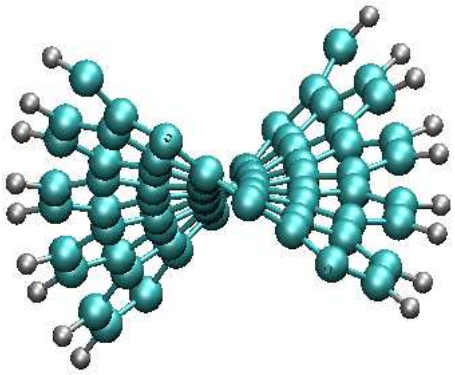

(b)

Figure 3.19: (a) Armchair GNR with width $N = 8$. Each helical unit cell is composed of one zigzag chain terminated by H atoms. The N C atoms in a helical cell are numbered as shown. The bonds are labeled as a1-a11. (b) Axial view of 10 °-twisted armchair GNR with width $N = 8$.

3.4.3 Band Structures and Near-gap Wavefunctions

We depict the electronic structures for armchair GNRs with width $N = 8$ under a series of twist angles in Figure 3.20, in which (a), (b), (c), and (d) correspond to twist angle θ equal to $0\,^\circ$, $8.5\,^\circ$, $9.0\,^\circ$, and $10\,^\circ$, respectively. In this ribbon, the top of the valence band and the bottom of the conduction band occur at the center of the one-dimensional Brillouin zone, resulting in a direct band gap at the zone center Γ point. The band gap for ribbon of width $N = 8$ is 0.40 eV for $\theta = 0$. When we apply on the ribbon torsional strain about the ribbon axis, the HOMO is raised while the LUMO is lowered if $\theta < 9.0\,^\circ$. therefore the band gap is reduced in this stage. In general two π bands cannot cross because they belong to the same irreducible representation for wave vectors not at the center or edge of the Brillouin zone. However, gap closure (accidental degeneracy) might take place at a point of high symmetry in the Brillouin zone such as the zone center or end. After the critical twist angle, the HOMO and LUMO do the inverse way, opening the band gap.

In addition to the band gap change, we also observed the twist effect on the characteristics of the bonding or antibonding states in HOMO and LUMO. Figure 3.21 depicts the wave functions of HOMO and LUMO under four different twist angles corresponding to that of Figure 3.20. According to the bonding states between the p_z orbitals of neighboring zigzag chains, there are two kinds of bonds: bonding states (BS) and antibonding states (AS). When the twist angle is smaller than $9.0\,^\circ$, the HOMO is BS state while LUMO is AS state. When the twist angle gets bigger, the characteristics of HOMO and LUMO exchanged. The energy of BS and AS states respond differently to the geometry change. Increasing bond length will lower the energy of AS state and raise the energy of BS state.

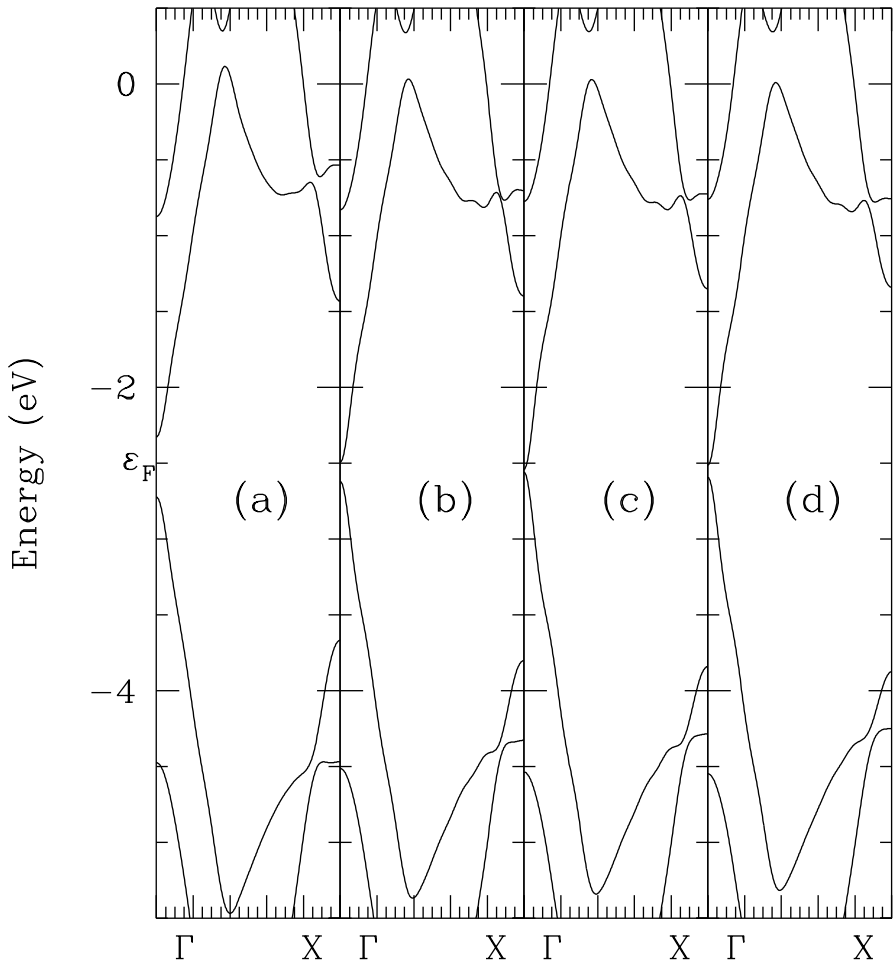

Figure 3.20: Electronic band structure of armchair GNRs (width $N = 8$) twisted by (a) 0°, (b) 8.5°, (c) 9.0°, and (d) 10.0°.

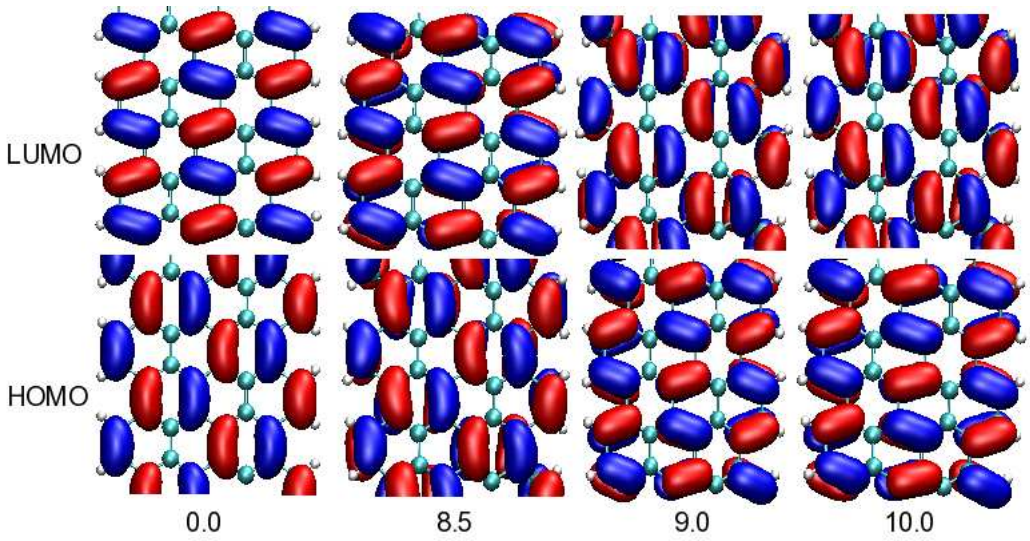

Figure 3.21: The LUMO and HOMO wave function of armchair GNRs (width $N = 8$) twisted by (a) 0 °, (b) 8.5 °, (c) 9.0 °, and (d) 10.0 °. The ribbons are vertically oriented.

3.4.4 Structure Parameters

In our simulations we carried out geometry optimization for all structures. Figure 3.22 depicts the variation of bond lengths in armchair GNRs of width $N = 8$ as a function of the twist angle. Because of symmetry in this ribbon, there are only eight nonequivalent bonds labeled by a1, a4, a7, a10 along the ribbon extension direction and by a2, a3, a5, a6 along the transverse direction. By symmetry the bonds a8, a9, and a11 are equivalent to a5, a3, and a2, respectively. Depending on the position, different bonds in a different way respond to the torsional deformation. The bonds along the transverse direction change a little bit with maximum change about 0.01 Å. The bonds connecting neighboring zigzag chains exhibit bigger change. Generally the change is increasing as bonds location move towards the ribbon edges. But the biggest bond length change of 0.045 Å occurs on a10 instead of a1 which is furthest from the ribbon center. As the twist angle approaches 9 °, some bonds exhibit abrupt change, which corresponds to the transition between the antibonding and bonding HOMOs.

In other ribbons of different widths, we observed similar bond length change as a function of twist angle and the bond equivalent to a10 has the biggest change. The bonds underlying bigger change play more important role in determining the shift of one electron energy of HOMO and LUMO. So only from the bonding (anti-bonding) states between inter-chain bonds we could acquire some idea about how the twist affects the electronic band gap of armchair GNRs. Tight-binding model could be used to carry out this analysis.

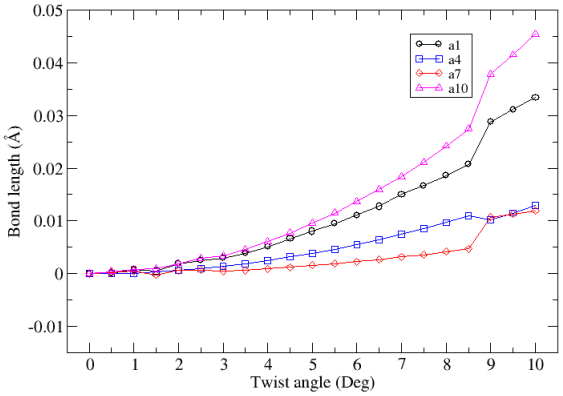

(a)

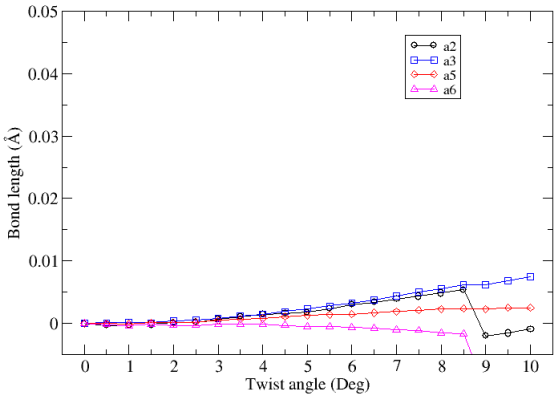

(b)

Figure 3.22: C-C bond lengths of the twisted armchair GNRs with width $N = 8$ as a function of twist angle θ.

3.4.5 Tight-binding Model

We start with the wavefunction as introduced in previous section,

$$\frac{1}{\sqrt{N_{cell}(N+1)}}\sum_{l}\sum_{n=1}^{N}\left[\sin\left(\frac{np\pi}{N+1}\right)\right](|n,l\rangle + s|n+N,l\rangle)$$

where $1 \leq p \leq N$, and $|n,l\rangle$ denotes the p_z orbital associated with nth C atom in the unit cell labeled by l in the notation of Figure 3.19. And the eigen energy at Γ can be expressed as follows:

$$E(s,p) = 2V_1[\cos(\frac{p\pi}{N+1}) + s],$$

where $s = 1$ indicates the BS and $s = -1$ indicates the AS. In this nearest-neighbor tight-binding model, the ribbon of $N = 3m + 2$ is metallic with HOMO and LUMO touching each other. We cannot distinguish the HOMO and LUMO. In this case, we introduced the third-nearest-neighbor interactions as perturbation. The perturbation shifted the energy by $-3/(N+1)V_3$ upward for LUMO and the same amount downward for HOMO. The third nearest-neighbor interactions are required to open the gap to give results consistent with our LDA results. After introducing these interactions, we determine that LUMO is at $p = (N+1)/3$ and anti-bonding, HOMO is at $2(N+1)/3$ and bonding. Because in some ribbons, the second HOMO (HOMO-1) and second LUMO (LUMO+1) are moving towards the Fermi level under twist and will play a role in determining the band gap beyond certain twist angle. We also analyzed the HOMO-1 and LUMO+1 states and present the results in Table 3.4.

Family	HOMO	LUMO	HOMO-1	LUMO+1
$N = 3m$	-$\downarrow$	+$\uparrow$	+$\uparrow$	-$\downarrow$
$N = 3m + 1$	+$\uparrow$	-$\downarrow$	-$\downarrow$	+$\uparrow$
$N = 3m + 2$	+$\uparrow$	-$\downarrow$	-$\downarrow$	+$\uparrow$

Table 3.4: Binding states of edge C p_z orbitals HOMO and LUMO. $\uparrow$ ($\downarrow$) indicates the energy point shifts upward (downward) with increasing twist angle. $+$ $(-)$ indicates the bonding (anti-bonding) states.

3.4.6 Band Gap Change Under Twist

In Figure 3.23 and Table 3.5 we present the local density functional results for the variations of energy gaps of three family structures with different widths ($N = 3m$, $3m+1$, $3m+2$, where $m = 2, 3, 4$) as a function of the twist angle θ. In combination with the tight-binding model in previous section, we will discuss in details how the twist affects the energy gaps in armchair graphene nanoribbons.

Depending on the bonding (anti-bonding) states of near Fermi level bands, the response of the armchair GNRs to the twist can be classified into two categories. One is of width $N = 3m$, and the other two belong to the second family.

For $N = 3m$, the energy gap will go through three stages with increasing twist. In the first stage, the bonding LUMO goes up and anti-bonding HOMO goes down, resulting in the raising of band gap. The HOMO-1 is raising and LUMO+1 is lowering. After certain twist angle, HOMO-1 and LUMO+1 will take over to determine the band gap. This begins the second stage, in which the band gap is reduced with increasing twist angle. When the twist is increased further, the HOMO-1 and LUMO+1 may touch and exchange bonding characteristics and then follow their previous way. This will start the third stage, in which the band gap is increased again. For $N = 12$ we only observed the first stage. For $N = 18$, we observed all these three stages because the reduced quantum confinement and bigger change in length of bonds parallel to the ribbon axis resulted from the bigger ribbon width.

For $N = 3m + 1$ and $N = 3m + 2$, the HOMO-1 and LUMO+1 are moving away from the Fermi level and will not play a role in determining the band gap. Within the twist angle studied, we only have to consider the HOMO and LUMO orbitals. Just as we have seen in armchair GNRs with width $N = 8$, the band gap will have two stages. The first stage is decreasing the band gap and the second would be increasing

the gap. In $N = 10$, we only have the first stage because of the relatively bigger band gap and not big enough ribbon width. Generally the turning point is moving toward smaller twist angle with increasing ribbon width for same family.

At each turning point corresponding to the minimum band gap, the gap closure may occur because of the additional symmetry at the zone center or edge. We can not have real band crossing because the eigen vectors of π bands belong to the same irreducible representation group.

Our bonding and anti-bonding analysis applies for other strain effect in the armchair GNRs as well. Our tight binding analysis are qualitatively consistent with the previous calculations on uniaxial strain effect on armchair GNRs by others. But the linear relation by TB model[93] or density functional theory calculations[94] is not observed in our calculations. This may be due to the hybridization between the s, p_x, p_y, p_z orbitals coming from the twist between neighboring zigzag chains.

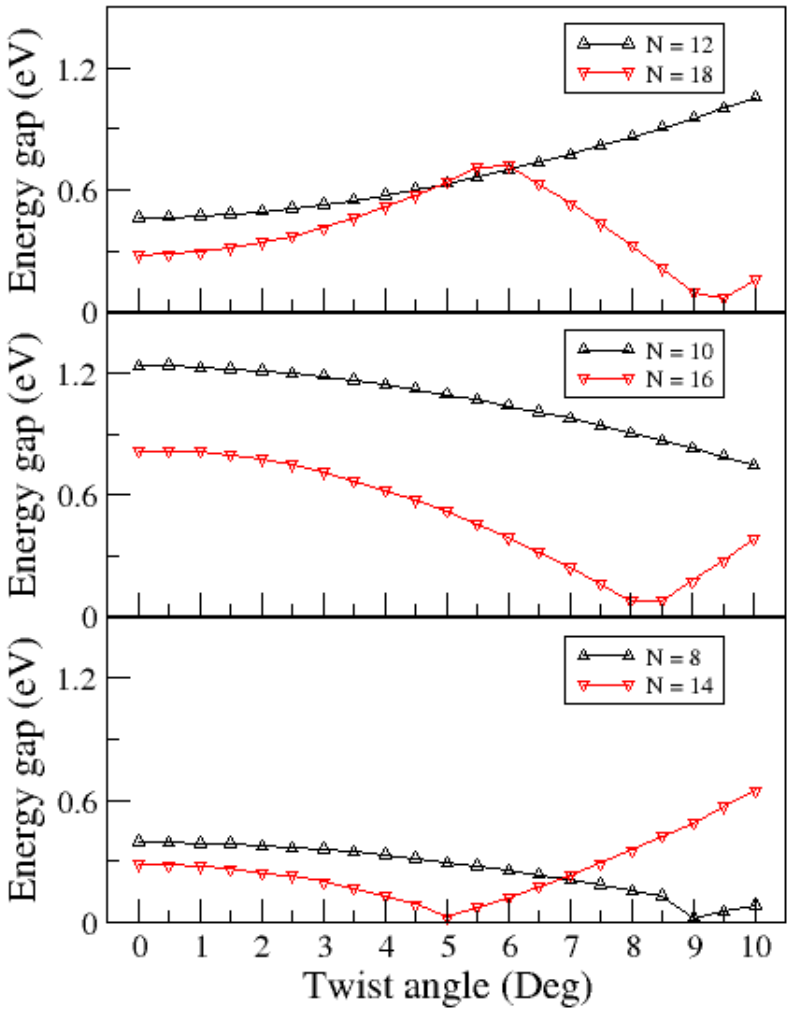

Figure 3.23: Variation of energy gaps of armchair GNRs as a function of twist angle θ. (a), (b), and (c) represent the armchair GNRs of width $N = 3m$, $3m + 1$, and $3m + 2$, respectively.

Table 3.5: Band gaps (eV) as a function of twist angle (Deg) in armchair graphene nanoribbons with various widths N

Twist angle	N=8	N=10	N=12	N=14	N=16	N=18
0.0	0.3958	1.2364	0.4648	0.2830	0.8166	0.2795
0.5	0.3904	1.2382	0.4677	0.2800	0.8170	0.2850
1.0	0.3842	1.2281	0.4732	0.2717	0.8159	0.2949
1.5	0.3860	1.2202	0.4816	0.2613	0.7983	0.3147
2.0	0.3727	1.2125	0.4951	0.2406	0.7764	0.3415
2.5	0.3632	1.1979	0.5109	0.2268	0.7486	0.3744
3.0	0.3579	1.1869	0.5276	0.1972	0.7125	0.4146
3.5	0.3456	1.1658	0.5498	0.1651	0.6714	0.4619
4.0	0.3313	1.1440	0.5738	0.1276	0.6239	0.5165
4.5	0.3116	1.1226	0.6051	0.0868	0.5839	0.5737
5.0	0.2909	1.0954	0.6329	0.0217	0.5215	0.6404
5.5	0.2739	1.0688	0.6642	0.0697	0.4568	0.7115
6.0	0.2541	1.0399	0.7004	0.1190	0.3907	0.7197
6.5	0.2309	1.0085	0.7374	0.1732	0.3200	0.6293
7.0	0.2062	0.9763	0.7749	0.2302	0.2435	0.5341
7.5	0.1821	0.9423	0.8180	0.2885	0.1625	0.4341
8.0	0.1541	0.9063	0.8610	0.3533	0.0780	0.3273
8.5	0.1274	0.8689	0.9070	0.4214	0.0761	0.2141
9.0	0.1990	0.8293	0.9532	0.4891	0.1746	0.0994
9.5	0.0505	0.7895	1.0027	0.5673	0.2764	0.0702
10.0	0.0815	0.7492	1.0560	0.6476	0.3847	0.1582

3.5 Summary and Conclusions

In this chapter we studied two kinds of GNRs: zigzag and armchair GNRs. We found that the zigzag GNRs have magnetically ordered insulating ground states that are ferromagnetically coupled along each edge and anti-ferromagnetically coupled across the edges. And the AFM band gap decreases with increasing ribbon width. The electronic states near Fermi level are localized at edge carbon sites, suggesting the edge sensitivity to passivating functional groups and therefore zigzag GNRs could be used in chemical sensor applications. Our LDF results with Gaussian basis sets agree with previous calculation by using plane wave basis, numerical atomic orbitals, and also are consistent with the tight-binding calculations on the zigzag GNRs. armchair GNRs do not have spin-polarized ground state and localized edge states. The band gaps of armchair GNRs are strongly dependent on the ribbon width. The complex alternating relation between gaps and ribbon width is different from the nearest-neighbor tight-binding prediction. The introduction of third-nearest-neighbor interaction across the hexagons resolved this discrepancy. Besides the planar GNRs, we investigated the twisted armchair GNRs and found the response to the applied torsional deformation could be classified into two categories. The tunable band gap upon applied twist is very useful in nano-mechanical devices.

It is well-known that the LDF underestimated the band gaps. Yang, *et al.*[96] presented calculations of the quasi-particle energies and band gaps of planar graphene nanoribbons carried out using a first-principles many-electron Green's function approach within the GW[97–100] approximation. The self-energy corrections are different for ribbons of different widths because of the screening effect of various magnitudes. However, the characteristics of three families in band gaps remain the same in armchair graphene nanoribbons.

CHAPTER 4

SURFACE PASSIVATION EFFECTS IN SILICON NANOWIRES

4.1 Overview

In recent years Si nanowires (SiNWs) have attracted much attention because of their potential applications in electronic, thermoelectric, and optoelectronic devices. They can be used as building blocks of nanoscale electrical devices such as field-effect transistors (FETs).[101–104] They are capable of inflating 4 times their normal size when absorbing lithium ions, which enables the new battery to hold 10 times the charge of existing lithium-ion batteries.[10] SiNWs can be used as thermoelectric materials because of their low thermal but high electrical conductivity.[12, 13] SiNWs also have potential application as solar cells to convert light into electricity. [11, 105–110]

The broad range of potential applications of SiNWs makes it critically important to understand how to tailor their electronic properties. The electronic properties of SiNWs can be modified by varying a range of structural properties such as surface passivation,[101] doping,[102] and how the nanowires are mechanically processed.[111]

Because of the enhanced surface-to-volume ratio of the SiNWs compared to bulk silicon, the surface of the SiNWs is of special status and the electronic properties of the SiNWs are strongly dependent on the characteristics of the SiNW surfaces. Cui, *et al.*[101] showed that exposure to 4-nitrophenyloctadecanoate or tetraethylammonium bromide can improve the conductance and on-off ratios in oxidized SiNW-based FETs. Haick, *et al.*[112] achieved the methyl passivation on SiNWs via a two-step chlorination/alkylation method and showed that the SiNWs have enhanced air sta-

bility and high hole mobility.

Although the question of how the dangling bonds are passivated at the silicon nanowire surface is of great importance, most of the theoretical studies have been carried out on H-terminated[99, 113–119] and bare SiNWs,[120–122] focusing on quantum confinement effects, orientation, and cross-section dependence of the electronic properties of SiNWs, doping effects, and surface reconstructions. There are very few investigations focusing on the surface effects. For examples, Blase, *et al.*[123] calculated the effects of a single alkyl chain on the zero-bias conductance of SiNWs and found that the Landauer conductance near Fermi level is almost not affected. Nolan, *et al.*,[124] using a combination of plane wave basis sets and pseudopotentials, observed that passivation with OH or NH_2 reduces the band gap of $\langle 100 \rangle$ SiNWs. Aradi, *et al.*[125] reported that the OH passivation also can induce the band gap reduction of $\langle 110 \rangle$ SiNWs. Leu, *et al.*[126] calculated the band structure of SiNWs with halogens surface substituents passivating the SiNW surfaces, and found that passivation with more weakly interacting surface species appears to lead to more marked reductions in the SiNW band gaps. The band gap reduction comes from the weakly interacting surface species which can not pull surface states of bare SiNWs out of mid-gap.

In our studies we choose the silicon nanowires along $\langle 110 \rangle$ and $\langle 100 \rangle$ as objects of study based on the experimental observation on the relations between the wire diameter and orientations. When synthesizing silicon nanowires using gold nanocluster-catalyzed 1D growth method, Wu, *et al.*,[127] found that the nanowires of diameter less than 10 nm prefer the $\langle 110 \rangle$ directions. Most bigger nanowires were $\langle 112 \rangle$- and $\langle 111 \rangle$-oriented. Schmidt, *et al.*,[128] using epitaxial vapor-liquid-solid (VLS) growth method, observed similar orientation dependence on the diameter. To my knowledge, no $\langle 100 \rangle$ SiNWs were obtained with the non-templated methods. Because only small silicon nanowires can be treated with the density functional theory, most computational simulations are focused on $\langle 110 \rangle$ SiNWs such that the calculation results

could be compared with experimental measurements. The ⟨100⟩-oriented nanowires are highly desirable since the conventional CMOS microelectronics are built on (100) silicon wafer. The ⟨100⟩ SiNWs can be used to fabricate the vertical field effect transistors on the (100) wafer. Researchers, with anodic alumina membranes template-directed growth technique, have obtained ⟨100⟩ silicon nanowires of diameter ranging from 60 nm to 200 nm.[129–131]

In this chapter we first present the first-principles study of the electronic band structures of SiNWs oriented along ⟨100⟩ and ⟨110⟩ directions with the surfaces passivated by hydrogen, hydroxyl, and methyl substituent groups. For convenience, sometimes we simply refer to the SiNWs of these three different surface passivations as H-SiNWs, OH-SiNWs, and CH_3-SiNWs, respectively. We observed the reduced band gaps with increasing wire diameter irrespective of passivating groups, manifesting the quantum confinement effects. Band gap reductions in OH-SiNWs with reference to H-SiNWs are also observed in our simulations, in agreement with others' results.[124, 125] CH_3 not only reduces the band gap but also leads to indirect band gaps for all ⟨100⟩ SiNWs studied. The passivations on surface not only can change the band gap nature and gap value, but also have effect on the effective mass of carriers in SiNWs. Our simulations suggest that passivation with CH_3 surface substituents substantially increases the electron effective mass for the ⟨100⟩ wires, while ⟨110⟩ SiNWs have small electron and hole effective masses for all three passivations studied.

The change on electronic band structures by surface passivations motivated us to study their effect on the transport conductance in SiNWs. As a preliminary study, we investigated the electron conductance of a ⟨110⟩ SiNW having a defect region with hydroxyl passivation rather than hydrogen passivation.

4.2 Computational Approaches

The Si nanowires studied herein were initially constructed from silicon in the diamond structure using the bulk lattice constant, $a = 5.43$ Å. All $\langle 100 \rangle$ nanowires were constructed with square cross-sections and $\{110\}$ faces, and all $\langle 110 \rangle$ nanowires were constructed with diamond cross-sections and $\{111\}$ faces. We carried out geometry optimization for all structures. The optimized structure for the $\langle 100 \rangle$ and $\langle 110 \rangle$ SiNWs are depicted in Figure 4.1. The $\langle 100 \rangle$ wires calculated have a 4-fold screw symmetry about the wire axis with translation $l = a/4$ and screw angle $\phi = \pi/2$, and the $\langle 110 \rangle$ wires have a 2-fold screw symmetry about the wire axis with translation $l = \sqrt{2}a/4$ and screw angle $\phi = \pi$. The different cross-sections of the $\langle 100 \rangle$ and $\langle 110 \rangle$ oriented SiNWs make a direct comparison of the radial scale of the wires somewhat arbitrary. We have chosen to define an effective nanowire diameter, d, given by the expression $d = \sqrt{a^3 N/2\pi l}$, where a is the lattice constant of bulk crystalline silicon, N is the number of Si atoms in the unit cell, and l is the length of the unit cell along the nanowire axis. This produces an effective diameter that scales as the square root of the cross-sectional area.

In the local-density functional (LDF) calculations, we evenly sampled 64 discrete points over the central Brillouin zone and used the 3-21G basis set. [132–134] Since our code takes advantage of the helical symmetry, the calculated band structures look quit different from those obtained by using other codes, such as VASP, SIESTA, GAUSSIAN, although they are essentially the same. To be able to compare with results reported by others using translational symmetry, all band structures shown in this chapter have been folded to be within the traditional translational Brillouin zone.

Although the LDF is well-known to underestimate the band gap, we are primarily

concerned with the relative change of the energy gaps here. We also carried out some testing calculations with PBE functional on the silicon nanowires of small diameter.

We numerically calculated the effective mass of charge carriers in silicon nanowires using the standard expression from solid-state theory $m^* = \hbar^2/(d^2E/dk^2)$, which is equal to $\hbar^2/(l^2d^2E/d\kappa^2)$ if we use helical symmetry, where l is the translation length along wire axis and $\hbar$ is the reduced Planck's constant.

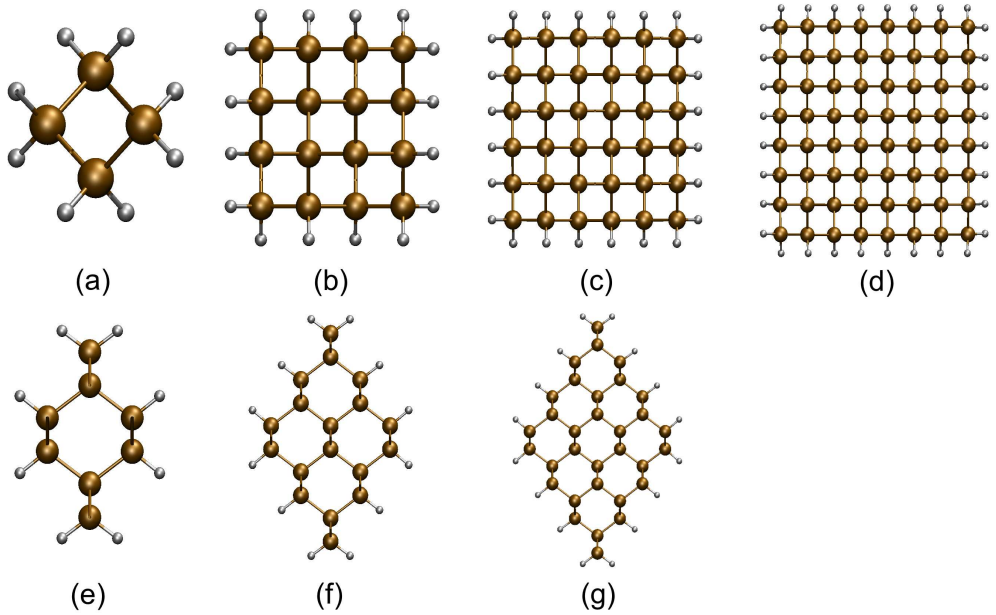

Figure 4.1: Cross-section views of the studied H-SiNWs. ⟨100⟩ SiNWs of diameter (a) 0.43 nm, (b) 0.87 nm, (c) 1.3 nm, and (d) 1.73 nm, respectively. ⟨110⟩ SiNWs of diameter (e) 0.73 nm, (f) 1.09 nm, and (g) 1.46 nm, respectively. The golden-yellow and silver balls represent Si and H atoms, respectively. In OH-SiNWs and CH_3-SiNWs, all H atoms are replaced with OH and CH_3 groups, respectively.

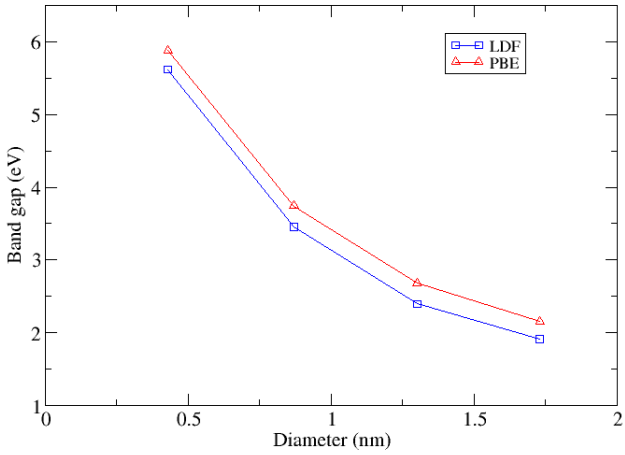

Figure 4.2: Band gaps as a function of diameter with hydrogen passivation for silicon nanowires along ⟨100⟩. The square and blue line indicate the LDF results and the uptriangle and red line indicate the PBE results.

For H-terminated ⟨100⟩ SiNWs, we compared the calculated band gaps with LDF and PBE functionals. Figure 4.2 depicts the band gaps as a function of diameter. The consideration of electron density gradient in PBE functional shifted up the LDF band gaps. The variation in the shifted amount, however, is small with maximum 0.05 eV. The LDF functional is sufficient to capture the quantum confinement in this nanomaterial and also have advantage of computional cost with comparison to PBE. The LDF was utilized for the study of silicon nanowires in the following discussions.

4.3 Structure Parameters

The surface passivating groups can affect the structure parameters of silicon nanowires. The calculated Si-Si bond lengths as a function of the distance from the bond center to the wire axis with different passivations are depicted in Figure 4.3. After geometry optimization the H-terminated ⟨100⟩ SiNWs exhibited small variations in Si-Si bond length from 2.37 Å to 2.39 Å, compared to the equilibrium value of 2.35 Å in the bulk silicon. In the OH-passivated ⟨100⟩ wire of diameter $d = 1.73$ nm, the Si-Si distances have larger variations from 2.36 Å to 2.49 Å. The Si-Si distances are ranging from 2.34 Å to 2.41 Å in the CH_3-terminated ⟨100⟩ wire of same diameter. The variations of Si-Si bond length in the core part are smaller than those near the surface.

In the ⟨110⟩ SiNWs, we found that the Si-Si bond lengths of H-SiNWs are similar to those of ⟨100⟩ H-SiNWs. The passivation with with OH or CH_3 induces smaller variations in Si-Si distances because the distances between surface-passivating groups on {111} faces of ⟨110⟩ wires are larger than those on {110} faces of ⟨100⟩ wires. The CH_3 groups even give rise to bond length variations comparable to that of the H-passivated wires along ⟨110⟩ direction.

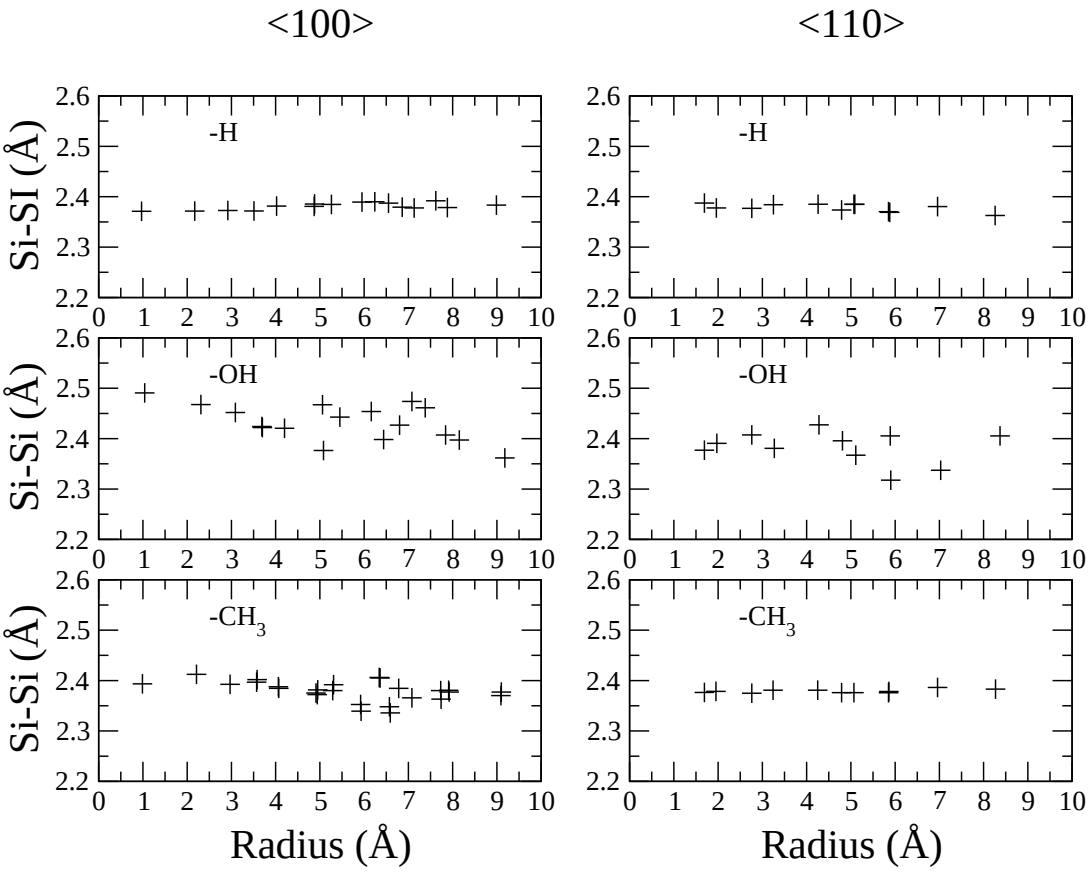

Figure 4.3: Si-Si bond length as a function of the distance from bond center to wire axis. (a), (b), (c) correspond to $\langle 100 \rangle$ SiNWs of diameter $d = 1.73$ nm passivated by H, OH, and CH_3, respectively. (d), (e), and (f) correspond to $\langle 110 \rangle$ SiNWs of diameter $d = 1.46$ nm passivated by H, OH, and CH_3, respectively.

4.4 Mulliken Population Analysis

We also did a Mulliken population analysis to see how the functional groups affect the charge distribution in the silicon nanowires. The calculated net charge of atoms as a function of the distance from atom to wire axis are presented in Figure 4.4. For elements Si, H, C, and O, the electronegativity (EN) is 1.9, 2.1, 2.5, and 3.5, respectively.[135] So C and O could pull more electrons away from the neighboring Si atoms than H and weaken the bond length of Si-Si. Although the EN of C is smaller than that of O, there are three H atoms attached to each C atom such that C atoms have more places to get charges. This results in that the charge is about -0.9 for C and is about -0.55 for O in the $\langle 100 \rangle$ wires of diameter $d = 1.73$ nm. The similar values were observed in the $\langle 110 \rangle$ wires of diameter $d = 1.46$ nm. The net charge of C and O are almost independent of the position and the wire orientation. The independence of position makes the corner Si atoms donate more charges to C or O and leave itself more positively charged because there are two groups attached to the corner Si. We found that the surface Si atoms are positive and the innermost Si atoms are nearly neutral. In the middle part, the net charge of Si atoms exhibited oscillations instead of gradual transition.

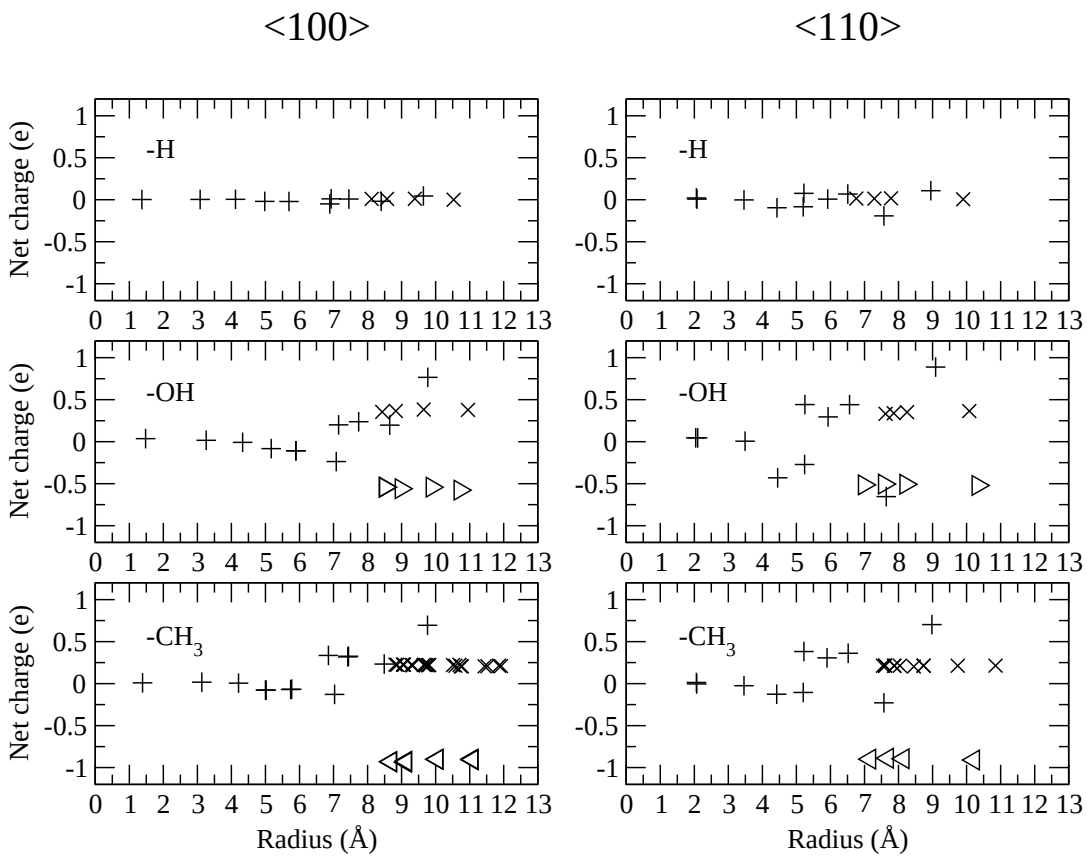

Figure 4.4: Net charge as a function of distance from the atom to the wire axis. (a), (b), (c) correspond to $\langle 100 \rangle$ SiNWs of diameter $d = 1.73$ nm passivated by H, OH, and CH_3, respectively. (d), (e), and (f) correspond to $\langle 110 \rangle$ SiNWs of diameter $d = 1.46$ nm passivated by H, OH, and CH_3, respectively. Si, H, O, and C are indicated by $+$, $\times$, $\triangleright$, and $\triangleleft$, respectively.

4.5 Band Gap Change

All of the passivations (H, OH, CH_3) studied in the present paper give indirect band gap for the $\langle 100 \rangle$ nanowire of diameter $d = 0.43$ nm. CH_3 even gives indirect band gap for all $\langle 100 \rangle$ nanowires investigated. Figure 4.5(a) shows the $\langle 100 \rangle$ Si nanowire band gaps as a function of diameter. With increasing diameter the band gap is decreasing because of the reduced quantum confinement. Because surface atoms have smaller and smaller percentage when increasing diameter from 0.43 nm to 1.73 nm, surface effect becomes weak and energy gap difference of different passivations is reduced from 2.75 eV to 0.64 eV for OH-SiNWs and from 1.72 eV to 0.54 eV for CH_3-SiNWs with H-SiNWs as the reference. We observed similar trend in band gap change of $\langle 110 \rangle$ SiNWs as shown in Figure 4.5(b). But different from the $\langle 100 \rangle$ SiNWs, the $\langle 110 \rangle$ wires have direct band gaps independent of the surface substituents. The band gap values corresponding to Figures 4.5(a) and 4.5(b) are listed in Tables 4.1 and 4.2.

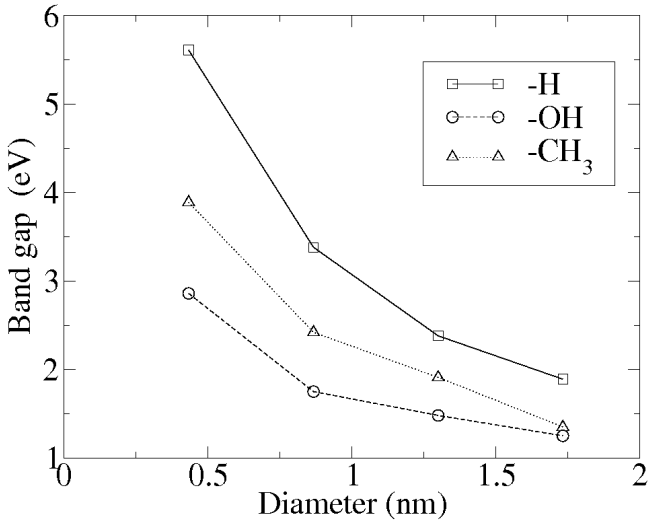

(a)

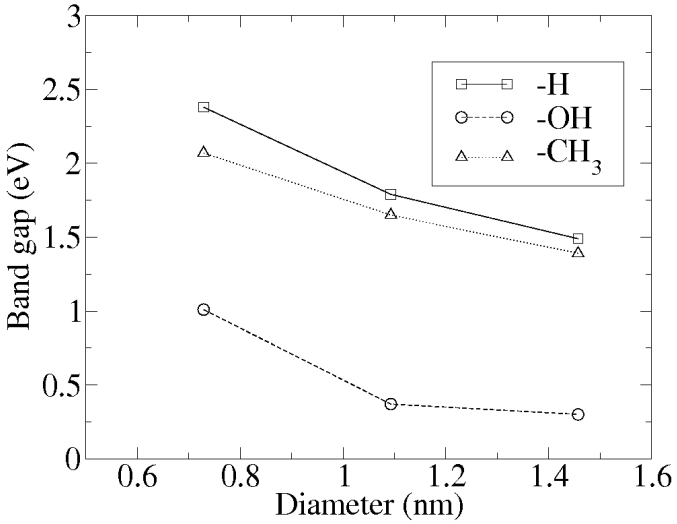

(b)

Figure 4.5: Band gaps as a function of diameter with various surface passivations for silicon nanowires along (a) ⟨100⟩, (b) ⟨110⟩.

Table 4.1: Band gaps (eV) as a function of diameter for ⟨100⟩ silicon nanowires with various passivations. X represents H, OH, or CH_3.

Stoichiometry	Diameter (nm)	H	OH	CH_3
Si_2X_2	0.43	5.61	2.86	3.89
Si_4X_4	0.87	3.38	1.75	2.42
Si_9X_6	1.30	2.38	1.48	1.91
$Si_{16}X_8$	1.73	1.89	1.25	1.35

Table 4.2: Band gaps (eV) as a function of diameter for ⟨110⟩ silicon nanowires with various passivations. X represents H, OH, or CH_3.

Stoichiometry	Diameter (nm)	H	OH	CH_3
Si_4X_4	0.73	2.38	1.01	2.07
Si_9X_6	1.09	1.79	0.37	1.65
$Si_{16}X_8$	1.46	1.49	0.30	1.39

4.6 Electronic Structures

We show the band structures of $\langle 100 \rangle$ silicon nanowires of diameter $d = 1.73$ nm with different surface passivations in Figure 4.6 and in Figure 4.7 we present the band structures of $\langle 110 \rangle$ silicon nanowires of diameter $d = 1.46$ nm. The Fermi levels in H-SiNWs are used as the reference and taken to be zero. Both OH and CH_3 change the band structure a lot and OH gives rise to more reduction of band gap. In addition to the band gap change, the Fermi levels also vary with the passivations. The CH_3 groups shift up the Fermi levels in $\langle 100 \rangle$ and $\langle 110 \rangle$ wires compared to H-SiNWs. The OH groups induce lower Fermi level in $\langle 100 \rangle$ SiNWs and higher Fermi level in $\langle 110 \rangle$ SiNWs. It is known that the Fermi levels will be aligned via charge redistribution when systems of different Fermi levels are put together. If the silicon nanowires are selectively passivated such that one segment is covered with H atoms and neighboring segment is passivated by CH_3 groups. Then the electron in CH_3-terminated part will move to H-terminated part and hole will move in the inverse way to align the Fermi levels and lower the total energy of the system. The ability of separating charge carriers in selectively passivated SiNWs could find potential application in photovoltaic devices.

Growth techniques for semiconductor nanowires have developed rapidly in recent years. Not only can the diameter and direction be controlled during growth, but nanowires can also be selectively functionalized. This has been achieved by various efforts such as electrochemical methods,[136] localized nanoscale Joule heating, [137] and adsorption and removal of self-assembled monolayers of the polymer (3-mercaptopropyl)-trimethoxysilane.[138]

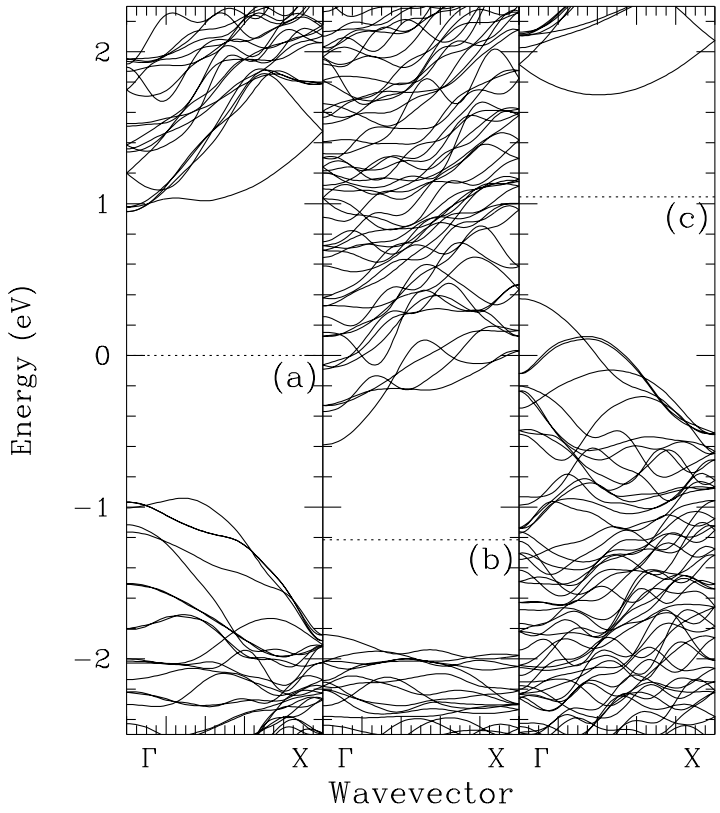

Figure 4.6: Electronic band structures of ⟨100⟩ SiNWs (diameter $d = 1.73$ nm) passivated by (a) H, (b) OH, and (c) CH_3. The Fermi level in H-SiNW is shifted to zero eV and taken as the reference.

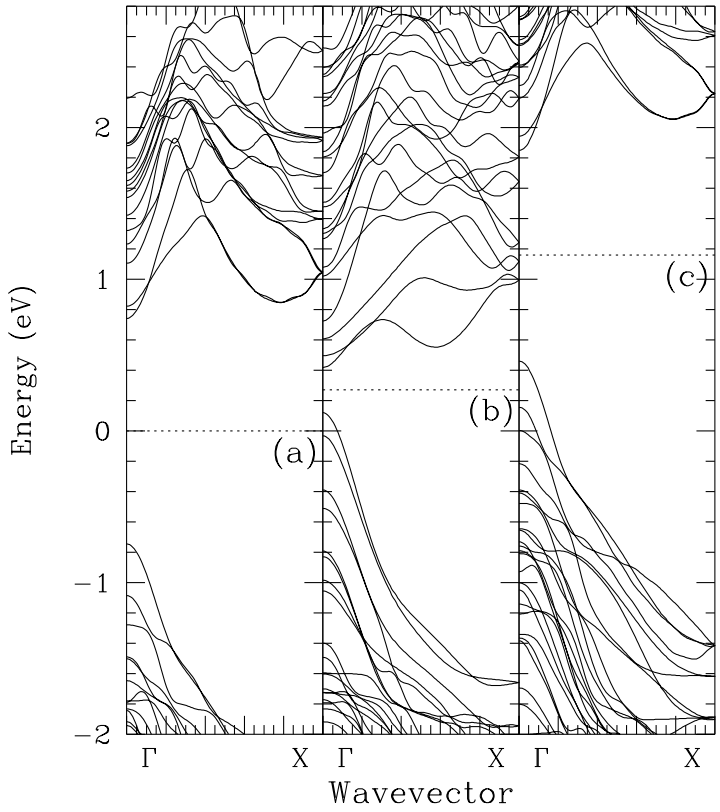

Figure 4.7: Electronic band structures of ⟨110⟩ SiNWs (diameter $d = 1.46$ nm) passivated by (a) H, (b) OH, and (c) CH_3. The Fermi level in H-SiNW is shifted to zero eV and taken as the reference.

4.7 Near-gap States

The near-gap states are mostly responsible for the transport and optical properties of the system. In order to see how the surface passivations will affect those properties in detail, we plot the orbital density of the highest occupied molecular orbital (HOMO) and lowest unoccupied molecular orbital (LUMO) for the $\langle 100 \rangle$ SiNWs of diameter $d = 1.73$ nm in Figure 4.8 and for the $\langle 110 \rangle$ SiNWs of diameter $d = 1.46$ nm in Figure 4.9 with sub-figures (a), (b), and (c) corresponding to the passivating substituents H, OH, and CH_3, respectively.

First look at the $\langle 100 \rangle$ SiNWs. For the H-SiNWs, both HOMO and LUMO are concentrated in the interior of the nanowire. Upon OH passivation HOMO goes to the corner O atoms while LUMO leaves the central region and corners blank. In the CH_3-SiNWs HOMO and LUMO spread out over the whole wire.

In the $\langle 110 \rangle$ SiNWs, the LUMO orbitals of H-SiNWs and CH_3-SiNWs have similar distribution with more contribution from the central region while the OH groups make the LUMO concentrated in a rectangular region. For the HOMO orbitals of $\langle 110 \rangle$ SiNWs, CH_3 groups make the orbitals more on the interior atoms compared to the H-SiNWs. The OH groups change it dramatically and the HOMO moves to the top and bottom Si and O atoms. And more importantly, the HOMO and LUMO have considerable concentration on O atoms in both $\langle 100 \rangle$ and $\langle 110 \rangle$ SiNWs, indicating that the OH-SiNWs are more sensitive to the external environment than the other two kinds of passivations.

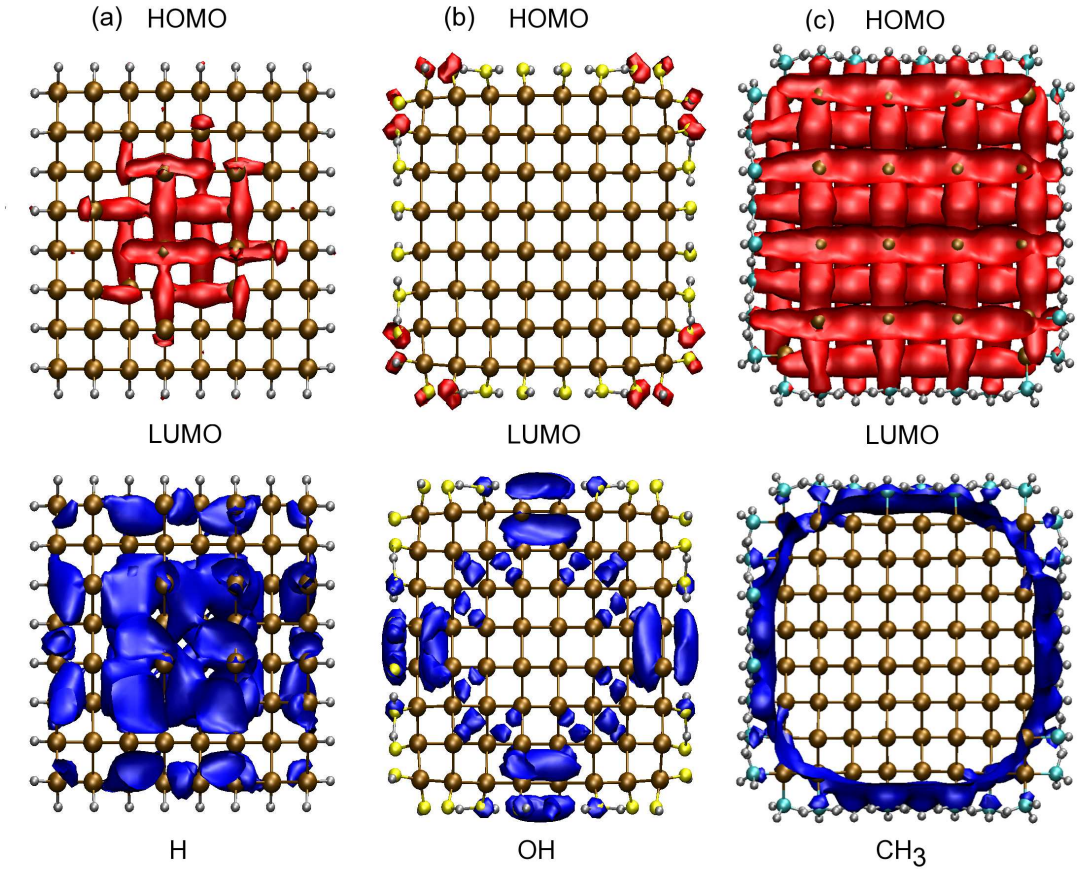

Figure 4.8: The HOMO and LUMO orbital density of the ⟨100⟩ SiNWs. (a), (b), and (c) correspond to SiNWs passivated by H, OH, and CH_3, respectively. Here red and blue represent HOMO and LUMO density, respectively. The contour is at 10% of the maximum value.

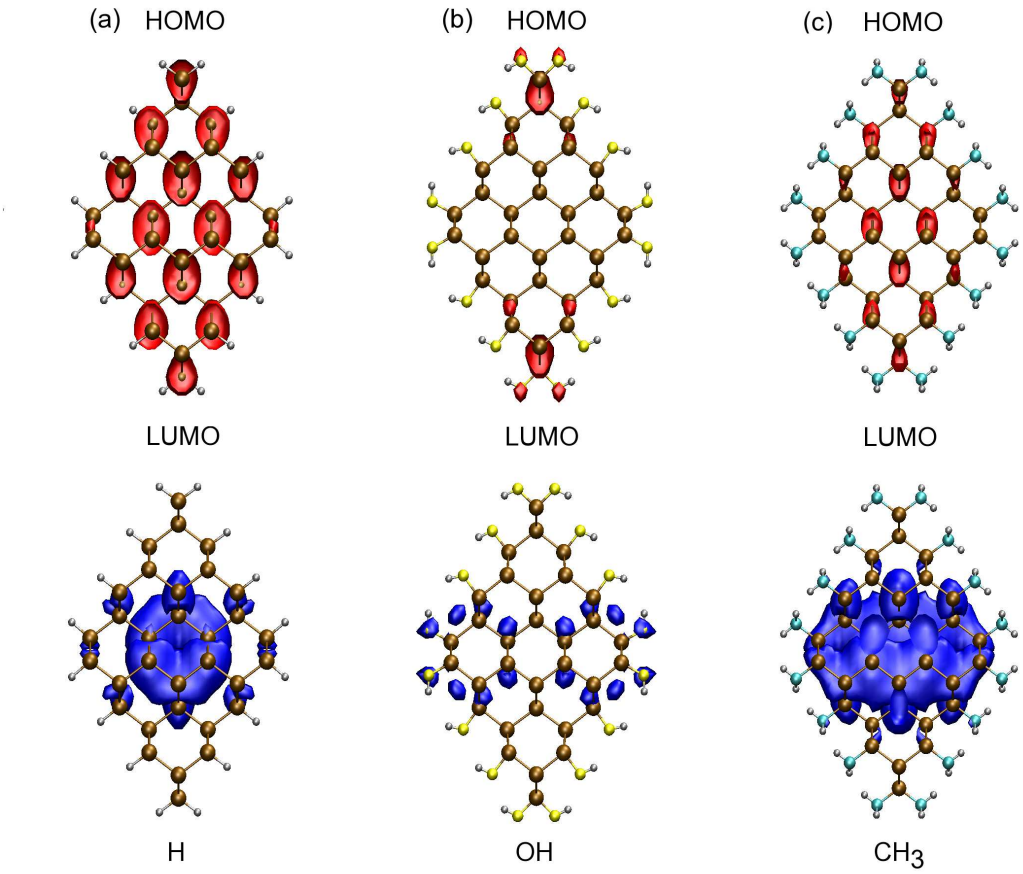

Figure 4.9: The HOMO and LUMO orbital density of the ⟨110⟩ SiNWs. (a), (b), and (c) correspond to SiNWs passivated by H, OH, and CH_3, respectively. Here red and blue represent HOMO and LUMO density, respectively. The contour is at 10% of the maximum value.

Usually the surface substituents such as hydroxyl, halogens[126, 139] and methyl in ⟨100⟩ SiNWs from our simulations will induce big change in the spatial distribution of near-gap orbitals. However, it is interesting to note that the CH_3 substituents do not have significant effect on the HOMO and LUMO orbitals in ⟨110⟩ SiNWs.

In Figures 4.10 and 4.11 we depict the isosurface of the HOMO and LUMO wave functions in ⟨110⟩ H-SiNWs, respectively. We can see that the wave functions have alternating positive and negative values along the wire axis and hence nodal surfaces perpendicular to the wire axis. When applying uniaxial tensile (compressive) strain, the energy values of the HOMO and LUMO will shift downward (upward) because the increase (decrease) of the distance between nodal planes results in the raising (lowering) of kinetic energy. So the conduction band minimum (CBM) and valence band maximum (VBM) will decrease or increase simultaneously. Similar effect was predicted to be useful in separating electrons and holes when partial strain is applied in ⟨110⟩ SiNWs.[89, 140] Under 2% tension, LUMO is located in strained region while HOMO is in the regular part in a partially strained Silicon nanorod, suggesting photovoltaic application in terms of type-II homojunction solar cells.

In our simulations, the CH_3 passivation retains the HOMO and LUMO structures of alternating positive and negative values along the wire axis as shown in Figures 4.12 and 4.13. So the ⟨110⟩ CH_3-SiNWs are supposed to have similar capability of separating the positive and negative charge carriers under partial strain as in ⟨110⟩ H-SiNWs. In addition to the charge carrier separation, the CH_3-SiNWs have better air stability and provide higher hole mobility and on-off ratio than the H-SiNWs [112] and do not affect the conductance of the near-gap channels, offering quasi-ballistic transport within several sub-bands near the SiNWs band gap. [123]

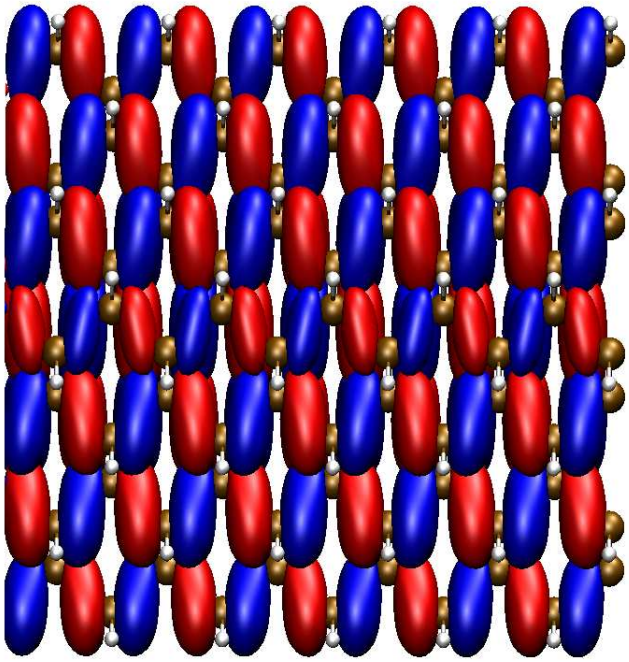

Figure 4.10: The HOMO orbital isosurface of the ⟨110⟩ H-SiNWs (diameter $d = 1.46$ nm). Here red and blue represent positive and negative values, respectively. The contour is at 10% of the maximum value.

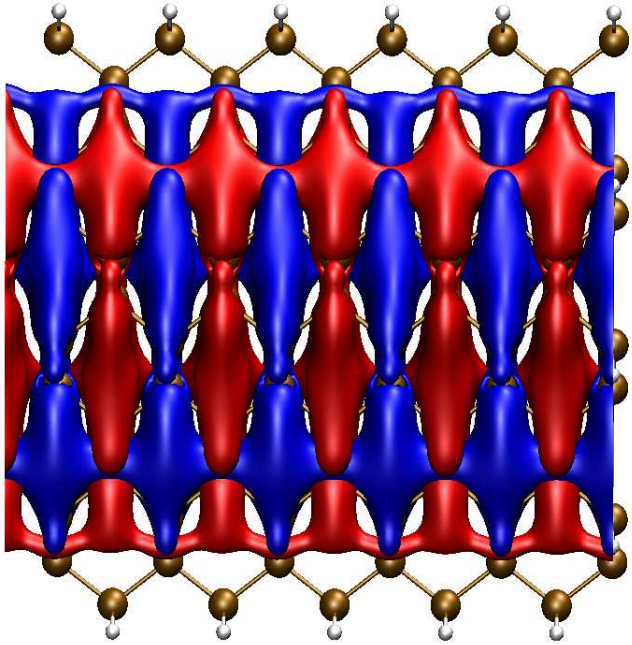

Figure 4.11: The LUMO orbital isosurface of the ⟨110⟩ H-SiNWs (diameter $d = 1.46$ nm). Here red and blue represent positive and negative values, respectively. The contour is at 10% of the maximum value.

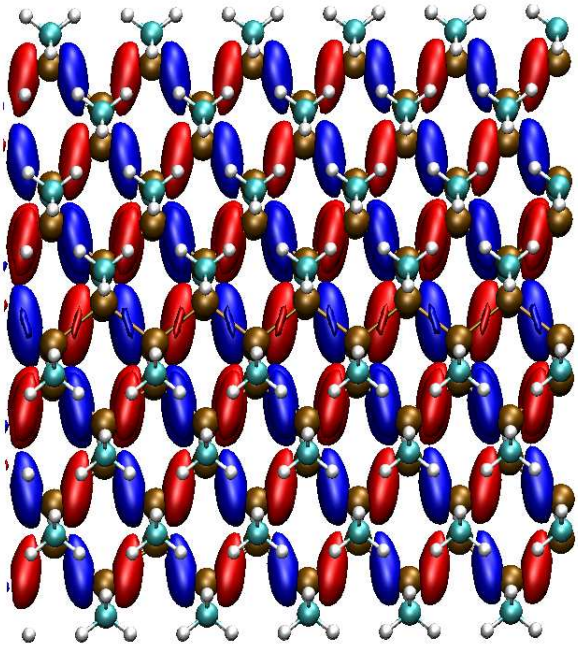

Figure 4.12: The HOMO orbital isosurface of the ⟨110⟩ CH_3-SiNWs (diameter d = 1.46 nm). Here red and blue represent positive and negative values, respectively. The contour is at 10% of the maximum value.

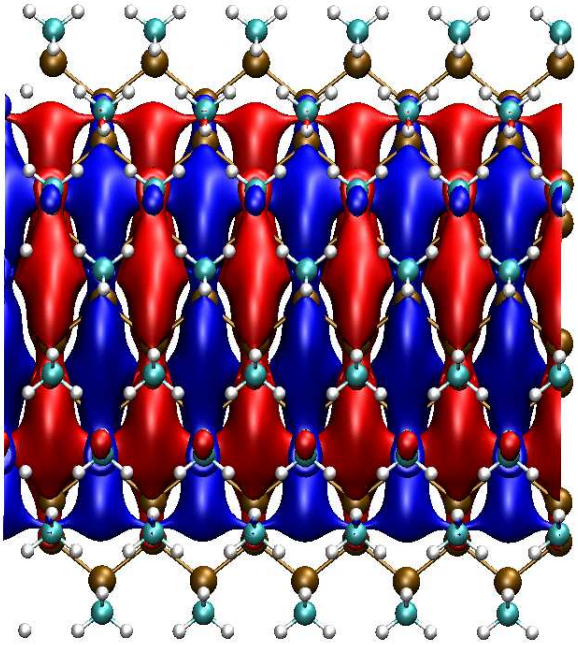

Figure 4.13: The LUMO orbital isosurface of the ⟨110⟩ CH_3-SiNWs (diameter d = 1.46 nm). Here red and blue represent positive and negative values, respectively. The contour is at 10% of the maximum value.

4.8 Effective Mass of Charge Carriers

The effective mass of carriers was calculated from the band dispersions and summarized in Table 4.3. The hole effective mass m_h of $\langle 100 \rangle$ H-SiNWs studied is decreasing with diameter in agreement with results of similar diameters reported by Yan, *et al.* [114] And in their calculations m_h is much bigger than m_e for $\langle 100 \rangle$ H-SiNWs. Although heavy hole is also observed in our simulations, the m_h is greatly reduced with increased diameter and has comparable magnitude with m_e especially for the $\langle 100 \rangle$ wire of diameter $d = 1.73$ nm. The OH passivation has effect on m_h and m_e and this effect is also dependent on the diameter in a complex manner. CH_3 passivation reduces m_h for smaller wires and increases m_h for the biggest $\langle 100 \rangle$ wire investigated. m_e is greatly increased by CH_3 passivation. With CH_3 passivation, $\langle 100 \rangle$ wires except the one of diameter $d = 0.43$ nm have m_e independent of diameter.

Light electron and hole masses were observed in our simulations for $\langle 110 \rangle$ SiNWs. The electron and hole effective masses of $\langle 110 \rangle$ H-SiNWs show comparable values, which are independent of diameter. The low-mass carriers in the $\langle 110 \rangle$ nanowire compared to those of the $\langle 100 \rangle$ nanowire are very important for electronic device materials because the carrier mobility is inversely proportional to the effective mass. Passivation with OH or CH_3 has little effect on the carrier effective masses of $\langle 110 \rangle$ SiNWs.

Table 4.3: Effective mass of silicon nanowires along ⟨100⟩ and ⟨110⟩ directions with various passivations

direction	diameter (nm)	effective mass (m_0)	H	OH	CH_3
⟨100⟩	0.43	m_e	0.56	0.39	2.51
		m_h	5.21	0.96	1.92
	0.87	m_e	0.30	0.40	1.12
		m_h	1.03	1.30	0.94
	1.30	m_e	0.22	0.29	1.13
		m_h	0.64	0.79	0.59
	1.73	m_e	0.30	0.31	1.13
		m_h	0.38	0.32	0.85
⟨110⟩	0.73	m_e	0.13	0.09	0.09
		m_h	0.13	0.11	0.13
	1.09	m_e	0.14	0.19	0.10
		m_h	0.13	0.10	0.13
	1.46	m_e	0.11	0.18	0.15
		m_h	0.12	0.18	0.14

4.9 Surface Defects Effect on Transport

4.9.1 Computational Approach

As a preliminary study on the transport in silicon nanowires, the smallest $\langle 110 \rangle$ silicon nanowires of diameter $d = 0.73$ nm was chosen as the object of study based on the consideration of computational cost. Figure 4.14 depicts our model system of transport study, which can be conceptually divided into three distinct regions: a conductor region, a left-hand lead, and a right-hand lead. The left-hand lead is a hydrogen-passivated SiNW extending infinitely to the left, and the right-hand lead is a hydrogen-passivated SiNW extending infinitely to the right. The central conductor region is functionalized with hydrogen except for one helical cell passivated by hydroxyl groups.

The Green's function of the left and right leads are calculated using an effective principal layer (PL) approach.[53, 54] It is required to set up the Hamiltonian matrices for the principal layers for the leads and also the Hamiltonian matrix for the conductor region. Each principal layer of the leads contains 7 helical cells. The conductor part contains 15 layers of helical cells, which includes 7 H-passivated helical cells on two ends and 1 helical cell passivated by OH group in the middle. The inclusion of one principal layer on both ends in the conductor makes the coupling matrices between device and leads easier to set up. Because of the usage of non-orthogonal Gaussian basis set, the overlap matrices have been set up similar to the Hamiltonian matrices.

Each transport calculation requires two HENS `parallax` SCF calculations. One is to set up the matrices of Hamiltonian and overlap for the leads. The other one is to calculate the matrices of Hamiltonian and overlap for the conductor and the interaction matrix between the leads and conductor.

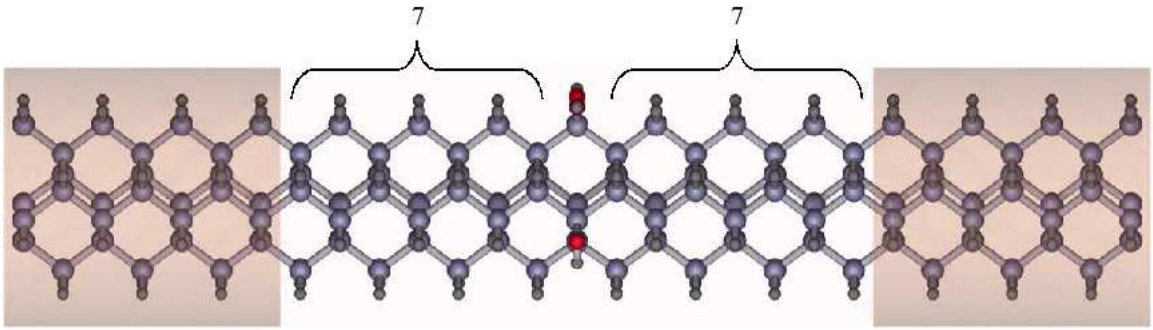

Figure 4.14: Model system for the conductance calculation. The system is composed of three regions: left-hand lead region, central conductor region, and right-hand lead region.

4.9.2 Transport Conductance

Figure 4.15 shows the results of the transport calculations. The solid line shows the calculated transport conductance in the pure H-passivated silicon nanowire while the dashed line shows the transport conductance in the model system shown in Figure 4.14 with OH passivating the surface Si atoms for one helical cell. Because of the scattering-free transport in bulk system the pure H-passivated SiNW exhibits staircase pattern with the calculated conductance $G(E)$ corresponding to integer multiples of the conductance quantum $G_0 = 2e^2/h$. The width of zero conductance region is consistent with the band gap of 2.38 eV in pure H-terminated SiNW oriented along $\langle 110 \rangle$ direction with diameter $d = 0.73$ nm. The introduction of the OH groups leads to scattering for the charge carriers from the left lead and gives rise to a significant reduction in the conductance. At energy points corresponding to the second minimum of conduction band and the second maximum of valence band, the conductance values almost drop to zero.

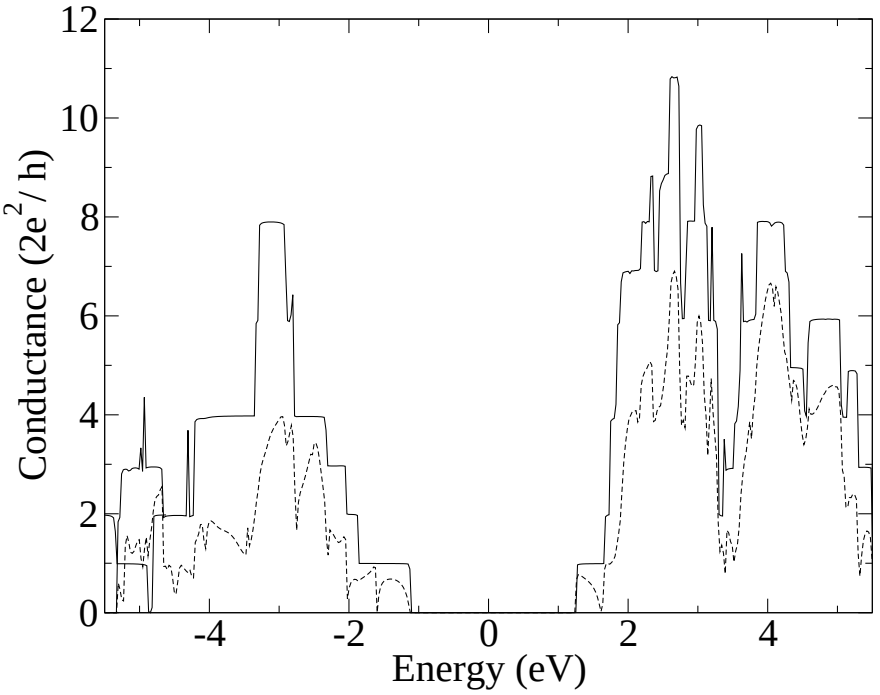

Figure 4.15: The transport conductance through the OH-passivated region: The solid line is the conductance of the pure H-SiNWs. The dashed line shows the conductance of the H-SiNWs with OH defects on one helical cell.

4.10 Summary and Conclusions

In summary, we have carried out the first-principles simulations on electronic band structures of silicon nanowires along $\langle 100 \rangle$ and $\langle 110 \rangle$ directions with surface passivated by H, OH, and CH_3. Passivation with OH groups was found to reduce the band gaps of $\langle 100 \rangle$ and $\langle 110 \rangle$ wires. Passivation with CH_3 groups gives rise to reduced indirect band gaps for $\langle 100 \rangle$ SiNWs. $\langle 110 \rangle$ SiNWs have direct band gaps independent of the diameter and surface passivation. Different from other substituents, the CH_3 groups do not have significant effect on the near-gap orbitals in $\langle 110 \rangle$ SiNWs, suggesting charge carrier separation under partial strain originally predicted for $\langle 110 \rangle$ H-SiNWs. We found that passivation with CH_3 increases the electron effective mass substantially. The $\langle 110 \rangle$ SiNWs were found to have similar electron and hole effective masses independent of the diameter and passivation.

We have carried out a preliminary study of the transport properties of a $\langle 110 \rangle$ silicon nanowire having a small defect region with hydroxyl-group passivation rather than hydrogen passivation. Using the Landauer approach, we have found that the hydroxyl defects greatly reduce the ballistic conductance of H-passivated silicon nanowires.

CHAPTER 5

CONCLUSIONS

With the rapid development of the fabrication and measurement of nanomaterials, researchers are doing various efforts to find application out of the nanostructures. So the theoretical understanding of electronic properties in nano size is of great significance both from fundamental and practical viewpoints. Utilizing the first-principles local density functional approach tailored for helical symmetry, we carried out computational simulations on graphene nanoribbon and silicon nanowires.

The study on graphene nanoribbons presented in Chapter 3 was motivated by the experimental isolation of single sheets of graphite, namely graphene. We investigated two kinds of graphene nanoribbons: zigzag and armchair nanoribbons. We found that the zigzag ribbons have magnetically ordered insulating ground states that are ferromagnetically coupled along each edge and anti-ferromagnetically coupled across the edges. And the band gap decreases with increasing ribbon width. The electronic states near Fermi level are localized at edge C sites, suggesting the edge sensitivity to passivating functional groups and therefore could be used in chemical sensor applications. Our local density functional results agree with previous calculation by using plane wave basis and also are consistent with the tight-binding predictions. Armchair ribbons do not have spin-polarized ground states or edge states. The band gaps of armchair ribbons are strongly dependent on the ribbon width. The complex alternating relation between gaps and ribbon width in our density functional calculations is different from the nearest-neighbor tight-binding prediction. The introduction of third-nearest-neighbor interactions across the hexagons resolved this puzzling differ-

ence. Besides the planar graphene nanoribbons, we investigated the twisted armchair GNRs and found the response to the applied torsional deformation could be classified into two categories according to the bonding characteristics.

In chapter 4, we mainly presented the first-principles simulation results on electronic band structure of SiNWs along ⟨100⟩ and ⟨110⟩ directions with surface passivated by H, OH, and CH_3. Passivation with OH and CH_3 groups was found to reduce the band gaps of ⟨100⟩ and ⟨110⟩ wires. The ⟨110⟩ CH_3-SiNWs and H-SiNWs have alternating positive and negative wavefunctions along the wire axis direction for HOMO and LUMO orbitals, suggesting the ability of separating charge carriers under strain. Passivation with CH_3 greatly increases the electron effective mass. Electron and hole effective masses in ⟨110⟩ SiNWs are not sensitive to the wire diameter and passivation.

We studied the pure silicon nanowires with full coverage of H, OH, and CH_3. The mixed coverage of H, OH, and CH_3 may lead to different band structures, which deserve further investigation. Nonetheless, the surface passivations are shown to be able to chemically tune the band structure and carrier mobility and provide more options together with others such as the diameter, orientation, and cross-sections when different kinds of properties of SiNWs are needed.

Besides the band structure studies on SiNWs, we have carried out a preliminary study of the transport properties of a ⟨110⟩ SiNW having a small defect region with hydroxyl-group passivation rather than hydrogen passivation. We have found that the hydroxyl defects greatly reduce the ballistic conductance of H-passivated SiNWs. It is worthwhile to carry out further studies on the transport property of SiNWs to see the conductance change by other factors such as the defect type and percentage, the wire size and orientations, etc.

BIBLIOGRAPHY

[1] K. S. Novoselov, A. K. Geim, S. V. Morozov, D. Jiang, Y. Zhang, S. V. Dubonos, I. V. Grigorieva, and A. A. Firsov. Electric field effect in atomically thin carbon films. *Science*, 306(5696):666–669, 2004.

[2] K. S. Novoselov, D. Jiang, F. Schedin, T. J. Booth, V. V. Khotkevich, S. V. Morozov, and A. K. Geim. Two-dimensional atomic crystals. *Proc. Natl. Acad. Sci. U.S.A.*, 102:10451, 2005.

[3] Y. Zhang, Y. W. Tan, H. L. Stormer, and P. Kim. Experimental observation of the quantum hall effect and berry's phase in graphene. *Nature*, 438:201, 2005.

[4] P. R. Wallace. The band theory of graphite. *Phys. Rev.*, 71(9):622–634, 1947.

[5] M. Y. Han, B. Özyilmaz, Y. Zhang, and P. Kim. Energy band-gap engineering of graphene nanoribbons. *Phys. Rev. Lett.*, 98(20):206805, 2007.

[6] J. Campos-Delgado, J. M. Romo-Herrera, X. Jia, D. A. Cullen, H. Muramatsu, Y. Ahm Kim, T. Hayashi, Z. Ren, D. J. Smith, Y. Okuno, T. Ohba, H. Kanoh, K. Kaneko, M. Endo, H. Terrones, M. S. Dresselhaus, and M. Terrones. Bulk production of a new form of sp2 carbon: Crystalline graphene nanoribbons. *Nano Lett*, 8(9):2773–2778, 2008.

[7] X. Jia, M. Hofmann, V. Meunier, B. G. Sumpter, J. Campos-Delgado, J. M. Romo-Herrera, H. Son, Y.-P. Hsieh, A. Reina, J. Kong, M. Terrones, and M. S. Dresselhaus. Controlled formation of sharp zigzag and armchair edges in graphitic nanoribbons. *Science*, 323(5922):1701–1705, 2009.

[8] D. V. Kosynkin, A. L. Higginbotham, A. Sinitskii, J. R. Lomeda, A. Dimiev, B. K. Price, and J. M. Tour. Longitudinal unzipping of carbon nanotubes to form graphene nanoribbons. *Nature*, 458:872–876, 2009.

[9] L. Jiao, L. Zhang, X. Wang, G. Diankov, and H. Dai. Narrow graphene nanoribbons from carbon nanotubes. *Nature*, 458:877–880, 2009.

[10] C. K. Chan, H. Peng, G. Liu, K. McIlwrath, X. F. Zhang, R. A. Huggins, and Y. Cui. High-performance lithium battery anodes using silicon nanowires. *Nature Nanotech.*, 3:31–35, 2008.

[11] B. Tian, X. Zheng, T. J. Kempa, Y. Fang, N. Yu, G. Yu, Huang J., and C. M. Lieber. Coaxial silicon nanowires as solar cells and nanoelectronic power sources. *Nature*, 449:885, 2007.

[12] A. I. Hochbaum, R. Chen, R. D. Delgado, W. Liang, E. C. Garnett, M. Najarian, A. Majumdar, and P. Yang. Enhanced thermoelectric performance of rough silicon nanowires. *Nature*, 451:163–167, 2008.

[13] A. I. Boukai, Y. Bunimovich, J. Tahir-Kheli, J.-K. Yu, W. A. Goddard III, and J. R. Heath. Silicon nanowires as efficient thermoelectric materials. *Nature*, 451:168, 2008.

[14] C. T. White, J. Li, D. Gunlycke, and J. W. Mintmire. Hidden one-electron interactions in carbon nanotubes revealed in graphene nanostrips. *Nano Lett.*, 7:825, 2007.

[15] D. Gunlycke, D. A. Areshkin, J. Li, J. W. Mintmire, and C. T. White. Graphene nanostrip digital memory device. *Nano Lett.*, 7:3608, 2007.

[16] D. Gunlycke, J. Li, J. W. Mintmire, and C. T. White. Altering low-bias trans-

port in zigzag-edge graphene nanostrips with edge chemistry. *Appl. Phys. Lett.*, 91:112108, 2007.

[17] J. Li and J. W. Mintmire. Electronic structure of twisted armchair graphene nanoribbons. *unpublished*.

[18] J. Li and J. W. Mintmire. Surface passivation effects in silicon nanowires. *unpublished*.

[19] J. Li, T. Jayasekera, V. Meunier, and J. W. Mintmire. Electronic transport of silicon nanowires with surface defects. *Int. J. Quan. Chem.*, 109:3705, 2009.

[20] A. Imamura. Electronic structures of polymers using the tight-binding approximation. I. polyethylene by the extended hückel method. *J. Chem. Phys.*, 52(6):3168–3175, 1970.

[21] H. Fujita and A. Imamura. Electronic structures of polymers using the tight-binding approximation. II. polyethylene and polyglycine by the cndo method. *J. Chem. Phys.*, 53(12):4555–4566, 1970.

[22] J. W. Mintmire, B. I. Dunlap, and C. T. White. Are fullerene tubules metallic? *Phys. Rev. Lett.*, 68:631, 1992.

[23] R. Landauer. *IBM J. Res. Dev.*, 1:223, 1957.

[24] S. Datta. *Electronic transport properties of mesoscopic systems*. Cambridge University Press: Cambridge, 1995.

[25] A. Szabo and N. S. Ostlund. *Modern quantum chemistry : introduction to advanced electronic structure theory*. Dover Publications, Inc., 1996.

[26] R. G. Parr and W. Yang. *Density-Functional Theory of Atoms and Molecules*. Oxford University Press: New York, 1995.

[27] R. A. Evarestov. *Quantum chemistry of solids : the LCAO first principles treatment of crystals*. Springer, 2007.

[28] L. H. Thomas. The calculation of atomic fields. *Proc. Cambridge Phil. Soc.*, 23:542–548, 1927.

[29] E. Fermi. Un metodo statistico per la determinatione di alcune priorieta dellátome. *Rend. Accad. Naz. Lincei*, 6:602–607, 1927.

[30] P. A. M. Dirac. Note on exchange phenomena in the thomas atom. *Math. Proc. Cambridge Phil. Soc.*, 26(03):376–385, 1930.

[31] E. Wigner. On the interaction of electrons in metals. *Phys. Rev.*, 46(11):1002–1011, 1934.

[32] P. Hohenberg and W. Kohn. Inhomogeneous electron gas. *Phys. Rev. B*, 136:B864, 1964.

[33] W. Kohn and L. J. Sham. Self-consistent equations including exchange and correlations effects. *Phys. Rev.*, 140:A1133, 1965.

[34] J. P. Perdew, A. Ruzsinszky, J. Tao, V. N. Staroverov, G. E. Scuseria, and G. I. Csonka. Prescription for the design and selection of density functional approximations: More constraint satisfaction with fewer fits. *J. Chem. Phys.*, 123(6):062201, 2005.

[35] J. C. Slater. A simplification of the Hartree-Fock method. *Phys. Rev.*, 81(3):385–390, 1951.

[36] J. P. Perdew and A. Zunger. Self-interaction correction to density-functional approximations for many-electron systems. *Phys. Rev. B*, 23(10):5048–5079, 1981.

[37] D. M. Ceperley and B. J. Alder. Ground state of the electron gas by a stochastic method. *Phys. Rev. Lett.*, 45(7):566–569, 1980.

[38] J. P. Perdew, K. Burke, and M. Ernzerhof. Generalized gradient approximation made simple. *Phys. Rev. Lett.*, 77(18):3865–3868, 1996.

[39] J. P. Perdew. Accurate density functional for the energy: Real-space cutoff of the gradient expansion for the exchange hole. *Phys. Rev. Lett.*, 55(16):1665–1668, 1985.

[40] J. P. Perdew and W. Yue. Accurate and simple density functional for the electronic exchange energy: generalized gradient approximation. *Phys. Rev. B*, 33(12):8800–8802, 1986.

[41] J. Tao, J. P. Perdew, V. N. Staroverov, and G. E.Scuseria. Climbing the density functional ladder: nonempirical meta-generalized gradient approximation designed for molecules and solids. *Phys. Rev. Lett.*, 91:146401, 2003.

[42] M. Levy and J. P. Perdew. Hellmann-feynman, virial, and scaling requisites for the exact universal density functionals. shape of the correlation potential and diamagnetic susceptibility for atoms. *Phys. Rev. A*, 32(4):2010–2021, 1985.

[43] G. L. Oliver and J. P. Perdew. Spin-density gradient expansion for the kinetic energy. *Phys. Rev. A*, 20(2):397–403, 1979.

[44] J. M. Shi, F. M. Peeters, G. Q. Hai, and J. T. Devreese. Donor transition energy in gaas superlattices in a magnetic field along the growth axis. *Phys. Rev. B*, 44(11):5692–5702, 1991.

[45] A. D. Becke. Density-functional thermochemistry. I. the effect of the exchange-only gradient correction. *J. Chem. Phys.*, 96(3):2155–2160, 1992.

[46] B. Hammer and M. Scheffler. Local chemical reactivity of a metal alloy surface. *Phys. Rev. Lett.*, 74(17):3487–3490, 1995.

[47] P. H. T. Philipsen, G. te Velde, and E. J. Baerends. The effect of density-gradient corrections for a molecule-surface potential energy surface. slab calculations on Cu(100)C(2x2)-CO. *Chem. Phys. Lett.*, 226(5-6):583 – 588, 1994.

[48] S. F. Boys. Electronic Wave Functions. I. A General Method of Calculation for the Stationary States of Any Molecular System. *Proc. R. Soc. A*, 200(1063):542–554, 1950.

[49] F. B. van Duijneveldt. *IBM Research Report RJ 945*. 1971.

[50] J. W. Mintmire. *Helical NanoStructure (HENS) Reference Manual*.

[51] M. B. Nardelli. Electronic transport in extended systems: application to carbon nanotubes. *Phys. Rev. B*, 60(11):7828–7833, 1999.

[52] M. B. Nardelli, J.-L. Fattebert, and J. Bernholc. $O(N)$ real-space method for ab initio quantum transport calculations: application to carbon nanotube–metal contacts. *Phys. Rev. B*, 64(24):245423, 2001.

[53] M. P. Lopez-Sancho, J. M. Lopez-Sancho, and J. Rubio. Quick iterative scheme for the calculation of transfer matrices: application to Mo (100). *J. Phys. F : Met. Phys.*, 14:1205–1215, 1984.

[54] M. P. Lopez-Sancho, J. M. Lopez-Sancho J. M. L. Sancho, and J. Rubio. Highly convergent schemes for the calculation of bulk and surface green functions. *J. Phys. F : Met. Phys.*, 15:851–858, 1985.

[55] K. S. Novoselov, A. K. Geim, S. V. Morozov, D. Jiang, M. I. Katsnelson, I. V. Grigorieva, S. V. Dubonos, and A. A. Firsov. Two-dimensional gas of massless dirac fermions in graphene. *Nature*, 438:197–200, 2005.

[56] Y.-M. Lin, K. A. Jenkins, A. Valdes-Garcia, J. P. Small, D. B. Farmer, and P. Avouris. Operation of graphene transistors at gigahertz frequencies. *Nano Lett*, 9:422–426, 2009.

[57] M. Fujita, K. Wakabayashi, K. Nakada, and K. Kusakabe. Peculiar localized state at zigzag graphite edge. *J. Phys. Soc. Jpn.*, 65(7):1920–1923, 1996.

[58] K. Nakada, M. Fujita, G. Dresselhaus, and M. S. Dresselhaus. Edge state in graphene ribbons: Nanometer size effect and edge shape dependence. *Phys. Rev. B*, 54(24):17954–17961, 1996.

[59] K. Wakabayashi, M. Fujita, H. Ajiki, and M. Sigrist. Electronic and magnetic properties of nanographite ribbons. *Phys. Rev. B*, 59(12):8271–8282, 1999.

[60] Y. Miyamoto, K. Nakada, and M. Fujita. First-principles study of edge states of H-terminated graphite ribbons. *Phys. Rev. B*, 59:9858, 1999.

[61] T. Kawai, Y. Miyamoto, O. Sugino, and Y. Koga. Graphitic ribbons without hydrogen-termination: electronic structures and stabilities. *Phys. Rev. B*, 62(24):R16349–R16352, 2000.

[62] K. V. Bets and B. I. Yakobson. Spontaneous twist and intrinsic instabilities of pristine graphene nanoribbons. *Nano Res.*, 2:161, 2009.

[63] O. Hod and G. E. Scuseria. Electromechanical properties of suspended graphene nanoribbons. *Nano Lett.*, 9(7):2619–2622, 2009.

[64] Y.-W. Son, M. L. Cohen, and S. G. Louie. Half-metallic graphene nanoribbons. *Nature*, 444:347–349, 2006.

[65] K. Nakada, M. Fujita, G. Dresselhaus, and M. S. Dresselhaus. Edge state in graphite ribbons: nanometer size effect and edge shape dependence. *Phys. Rev. B*, 54:17954, 1996.

[66] G. Lee and K. Cho. Electronic structures of zigzag graphene nanoribbons with edge hydrogenation and oxidation. *Phys. Rev. B*, 79(16):165440, 2009.

[67] K. N. Kudin. Zigzag graphene nanoribbons with saturated edges. *ACS Nano*, 2(3):516–522, 2008.

[68] O. Hod, V. Barone, J. E. Peralta, and G. E. Scuseria. Enhanced half-metallicity in edge-oxidized zigzag graphene nanoribbons. *Nano Lett.*, 7(8):2295–2299, 2007.

[69] Z. Li, J. Yang, and J. G. Hou. Half-metallicity in edge-modified zigzag graphene nanoribbons. *J. Am. Chem. Soc.*, 130(13):4224–4225, 2008.

[70] N. Hamada, S.-I. Sawada, and A. Oshiyama. New one-dimensional conductors: graphitic microtubules. *Phys. Rev. Lett.*, 68:1579, 1992.

[71] R. Saito, M. Fujita, G. Dresselhaus, and M. S. Dresselhaus. Electronic structure of chiral graphene tubules. *Appl. Phys. Lett.*, 60:2204, 1992.

[72] C. T. White, D. H. Robertson, and J. W. Mintmire. Helical and rotational symmetries of nanoscale graphitic tubules. *Phys. Rev. B*, 47:5485, 1993.

[73] J. W. Mintmire, D. H. Robertson, and C. T. White. Properties of fullerene nanotubules. *J. Phys. Chem. Solids*, 54:1835, 1993.

[74] J. W. Mintmire and C. T. White. Electronic and structural properties of carbon nanotubes. *Carbon*, 33:893, 1995.

[75] J. W. G. Wilder, L. C. Venema, A. G. Rinzler, R. E. Smalley, and C. Dekker. Electronic structure of atomically resolved carbon nanotubes. *Nature*, 391:59, 1998.

[76] T. W. Odom, J.-L. Huang, P. Kim, and C. M. Lieber. Atomic structure and electronic properties of single-walled carbon nanotubes. *Nature*, 391:62, 1998.

[77] J. W. Mintmire and C. T. White. Universal density of states for carbon nanotubes. *Phys. Rev. Lett.*, 81:2506, 1998.

[78] C. T. White and J. W. Mintmire. Density of states reflects diameter in nanotubes. *Nature*, 394:29, 1998.

[79] J. W. Mintmire and C. T. White. First-principles band structures of armchair nanotubes. *Appl. Phys. A*, 67:65, 1998.

[80] X.-P Tang, A. Kleinhammes, H. Shimoda, L. Fleming, K. Y. Bennoune, S. Sinha, C. Bower, O. Zhou, and Y. Wu. Electronic structures of single-walled carbon nanotubes determined by NMR. *Science*, 288:492, 2000.

[81] S. G. Lemay, J. W. Janssen, M. van den Hout, M. Mooij, M. J. Bronikowski, P. A. Willis, R. E. Smalley, L. P. Kouwenhoven, and C. Dekker. Two-dimensional imaging of electronic wavefunctions in carbon nanotubes. *Nature*, 412:617, 2001.

[82] M. Ouyang, J.-L. Huang, and C. M. Lieber. One-dimensional energy dispersion of single-walled carbon nanotubes by resonant electron scattering. *Phys. Rev. Lett.*, 88:066804, 2002.

[83] C. T. White and J. W. Mintmire. Fundamental properties of single-wall carbon nanotubes. *J. Phys. Chem. B*, 109:52, 2005.

[84] Y.-W. Son, M. L. Cohen, and S. G. Louie. Energy gap in graphene nanoribbons. *Phys. Rev. Lett.*, 97:216803, 2006.

[85] D. Gunlycke and C. T. White. Tight-binding energy dispersions of armchair-edge graphene nanostrips. *Phys. Rev. B*, 77:115116, 2008.

[86] X. Li, X. Wang, L. Zhang, S. Lee, and H. Dai. Chemically derived, ultrasmooth graphene nanoribbon semiconductors. *Science*, 319:1229, 2008.

[87] X. Wang, Y. Oyang, X. Li, H. Wang, J. Gui, and H. Dai. Room-temperature all-semiconducting sub-10-nm graphene nanoribbon field-effect transistors. *Phys. Rev. Lett.*, 100:206803, 2008.

[88] M. Ieong, B. Doris, J. Kedzierski, K. Rim, and M. Yang. Silicon device scaling to the sub-10-nm regime. *Science*, 306(5704):2057–2060, 2004.

[89] K.-H. Hong, J. Kim, S.-H. Lee, and J. W. Shin. Strain-driven electroni band structure modulation of si nanowires. *Nano Lett.*, 8(5):1335–1340, 2008.

[90] P. W. Leu, A. Svizhenko, and K. Cho. Ab initio calculations of the mechanical and electronic properties of strained si nanowires. *Phys. Rev. B*, 77(23):235305, 2008.

[91] Z. H. Ni, T. Yuand Y. H. Lu, Y. Y. Wang, Y. P. Feng, and Z. X. Shen. Uniaxial strain on graphene: Raman spectroscopy study and band-gap opening. *ACS Nano*, 2(11):2301–2305, 2008.

[92] M. L. Teague, A. P. Lai, J. Velasco, C. R. Hughes, A. D. Beyer, M. W. Bochrath, C. N. Lau, and N.-C. Yeh. Evidence for strain-induced local conductance modulations in single-layer graphene on SiO_2. *Nano Lett.*, 9(7):2542–2546, 2009.

[93] Y. Lu and J. Guo. Band gap of strained graphene nanoribbons. *http://arxiv.org/abs/0912.2702*, 2009.

[94] L. Sun, Q. Li, H. Ren, H. Su, Q. W. Shi, and J. Yang. Strain effect on electronic structures of graphene nanoribbons: A first-principles study. *J. Chem. Phys.*, 129(7):074704, 2008.

[95] W. J. Hehre, R. Ditchfield, and J. A. Pople. Selfconsistent molecular orbital methods. XII. further extensions of gaussiantype basis sets for use in molecular orbital studies of organic molecules. *J. Chem. Phys.*, 56:2257, 1972.

[96] L. Yang, C.-H. Park, Y.-W. Son, M. L. Cohen, and S. G. Louie. Quasiparticle energies and band gaps in graphene nanoribbons. *Phys. Rev. Lett.*, 99(18):186801, 2007.

[97] M. S. Hybertsen and S. G. Louie. Electron correlation in semiconductors and insulators: band gaps and quasiparticle energies. *Phys. Rev. B*, 34(8):5390–5413, 1986.

[98] L. Wirtz, A. Marini, and A. Rubio. Excitons in boron nitride nanotubes: Dimensionality effects. *Phys. Rev. Lett.*, 96(12):126104, 2006.

[99] X. Zhao, C. M. Wei, L. Yang, and M. Y. Chou. Quantum confinement and electronic properties of silicon nanowires. *Phys. Rev. Lett.*, 92:236805, 2004.

[100] C. D. Spataru, S. Ismail-Beigi, L. X. Benedict, and S. G. Louie. Excitonic effects and optical spectra of single-walled carbon nanotubes. *Phys. Rev. Lett.*, 92(7):077402, 2004.

[101] Y. Cui, Z. Zhong, D. Wang, W. Wang, and C. M. Lieber. High performance silicon nanowire field effect transistors. *Nano Lett.*, 3:149, 2003.

[102] Y. Cui, X. Duan, J. Hu, and C. M. Lieber. Doping and electrical transport in silicon nanowires. *J. Phys. Chem. B*, 104:5213, 2000.

[103] J. Goldberger, A. I. Hochbaum, R. Fan, and P. Yang. Silicon vertically integrated nanowire field effect transistors. *Nano Lett.*, 6:973, 2006.

[104] V. Schmidt, H. Riel, S. Senz, S. Karg, W. Riess, and U. Gösele. Realization of a silicon nanowire vertical surround-gate field-effect transistor. *Small*, 2:85, 2006.

[105] M. D. Kelzenberg, D. B. Turner-Evans, B. M. Kayes, M. A. Filler, M. C. Putnam, N. S. Lewis, and H. A. Atwater. Photovoltaic measurements in single-nanowire silicon solar cells. *Nano Lett.*, 8:710, 2008.

[106] K. Peng, Y. Xu, Y. Wu, Y. Yan, S.-T. Lee, and J. Zhu. Aligned single-crystalline Si nanowire arrays for photovoltaic applications. *Small*, 1:1062, 2005.

[107] H. Fang, X. Li, S. Song, Y. Xu, and J. Zhu. Fabrication of slantingly-aligned silicon nanowire arrays for solar cell applications. *Nanotechnology*, 19:255703, 2008.

[108] L. Tsakalakos, J. Balch, J. Fronheiser, B. A. Korevaar, O. Sulima, and J. Rand. Silicon nanowire solar cells. *Appl. Phys. Lett.*, 91:233117, 2007.

[109] B. M. Kayes, H. A. Atwater, and N. S. Lewis. Comparison of the device physics principles of planar and radial p-n junction nanorod solar cells. *J. Appl. Phys.*, 97:114302, 2005.

[110] C. H. Peters, A. R. Guichard, A. C. Hryciw, M. L. Brongersma, and M. D. McGehee. Energy transfer in nanowire solar cells with photo-harvesting shells. *J. App. Phys.*, 105:124509, 2009.

[111] A. J. Lu, R. Q. Zhang, and S. T. Lee. Stress-induced band gap tuning in <112> silicon nanowires. *Appl. Phys. Lett.*, 91:263107, 2007.

[112] H. Haick, P. T. Hurley, A. I. Hochbaum, P. Yang, and N. S. Lewis. Electrical characteristics and chemical stability of non-oxidized methyl-terminated silicon nanowires. *J. Am. Chem. Soc.*, 128:8990, 2006.

[113] A. J. Read, R. J. Needs, K. J. Nash, L. T. Canham, P. D. J. Calcott, and A. Qteish. First-principles calculations of the electronic properties of silicon quantum wires. *Phys. Rev. Lett.*, 69:1232, 1992.

[114] J.-A. Yan, L. Yang, and M. Y. Chou. Size and orientation dependence in the electronic properties of silicon nanowires. *Phys. Rev. B*, 76:115319, 2007.

[115] R. Q. Zhang, Y. Lifshitz, D. D. D. Ma, Y. L. Zhao, Th. Frauenheim, S. T. Lee, and S. Y. Tong. Structures and energetics of hydrogen-terminated silicon nanowire surfaces. *J. Chem. Phys.*, 123:144703, 2005.

[116] T. Vo, A. J. Williamson, and G. Galli. First principles simulations of the structural and electronic properties of silicon nanowires. *Phys. Rev. B*, 74:045116, 2006.

[117] P. B. Sorokin, P. V. Avramov, A. G. Kvashnin, D. G. Kvashnin, S. G. Ovchinnikov, and A. S. Fedorov. Density functional study of <110>-oriented thin silicon nanowires. *Phys. Rev. B*, 77:235417, 2008.

[118] C. R. Leao, A. Fazzio, and A. J. R. da Silva. Confinement and surface effects in B and P doping of silicon nanowires. *Nano Lett.*, 8:1866, 2008.

[119] A. K. Singh, V. Kumar, R. Note, and Y. Kawazoe. Effects of morphology and doping on the electronic and structural properties of hydrogenated silicon nanowires. *Nano Lett.*, 6:920, 2006.

[120] J. X. Cao, X. G. Gong, J. X. Zhong, and R. Q. Wu. Sharp corners in the cross section of ultrathin Si nanowires. *Phys. Rev. Lett.*, 97:136105, 2006.

[121] R. Rurali and N. Lorente. Metallic and semimetallic silicon <100> nanowires. *Phys. Rev. Lett.*, 94:026805, 2005.

[122] R. Rurali, A. Poissier, and N. Lorente. Size effects in surface-reconstructed <100> and <110> silicon nanowires. *Phys. Rev. B*, 74:165324, 2006.

[123] X. Blase and M.-V. Fernández-Serra. Preserved conductance in covalently functionalized silicon nanowires. *Phys. Rev. Lett.*, 100:046802, 2008.

[124] M. Nolan, S. O'Callaghan, G. Fagas, J. C. Greer, and Th. Frauenheim. Silicon nanowire band gap modification. *Nano Lett.*, 7:34, 2007.

[125] B. Aradi, L. E. Ramos, P. Deák, Th. Köhler, F. Bechstedt, R. Q. Zhang, and Th. Frauenheim. Theoretical study of the chemical gap tuning in silicon nanowires. *Phys. Rev. B*, 76:035305, 2007.

[126] P. W. Leu, B. Shan, and K. Cho. Surface chemical control of the electronic structure of silicon nanowires: density functional calculations. *Phys. Rev. B*, 73:195320, 2006.

[127] Y. Wu, Y. Cui, L. Huynh, C. J. Barrelet, D. C. Bell, and C. M. Lieber. Controlled growth and structures of molecular-scale silicon nanowires. *Nano Lett.*, 4:433, 2004.

[128] V. Schmidt, S. Senz, and U. Gösele. Diameter-dependent growth direction of epitaxial silicon nanowires. *Nano Lett.*, 5:931, 2005.

[129] K.-K. Lew, C. Reuther, A. H. Carim, J. M. Redwing, and B. R. Martin. Template-directed vapor-liquid-solid growth of silicon nanowires. *J. Vac. Sci. Technol. B*, 20:389, 2002.

[130] T. Shimizu, S. Senz, S. Shingubara, and U. Gösele. Synthesis of epitaxial Si(100) nanowires on Si(100) substrate using vapor-liquid-solid growth in anodic aluminum oxide nanopore arrays. *Appl. Phys. A*, 87:607, 2007.

[131] T. Shimizu, T. Xie, J. Nishikawa, S. Shingubara, S. Senz, and U. Gösele. Synthesis of vertical high-density epitaxial Si(100) nanowire arrays on a Si(100) substrate using an anodic aluminum oxide template. *Adv. Mater.*, 19:917, 2007.

[132] J. S. Binkley, J. A. Pople, and W. J. Hehre. Self-consistent molecular orbital

methods. 21. small split-valence basis sets for first-row elements. *J. Am. Chem. Soc.*, 102:939–947, 1980.

[133] M. S. Gordon, J. S. Binkley, J. A. Pople, W. J. Pietro, and W. J. Hehre. Self-consistent molecular orbital methods. 22. small split-valence basis sets for second-row elements. *J. Am. Chem. Soc.*, 104:2797–2803, 1982.

[134] P. C. Hariharan and J. A. Pople. The influence of polarization functions on molecular orbital hydrogenation energies. *Theo. Chem. Acc.*, 28:213–222, 1973.

[135] L. Pauling. *The Nature of the Chemical Bond and the Structure of Molecules and Crystals: An Introduction to Modern Structural Chemistry*. Cornell University Press, Ithaca New York, 1960.

[136] Y. L. Bunimovich, G. Ge, K. C. Beverly, R. S. Ries, L. Hood, and J. R. Heath. Electrochemically progammed, spatially selective biofunctionalization of silicon wires. *Langmuir*, 20:10630 – 10638, 2004.

[137] I. Park, Z. Li, A. P. Pisano, and R. S. Williams. Selective surface functionalization of silicon nanowores via nanoscale joule heating. *Nano Lett.*, 7:3106, 2007.

[138] K. Skinner, C. Dwyer, and S. Washburn. Selective functionalization of arbitrary nanowires. *Nano Lett.*, 6:2758, 2006.

[139] M. F. Ng, L. Zhou, S. W. Yang, L. Y. Sim, V. B. C. Tan, and P. Wu. Theoretical investigation of silicon nanowires:methodology, geometry, surface modification, and electrical conductivity using a multiscale approach. *Phys. Rev. B*, 76:155435, 2007.

[140] Z. Wu, J. B. Neaton, and J. C. Grossman. Charge separation via strain in silicon nanowires. *Nano Lett.*, 9:2418, 2009.

VITA

JUNWEN LI

Candidate for the Degree of

Doctor of Philosophy

Dissertation: FIRST-PRINCIPLES STUDY OF ELECTRONIC PROPERTIES OF ONE DIMENSIONAL NANOSTRUCTURES

Major Field: Physics

Biographical:

Personal Data: Born in Dongying, Shandong, China on October 6th, 1977.

Education: Received Bachelor of Science degree in Applied Physics from Qingdao University, Qingdao, Shandong, China in July 1999. Received Master of Science degree in Physics from Institute of Physics, Chinese Academy of Sciences, Beijing, China in July 2002. Completed the requirements for the degree of Doctor of Philosophy with a major in Physics at Oklahoma State University in May 2010.

Experience: Employed by Institute of Physics, Chinese Academy of Sciences as an electrical engineer from August 2002 to August 2005. Employed by Department of Physics, Oklahoma State University as graduate teaching assistant and research assistant from August 2005 to present.

Professional Memberships: American Physical Society

Name: Junwen Li Date of Degree: May, 2010

Institution: Oklahoma State University Location: Stillwater, Oklahoma

Title of Study: FIRST-PRINCIPLES STUDY OF ELECTRONIC PROPERTIES OF ONE DIMENSIONAL NANOSTRUCTURES

Pages in Study: 130 Candidate for the Degree of Doctor of Philosophy

Major Field: Physics

Scope and Method of Study:

In this work, we present simulation results for the electronic properties of two types of quasi-one-dimensional nanostructures: graphene nanoribbons and silicon nanowires. The electronic structures throughout the dissertation were calculated within a first-principles, all-electron, self-consistent local density functional (LDF) approach tailored for helical symmetry. Tight-binding models (TBM) were employed to study the energy gaps and bonding characteristics of armchair graphene nanoribbons. Within the study of silicon nanowires, we were interested in surface passivation effects and electronic transport properties of silicon nanowires with surface defects. The transport calculation makes use of the Landauer approach implemented with non-equilibrium Green's function formalism.

Findings and Conclusions:

For the study of graphene nanoribbons, we found that the zigzag ribbons exhibited spin-polarized ground states with ferromagnetic edges on opposite sides aligned antiferromagnetically. The electron states near the Fermi level in zigzag ribbons are localized on the edge carbon atoms. The armchair ribbons have ground states of degenerate spin configuration and the LDF energy gaps separate into three families, which is not consistent with the nearest-neighbor TBM. The third-nearest-neighbor interaction was introduced to resolve the discrepancy between LDF and TBM in armchair ribbons. We found that armchair graphene ribbons have two different responses to twist deformation according to ribbon widths, suggesting potential nanomechanical application. In the investigation of silicon nanowires, we found that passivation using hydroxyl or methyl groups reduced the band gaps compared to hydrogen-terminated Si nanowires, and passivation using methyl groups produced systems with indirect gaps for all $\langle 100 \rangle$ Si nanowires studied. All band gaps were direct in the $\langle 110 \rangle$ Si nanowires independent of passivation. The distributions of near-gap orbitals were greatly affected by the surface substituents. We also found that the carrier effective masses of $\langle 100 \rangle$ Si nanowires were sensitive to the diameter and passivation, while those of $\langle 110 \rangle$ Si nanowires were not. We show that the hydroxyl defects can greatly reduce the conductance of hydrogen-passivated Si nanowires and can be used to tune the conductance of the silicon nanowires.

ADVISOR'S APPROVAL: Dr. John W. Mintmire